Modeling wind waves from deep to shallow waters in Lake Michigan using unstructured SWAN

Miaohua Mao[1], André. J. van der Westhuysen[2], Meng Xia[1, *], David J. Schwab[3], Arun Chawla[4]

[1]Department of Natural Sciences,
University of Maryland Eastern Shore,
MD, USA

[2]IMSG at NOAA/NWS/NCEP/Environmental Modeling Center,
College Park, MD, USA

[3]University of Michigan Water Center,
Graham Environmental Sustainability Institute,
University of Michigan, Ann Arbor, MI, USA

[4]NOAA/NWS/NCEP/Environmental Modeling Center,
College Park, MD, USA

*email: mxia@umes.edu

Submitted to the Journal of Geophysical Research: Oceans (In revision)

Abstract

Accurate wind-wave simulations are vital for evaluating the impact of waves on coastal dynamics, especially when wave observations are sparse. It has been demonstrated that structured-grid models have the ability to capture the wave dynamics of large-scale offshore domains, and the recent emergence of unstructured meshes provides an opportunity to better simulate shallow-water waves by resolving the complex geometry along islands and coastlines. For this study, wind waves in Lake Michigan were simulated using the unstructured-grid version of Simulating WAves Nearshore (un-SWAN) model with various types of wind forcing, and the model was calibrated using *in-situ* wave observations. Sensitivity experiments were conducted to investigate the key factors that impact wave growth and dissipation processes. In particular, we considered (1) three wind field sources, (2) three formulations for wind input and whitecapping, (3) alternative formulations and coefficients for depth-induced breaking, and (4) various mesh types. We find that un-SWAN driven by Global Environmental Multiscale (GEM) wind data reproduces significant wave heights reasonably well using previously proposed formulations for wind input, recalibrated whitecapping parameters, and alternative formulations for depth-induced breaking. The results indicate that using GEM wind field data as input captures large waves in the mid-lake most accurately, while using the Natural Neighbor Method wind field reproduces shallow-water waves more accurately. Wind input affects the simulated wave evolution across the whole lake, whereas whitecapping primarily affects wave dynamics in deep water. In shallow water, the process of depth-induced breaking is dominant and highly dependent upon breaker indices and mesh types.

Keywords: Unstructured-grid SWAN; Lake Michigan; Wind input; Whitecapping; Depth-induced breaking

KEY POINTS:

- Impacts of three different wind field sources on lake wave dynamics are examined
- Modifications to wind input and whitecapping formulations are critical to deep-water wave dynamics
- Depth-induced wave breaking and the choice of mesh type dominate modeled shallow-water wave dynamics

1. **Introduction**

Lake Michigan (Fig. 1a), the third largest lake in the Great Lakes system by surface area (58,000 km^2) and second largest by volume (4,900 km^3), has experienced severe windstorms over the past 20 years (Jensen et al., 2012). These extreme events present coastal hazards such as high waves and rip currents at recreational beaches, especially along the lake's southeastern coast. Furthermore, a number of lake processes driven by extreme winds and waves, such as sediment resuspension and plume dynamics, can also be significantly affected by these storms, which can impact the regional ecosystem, as occurred with the 1998 and 1999 spring blooms. Although wave observations are routinely recorded by the National Oceanic and Atmospheric Administration's National Data Buoy Center (NOAA-NDBC), gaps in data for the mid-lake (deep-water) and some coastal (shallow-water) stations still exist under severe storm conditions. Therefore, accurate wind-wave simulation is fundamental to the understanding of complex coastal dynamics in Lake Michigan (Lou et al., 2000; Schwab et al., 2000; Chen et al., 2004; Jensen et al., 2012).

Given the limitations, especially in shallow water, in available wave buoy data, a third-generation wind-wave model known as Simulating WAves Nearshore (SWAN, Booij et al., 1999) has been widely used for both hindcasting surface gravity waves (Rogers et al., 2003) and forecasting future conditions (Rogers et al., 2007). Using the spectral action balance equation for wave energy (Gelci and Cazalé, 1953), SWAN simulates the growth, propagation, and decay of waves, taking into account current- and depth-induced refraction and frequency shifts, wind input, whitecapping dissipation, bottom friction, depth-induced wave breaking, and nonlinear wave–wave interactions (Booij et al., 1999). Whitecapping is widely regarded to be the principle mechanism for wave dissipation in deep water, and therefore many semi-empirical formulations for this process have been developed and calibrated (e.g., Rogers et al., 2003, 2012; van der Westhuysen et al., 2007). Rogers et al. (2003) calibrated the free parameters for the wave steepness-related whitecapping formulation of Komen et al. (1984). Specifically, Rogers et al. (2003) increased the weighting of the relative wave number to shift the dissipation toward higher frequencies, and made simultaneous adjustment to the dissipation rate to match the limiting spectrum of Pierson and Moskowitz (1964). This modification greatly reduced the error in the estimation of wave frequency at mid-lake stations (NDBC 45002 and 45007, see Fig. 2a). However, the interpolated spatial wind field used as input for the model was based only on mid-lake stations, which may bias the estimation of complex wind conditions near coasts (Jensen et al., 2012; Alves et al., 2014).

In order to quantify simulation error resulting from inaccuracy in the wind field data, Jensen et al. (2012) hindcasted seven Lake Michigan storms from 1989 to 2009 using the WAve Model (WAM) Cycle 4 with two sources of wind field data. These data were derived from the NOAA National Centers for Environmental Prediction's (NOAA-NCEP) Climate Forecast System Reanalysis (CFSR) wind field, and from the Great Lakes Environmental Research Laboratory's (GLERL) observation-based Natural Neighbor Method (NNM) wind field. Jensen et al. (2012) compared their simulation results with observations from buoys in the mid-lake and one station near the western shore (station 45010, where water depth is 19.6 m, see Fig 2a). They reported that the spatial structures of the wind and wave fields were similar, but the model driven by the spatially coherent CFSR wind data outperformed the model using the NNM wind data for the estimation of storm waves (defined as the mean value of significant wave height (SWH) plus two times the variance) at mid-lake. Alves et al. (2014) confirmed, based on distinct responses to alternative wind fields (e.g., NCEP's North American Mesoscale Model (NAM), and the National Digital Forecast Database) using WAVEWATCH III (WW3, Tolman, 2002), that model accuracy is strongly dependent upon the selection of wind field sources, and that model performance can be further improved by applying more advanced parameterization for deep-water wave physics (i.e., wind input and whitecapping terms). However, they used a 2.5-km-resolution curvilinear structured grid over the entire Great Lakes system without specific focus on shallow-water regions where the complex and steep bathymetry would likely be better resolved with flexible unstructured meshes (Zijlema, 2010). Although a 200-m-resolution structured-grid shallow-water model (STeady-state spectral WAVE, known as STWAVE, see Massey et al., 2011) for the southwestern shore of Lake Michigan and Green Bay was applied by Jensen et al. (2012), its assumption of stationarity may limit its accuracy. Moreover, the one-way nesting process from unstructured mesh to structured grid (Jensen et al., 2012) may introduce both physical and numerical errors (Zijlema, 2010). Because of the difficulty of adjusting mesh size and orientation to accommodate highly irregular coasts and island shorelines, models that use unstructured meshes typically outperform those that use structured grids in computational accuracy and efficiency (Zijlema, 2010).

For their Gulf of Mexico study domain, Kerr et al. (2013) concluded that wave statistics were insensitive to grid resolution (i.e., a moderate-resolution mesh vs. a high-resolution mesh) in deep-water (water depths greater than 3000 m) and shelf regions (water depths between 50 and 200 m), but were sensitive to grid resolution at coastal stations. Aside from the effect of grid resolution, shallow-water wave dynamics assessment is also significantly affected by the description of depth-induced breaking. Van der Westhuysen (2010) applied various models of wave breaking (Battjes and Janssen, 1978, hereafter BJ78; Thornton and Guza, 1983, hereafter TG83) to three shallow lakes in the Netherlands with typical water depths of less than 5 m, and improved the models' accuracy by optimizing the breaker index. Even though Lake Michigan is a relatively deep lake, with an average water depth of about 85 m, appropriate parameterization of depth-induced breaking is nonetheless expected to improve the accuracy of wave simulations for its shallow-water regions (Van der Westhuysen, 2010; Salmon et al., 2015). In addition, the variation in monthly lake levels in the Great Lakes system reported by Sellinger et al. (2007) and Gronewold and Stow (2014) may be an important factor for depth-induced breaking. This possibility has not previously been explored. Finally, Rogers et al. (2007) demonstrated that shallow-water wave processes such as depth-induced refraction can introduce error if complex bathymetry is poorly resolved. Dietrich et al. (2013) further developed a range of Courant–Friedriches–Lewy (CFL) limiters for the directional turning rate of the spectral propagation velocities of waves, and succeeded in stabilizing wave simulation for Hurricane Hugo (1989) off the coast of South Carolina. To avoid excessive restriction to wave propagation, Dietrich et al. (2013)

suggested using a CFL value that is as large as possible, but within the range of 0.25–0.5. Therefore, a CFL value of 0.5 is adopted for the simulation herein.

For this study, we configured an unstructured-grid version of SWAN (un-SWAN, Zijlema, 2010) for Lake Michigan over the ice-free period (April–November) for the years 2002–2012, and verified the model's skill with a hindcast of Superstorm Sandy (2012). This study addresses three main questions: (1) How well can un-SWAN simulate surface gravity waves, particularly for extreme wind events? (2) How do the SWH and energy dissipation fields (i.e., whitecapping and depth-induced breaking) respond to wind input during Superstorm Sandy (2012)? (3) How does model performance differ when alternative sources of wind field data, different descriptions of deep- and shallow-water wave physics, and various mesh types are applied?

This study is organized as follows: The methodology is introduced in Section 2, which includes description of the study domain, mesh types, models, datasets, skill metrics, and wind and wave climates of Lake Michigan. Section 3 presents wave simulation results for the default and recalibrated models. Model sensitivity experiments addressing the aforementioned question (3) are reported, and differences are explained in Section 4. Discussion and conclusions are given in Sections 5 and 6, respectively.

2. Methodology

2.1. Study domain and mesh types

From north to south, the major body of Lake Michigan comprises the Chippewa Basin, the Mid-Lake Plateau, and the South Chippewa Basin (Fig. 1b). Its two largest bays (Green Bay and Grand Traverse Bay) and two major islands (Beaver Island and North Manitou Island) are located in the northern part of the lake. Ambient flows into the lake (e.g., from the Grand River, MI, and the channel that connects Lakes Michigan and Huron) are not considered for this study; it is assumed that their effects on the lake's wave dynamics are insignificant. Various computational mesh types, including orthogonal curvilinear (OC) structured grids, and medium- and high-resolution (MR and HR) unstructured meshes are applied (Figs. 2b–d). The OC grid cells are evenly distributed (1.8 × 1.8 km resolution) over the entire computational domain with a total number of 52,975 cells (163 × 325). The spatial structure of the OC grid is similar to that applied by Alves et al. (2014), but is somewhat higher in horizontal resolution. The MR unstructured mesh consists of 5,256 nodes and 9,581 elements. The HR version has a similar mesh structure, but contains 20,108 nodes and 38,324 elements. The mesh size of the MR version benefits from a capacity for local mesh refinement; it decreases to 340 m in the shallow-water region (water depth below 50 m), whereas it increases to 440–7600 m over the major body of the lake (water depth over 50 m). The lake bathymetry is resolved more finely by the HR version, of which the mesh size is about half of that for the MR version. Details about the domain size and mesh distribution over the lake are given in Table 1.

2.2. Model description

The un-SWAN model is based on the spectral action balance equation for wave energy (Gelci and Cazalé, 1953; Booij et al., 1999; Zijlema, 2010; SWAN Group, 2012a, 2012b):

$$\frac{\partial N}{\partial t} + \frac{\partial C_{g,x} N}{\partial x} + \frac{\partial C_{g,y} N}{\partial y} + \frac{\partial C_{g,\sigma} N}{\partial \sigma} + \frac{\partial C_{g,\theta} N}{\partial \theta} = \frac{S_{tot}}{\sigma} \tag{1}$$

where σ is the intrinsic frequency, θ is the wave direction taken counterclockwise from the geographical east, *N* denotes the wave action spectral density, t is time, and C_g is the wave group velocity in space $(x, y, \sigma, and\ \theta)$. From the right side of Eq. (1), S_{tot} is expressed as follows:

$$S_{tot} = S_{in} + S_{nl3} + S_{nl4} + S_{ds,w} + S_{ds,b} + S_{ds,br}. \tag{2}$$

These six terms for wave energy sources and sinks represent wave growth by wind input, nonlinear wave energy transfer through three-wave and four-wave interactions, wave decay due to whitecapping and bottom friction, and depth-induced wave breaking, respectively.

The wind input term in the wave model consists of two parts:

$$S_{in}(\sigma, \theta) = A + BE\ (\sigma, \theta) \tag{3}$$

where term A represents the initial linear growth stage of wind waves. The following exponential growth term $BE\ (\sigma, \theta)$ is one or more orders of magnitude larger than the linear term because of the positive feedback of wave energy. The default formulation for the exponential wind-wave growth process is based on the work of Snyder et al. (1981), and given by Komen et al. (1984) as follows:

$$B = \max\left[0, 0.25 \frac{\rho_a}{\rho_w}\left(28 \frac{u_*}{c_{ph}} cos(\theta - \theta_w) - 1\right)\right] \sigma. \tag{4}$$

An alternative formulation by Janssen (1991) adopts the quasi-linear wind-wave theory:

$$B = \beta \frac{\rho_a}{\rho_w} (\frac{U_*}{c_{ph}})^2 max[0, \cos(\theta - \theta_w)]^2\ \sigma. \tag{5}$$

Yan (1987) proposed an empirical fit equation based on experimental datasets:

$$B = D\left(\frac{U_*}{c_{ph}}\right)^2 cos(\theta - \theta_w) + E\left(\frac{U_*}{c_{ph}}\right) cos(\theta - \theta_w) + Fcos(\theta - \theta_w) + H \tag{6}$$

in which ρ_a and ρ_w refer to the density of air and water respectively; $U_*\ and\ c_{ph}$ are the wind friction velocity and wave phase speed respectively, θ and θ_w are the mean wave and mean wind direction respectively, and β is the Miles constant. The coefficients defined by Yan (1987) were refitted by van der Westhuysen et al. (2007) such that

$D = 4.0 \times 10^{-2}, E = 5.52 \times 10^{-3}, F = 5.2 \times 10^{-5}, and\ H = -3.02 \times 10^{-4}$. The key variable U_* is calculated from the wind speed at 10 m elevation (U_{10}), and the wind drag coefficient C_d by the following formulation by Wu (1982):

$$U_*^2 = C_d \times U_{10}^2 \tag{7}$$

$$C_d \times 10^3 = \begin{cases} 1.2875 & U < 7.5\, m/s \\ (0.8 + 0.065 \times U_{10}) & U_{10} \geq 7.5\, m/s \end{cases} .$$

(8)

Powell et al. (2003) suggested that the wind drag coefficient C_d should be capped when U_{10} is greater than about 33 m/s. We adopt the recommendation of the SWAN manual (SWAN Group, 2012a, 2012b) by setting an upper limit of $C_d = 2.5 \times 10^{-3}$ for a maximum of $U_{10} = 26\ \mathrm{m/s}$.

The whitecapping dissipation term in Eq. (2) is based on the pulse-driven model of Hasselmann (1974), as modified by Komen et al. (1984) and Janssen (1992):

$$S_{ds,w}(\sigma,\theta) = \Gamma \sigma_m (\frac{k}{k_m}) E(\sigma,\theta). \tag{9}$$

The steepness parameter Γ is defined as:

$$\Gamma = C_{ds}[(1-\delta) + \delta(\frac{k}{k_m})](\frac{s}{s_{PM}})^m \tag{10}$$

where σ_m and k_m are the mean wave frequency and mean wave number respectively, k is the wave number, and C_{ds} and δ are tunable parameters that represent the whitecapping dissipation rate and weighting coefficient of the relative wave number, respectively. The superscript m denotes the power of the ratio of the overall wave steepness s to that of Pierson and Moskowitz (1964)'s spectrum $s_{PM} = \sqrt{3.02 \times 10^{-3}}$.

The default depth-induced breaking formulation is derived from the BJ78 model, which assumes that the maximum possible wave height H_{max} for a given local water depth d is limited by a breaker index γ_{BJ}, expressed as $H_{max} = \gamma_{BJ} \times d$. The alternative TG83 model introduces a weighting function with a scaling coefficient $M_{TG} = (H_{rms}/\gamma_{TG} d)^2$, where $\gamma_{TG} = H_{rms,max}/d$ is the ratio of the maximum possible root-mean-square of wave height to local water depth. The default breaker indices for the BJ78 and TG83 models are $\gamma_{BJ} = 0.73$ and $\gamma_{TG} = 0.42$, respectively.

On the basis of the governing Eq. (1), the un-SWAN model is discretized with a first-order, backward-space, backward-time scheme, and a hybrid central or upwind scheme in wave spectral space. This implicit geographical propagation scheme avoids the strict CFL limitation on time step, but a CFL limiter of 0.5 in the directional space of waves is nonetheless used to prevent excessive depth-induced refraction in regions with under-resolved bathymetry. The equation is integrated using a finite difference method. In this study, the wave directions are evenly distributed into 36 bins with a constant bandwidth of 10°, and frequencies are discretized over 32 bins with an increasing logarithmic scale over the range of 0.0512–1 Hz. The computational time interval is set to 5 min. For detailed descriptions of discretization skill and the numerical scheme, readers are referred to Booij et al. (1999) and Zijlema (2010).

2.3. Model input and observational data

The wave model was applied using three different sources of wind field data adjusted to 10 m elevation: (a) the GLERL's NNM-based (Schwab and Morton, 1984) hourly, 2-km horizontal resolution forcing, derived from lake buoy- (at mid-lake and several nearshore stations) and coastal land site-based data (Lang and Leshkevich, 2014); (b) the Canadian Meteorological Centre's three-hourly, 10-km resolution wind field from the Global Environmental Multiscale (GEM) Model, which assimilates both *in situ* and remotely sensed data (Côté et al., 1998); and (c) the reanalysis dataset from the NOAA-NCEP Climate Forecast System Version 2 (CFSv2) with hourly, 0.205° (longitudinal) and ~ 0.204° (latitudinal) resolution, which assimilates surface, upper balloon, aircraft, and satellite observations (Saha et al., 2014). Gridded bathymetry data obtained from the NOAA National Geophysical Data Center (NGDC), with a resolution of 6 arc-sec (approximately 185 m in longitude and 133 m in latitude), are interpolated to computational cells. The lake bathymetry is steep near the shallow coast, islands, and bays (e.g., Green Bay), and mild in the Chippewa Basin and the South Chippewa Basin (Figs. 1b and 2a). Monthly lake level anomaly values are derived from the NOAA's Great Lakes Water Level Dashboard (GLWLD) surface water elevation records. The NOAA-NDBC provides access to observational wind and wave buoy data from all over the lake that are managed by various national and regional organizations (Fig. 2a and Table 2).

2.4. Skill metrics

Taylor diagrams (Taylor, 2001) were used to evaluate model skill based on the correlation coefficient (CC), normalized standard deviation (NSTD), and root-mean-square deviation (RMSD). In addition, the scatter index (SI) and relative bias (RB) were also included in the scatterplots for model-to-data comparisons. These expressions are given as follows:

$$CC = \frac{\frac{1}{N}\sum_{n=1}^{N}(f_n-\bar{f})(r_n-\bar{r})}{\sigma_f \sigma_r} \tag{11}$$

$$NSTD = \frac{\sqrt{\frac{1}{N}\sum_{n=1}^{N}(f_n-\bar{f})^2}}{\sqrt{\frac{1}{N}\sum_{n=1}^{N}(r_n-\bar{r})^2}} \tag{12}$$

$$RMSD = \left[\frac{1}{N}\sum_{n=1}^{N}(f_n - r_n)^2\right]^{1/2} \tag{13}$$

$$SI = \frac{\sqrt{\frac{1}{N}\sum_{n=1}^{N}(r_n - f_n)^2}}{\frac{1}{N}\sum_{n=1}^{N} f_n} \tag{14}$$

$$RB = \frac{\sum_{n=1}^{N}(r_n - f_n)}{\sum_{n=1}^{N} f_n} \tag{15}$$

where $\bar{f}$ and $\bar{r}$ are the mean values of the datasets f_n and r_n respectively, in a sample of size N, and σ_f and σ_r are the corresponding standard deviations. In this study, f_n denotes the observed wind speed, SWH, or peak wave period (PWP) at time n, and r_n is the corresponding value from model input or output.

2.5. Wind and wave climates of Lake Michigan

The hourly data for wind speed and SWH at mid-lake stations were averaged to monthly values for the ice-free period of the years 2002–2012. The spatial variability of wind and wave climates was further investigated with the addition of recently-deployed coastal buoy stations in 2011 and 2012.

Figure 3a presents the rose diagrams for hourly wind speeds and SWHs at buoys located in the northern mid-lake area (45002), southern mid-lake area (45007), and near the mid-eastern (45029) and southeastern shores (45026). Figure 3b shows additional wind roses for hourly wind speed along the southwestern (FSTI2), mid-western (45013), northwestern (0Y2W3), and northeastern shores (45024), and in Little Traverse Bay (45022) and Green Bay (45014). These data indicate that wind directions at mid-lake stations follow primarily along the lake's longitudinal axis. However, at the shallow eastern coastal stations 45026 and 45029, multidirectional coastal winds show clear dominance of an onshore component from the lake's interior. Steered by these westerly and northwesterly local winds, the shallow-water waves propagate toward the eastern coast of the lake. In contrast, winds at northeastern/northwestern and mid-western coastal stations show signatures of alongshore and offshore directions respectively (Fig. 3b). Near the extremely shallow southwestern coast, wind conditions are complex, and no single prevailing wind direction is observed. It should be noted that the winds over Little Traverse Bay and Green Bay are predominately parallel to the major axes of the respective bays. The intensity of wind over the lake is most often mild (5–10 m/s), followed in frequency by weak (0–5 m/s), high (10–15 m/s), and strong values (15–20 m/s). Across all stations, small ($0 < \text{SWH} \leq 2$ m) and medium (2 m $< \text{SWH} \leq 4$ m) waves account for a large proportion of the observed SWH, although large (4 m $< \text{SWH} \leq 6$ m) and moderately high waves ($\text{SWH} > 6$ m) are present at mid-lake stations. These fully-developed extreme wave conditions are likely induced by the strong winds with long fetch distances (400–500 km) that follow along the lake's longitudinal axis.

Figure 4 shows histograms of monthly-averaged SWH and wind speed at various deep- (northern and southern mid-lake), intermediate- (Little Traverse Bay) and shallow-water stations (Green Bay, and the western and eastern coasts). An interesting phenomenon is that the monthly-averaged SWHs in the lake are larger in the late fall (i.e., October and November), while the monthly-averaged wind speeds during these two months have similar speeds to those of the late spring (i.e., April and May). Because SWH is highly sensitive to the intensity of wind speed (i.e., it is proportional to the square of wind speed, see Benetazzo et al., 2013), the monthly-averaged SWH value may be enhanced significantly by several extreme wind events. However, these event-dominated gusts generally last only a few hours, which may limit their contribution to the monthly-averaged wind speed. Therefore, this phenomenon may be explained by the observation that extreme wave conditions occurred more frequently in the late fall than in the spring in the mid-lake area in the years 2002–2012 (i.e., a total of eleven events in the late fall and six in the spring, see Tables 3–4 and 3–5 in Jensen et al., 2012). Spatially, the monthly-averaged SWHs of the deep-water regions are higher than those in the intermediate- and shallow-water regions. This difference emerges because the elongated wind fetch over the spacious mid-lake region can generate fully-developed deep-water waves, while the coastal winds are significantly impeded by the irregular coastline, and the waves are affected by strong depth-induced breaking in the shallow-water regions. It is noted that the monthly-averaged SWHs near the eastern coast are larger than those near the western coast, presumably because of the long-term averaged westerly wind conditions over Lake Michigan that enhance the fetch toward the eastern coast (Beletsky and Schwab, 2008).

3. Wave simulations

3.1. Long-term wave simulation with the default model

We first consider a long-term Lake Michigan wave simulation from April to November in the years 2002–2012 using the MR un-SWAN model with the default physics settings of version 40.91 (SWAN Group, 2012a, 2012b). The default model is driven by the GLERL's observation-based NNM winds, as applied operationally by NOAA in the Great Lakes Operational Forecast System (GLOFS). The wind input and whitecapping terms are based on the work of Snyder et al. (1981) and Komen et al. (1984), with the default dissipation rate of $C_{ds} = 2.36 \times 10^{-5}$ and the relative wave number weighting coefficient of $\delta = 0$. The formulation of Hasselmann et al. (1973), with a constant coefficient of 0.067 m^2s^{-3}, is applied for bottom friction dissipation. Depth-induced breaking is incorporated through the BJ78 model, with a default breaker index of $\gamma_{BJ} = 0.73$. In addition, the directional wave speed is limited, with a CFL number of 0.5 to restrain spurious refractions over regions where the bathymetry is under-resolved (Dietrich et al., 2013). Details of the physical parameterization of the default model (Case 1a) can be found in Table 3.

Model to data comparisons for wind speed and SWH are shown in Figs. 5a and b, respectively. On average, slight underestimations (negative RB) of the wind speeds in NNM data are noted across all stations except for a very shallow northwestern shore station (0Y2W3). With this wind forcing, SWHs produced with the un-SWAN model are underestimated for most stations, although they are overestimated in Green Bay (45014), and along the mid-western (45013) and southwestern shores (45018, 45016, and 45015). Because wind forcing is the primary driving agent of the wave dynamics of an enclosed lake, underestimation of wave height can be partially attributed to the underprediction of wind speed. However, the degrees of underprediction for wave heights at stations 45002 and 45007 (-4.4% and -6.2%) are significantly larger than for wind speed (-0.3% and -1.4%), which suggests that the deviation may originate from deficiencies in the treatment of deep-water wave physics (i.e., the parameterization of whitecapping dissipation, see Rogers et al., 2003).

Overall, the scores for the RB, SI, and CC for wind speeds and SWHs for the mid-lake area are superior to those for the extreme shallow-water stations in Green Bay and along the northwestern and southwestern coasts, where the interactions of waves with bathymetry are highly dynamic. Consequently, the largest NSTD of SWH is found at the shallowest southwestern shore station (NSTD = 1.68). The large SI and RMSD scores for SWH from the station in Green Bay (SI = 1.026 and RMSD = 0.39 m) are largely attributable to significant underestimation of outliers in wave height (3 m < SWH < 5 m) at that location. The third trend apparent in the model results is that the SWHs along the western shores (45013, 45015, 45016, and 45018) and in Green Bay are overestimated (i.e., positive RB) despite slight underestimation of wind speed (i.e., negative RB). This negative correlation is likely because of inaccurate estimation of shallow-water wave processes in the default model, such as the omission of monthly lake level variations, and deficiencies in the description of depth-induced refraction and breaking.

To improve these results, additional experiments using un-SWAN with alternative wind field sources and different formulations and parameterizations for deep- and shallow-water wave physics are discussed below.

3.2. Improved performance with the recalibrated model

In this section, we examine the skill of a recalibrated MR un-SWAN model for which the input sources and wave physics have been optimized, as will be discussed in the following sections (see model input and settings of Case 2c in Table 3). Figures 6a and b show scatterplots of simulated SWHs and PWPs from Cases 1a (the default version) and 2c (the recalibrated MR un-SWAN model) versus observations over April–November 2012 at 13 NDBC stations. Large waves are identified at the eastern shore buoys (45029 and 45026) and northern mid-lake buoy (45002), and moderately high waves are identified at the southern mid-lake buoy (45007) caused by enhanced wind intensity and fetch distance under storm conditions (e.g., the dominant northerly winds of Superstorm Sandy, 2012). Overall, both model configurations demonstrate reasonable skill in reproducing wave heights across all stations except for some large outliers in Green Bay (45014) and along the northwestern shore (0Y2W3 and C58W3). The recalibrated un-SWAN model slightly overestimates SWHs at buoys in the mid-lake area (45002 and 45007), and along the southwestern (45018 and 45016), mid-western (45013) and north-of-mid-eastern shores (45161), whereas it underestimates SWHs in Little Traverse Bay (45022), Green Bay (45014), and near the southeastern (45026), south-of-mid-eastern (45029), northeastern (45024), and northwestern shores (0Y2W3 and C58W3). Compared with the default model, the recalibrated model improves not only the simulation of extreme wave height at buoys in mid-lake, but also the overall statistical accuracy (RB and SI) for SWH along the shallow eastern (45026, 45029, 45024) and southwestern shores, and in Little Traverse Bay. Additionally, the RB and SI scores for PWP are significantly reduced in the recalibrated model at all NDBC buoy stations except for Green Bay (Fig. 6b). It should be noted that a large portion of low-frequency (i.e., higher PWP) waves are underpredicted at buoy stations 45024 and 45022. This possibly because the wind sea estimated in the model causes unphysical swell dissipation that was not observed in the buoy data (Rogers et al., 2003), which is beyond the scope of this study.

Taylor diagrams (Fig. 7) confirm quantitatively that both models perform well statistically (RMSD, NSTD, and CC) for wave simulations across all stations, except for SWH in Green Bay (45014) and near the northwestern coast, and for PWP near the southwestern coast. The recalibrated version yields superior scores for the NSTD of both SWH and PWP for most buoy stations compared to scores from the default model. In the next section, the verification of the recalibrated un-SWAN model is examined by hindcasting the dynamic responses of the spatiotemporal wave field to Superstorm Sandy (2012).

3.3. Hindcasting case: Superstorm Sandy (2012)

The wind speeds and directions from the GEM and NNM fields, along with their resulting SWHs and PWPs from the un-SWAN model, are compared with observed results of the Superstorm Sandy event from October 29 to November 1, 2012 (Fig. 8). Both GEM and NNM winds agree well with observational wind data across all stations, but the NNM wind field shows superior performance at the shallow-water station 45013. Consequently, the un-SWAN model using the NNM winds expresses superior skill in reproducing SWH at the shallow-water station, whereas the model driven by the GEM model winds reproduces mid-lake extreme waves more accurately. In particular, the northerly wind-induced extreme SWH at the southern mid-lake buoy 45007 is captured nearly perfectly by the model that uses the GEM winds, possibly because it better estimates the wind field along the lake's longitudinal axis between the mid-lake buoys. It should be noted, however, that the SWH at the shallow-water station 45013 is consistently overestimated. Additional numerical experiments (not described here) indicate that the SWH variations that result from using different formulations for depth-induced breaking (BJ78; Nelson, 1987; Ruessink et al., 2003) and bottom friction dissipation (Collins, 1972; Madsen et al., 1988), and from coupling with the ADvanced CIRCulation Model (ADCIRC, see Dietrich et al., 2011) are not as significant as those that result from using alternative wind fields (e.g., the GEM and NNM winds). Van der Westhuysen (2010) demonstrated that wind direction plays a key role in determining shallow-water wave growth (e.g., sloping bed surf zone or finite water depth conditions), and therefore further impacts the intensity of depth-induced breaking. Alves et al. (2014) reported that a wave model with improved physical parameterization designed to address short-fetch (offshore winds) wave growth could potentially provide more accurate storm wave simulation for the Great Lakes. Another possible explanation for remaining overprediction of SWH is insufficient treatment of the air-flow separation effect, which could reduce wave growth intensity via wind input (Donelan et al., 2006). Relative to the consistent SWH overestimation at the western shore station 45013, the intermittent underestimations at the northwestern shore stations 0Y2W3 and C58W3 were probably caused by the lack of consideration for wind gustiness (Cavaleri, 2009), which could significantly enhance wind intensity on a short time scale (Powell et al., 2003). The gusts, which typically reach peak speed for only 5 or 8 seconds, are rarely recorded by NDBC buoys because of power outages and anemometer failures that occur under extreme winds (Powell et al., 2003). Therefore, further improvement could be made through maintaining more continuous wind gustiness records and incorporating them into the wind-wave model. Compared to the sensitivity of SWH predictions, the PWP predictions at mid-lake buoys and near the shallow-water station 45013 are reproduced satisfactorily by both models regardless of the type of wind field used.

Figure 9 maps the spatial distribution of water depth, maximum total energy dissipation, whitecapping, and depth-induced wave breaking based on the un-SWAN model driven by the GEM wind data during the northerly winds that dominated Superstorm Sandy (2012). The total wave energy dissipation is appreciable near the southeastern coast and eastern portion of the South Chippewa Basin, but insignificant in the Chippewa Basin and near other coasts. Figures 9c and d illustrate that the energy dissipation in deep-water regions is dominated by whitecapping with dissipation reaching approximately 10–15 W/m^2. The spatial similarity between the regions for maximum whitecapping dissipation and SWH (not shown here) indicates that the wind-induced extreme waves in the mid-lake region are primarily dissipated through steepness-related whitecapping. However, the intensity of deep-water whitecapping dissipation declines gradually as waves propagate toward shallower zones (20 m $<$ water depth $\leq$ 40 m), and energy dissipation is eventually dominated by depth-induced breaking in nearshore regions (10 m $<$ water depth $\leq$ 20 m). Even though shallow-water wave breaking only occurs over a narrow strip along the southeastern shore of the lake, the maximum dissipation intensity therein reaches as high as 36.5 W/m^2.

4. Model sensitivity

To individually address the above factors that have improved model accuracy, sensitivity analyses over the ice-free period of the year 2011 were conducted. In particular, we included alternative sources for wind fields (GEM, CFSv2, and NNM), various combinations of wind input and whitecapping formulations (e.g., Komen et al., 1984; recalibrated Rogers et al., 2003; van der Westhuysen et al., 2007), different settings for depth-induced breaking (e.g., the BJ78 and TG83 models), and additional mesh types (the OC structured grid, and the MR and HR unstructured meshes). The SWH and PWP estimated from each model are compared with *in-situ* wave observations from buoys in the mid-lake area (45002 and 45007), Little Traverse Bay (45022), and along the southwestern (45018) and southeastern shores (45026).

4.1. Sensitivity to alternative sources of wind fields

Three sources of wind field data, namely the fields of the atmospheric models GEM and CFSv2, and observation-based NNM fields, were used to drive the MR un-SWAN wave model. The default deep-water wave growth formulation of Snyder et al. (1981) and

Komen et al. (1984) (WAM Cycle 3, henceforth denoted WAM3) was applied to these three simulations. The comparisons of various wind fields with NDBC buoy data are shown in Fig. 10a. Note that buoy winds at station 45018 are missing and were replaced with winds from the adjacent station FSTI2. Figure 10b shows the scatterplots for SWH produced with un-SWAN model using the three different wind fields. The wind speeds determined from either atmospheric model scatter around the line of perfect agreement, whereas the observation-based NNM winds yield superior statistical scores for the RB, SI, CC, and RMSD for all buoy stations. At the northern and southern mid-lake buoys, the RB scores for the CFSv2 winds are 11.2% and 9.1%, which are reduced to less than 3.2% and 1% with the GEM and NNM winds, respectively. As a direct result of the overestimation of wind speeds, SWHs are slightly overestimated, e.g., by 3.8% at station 45002 and 8.9% at station 45007 using the GEM data, and this effect is enhanced to over 20.7% when the relatively stronger CFSv2 winds are used. Relative to the SWH overpredictions driven by atmospheric model winds, SWH is consistently underestimated when the observation-based NNM winds are used, e.g., by -16.1% at station 45002 and -12% at station 45007; this bias is especially notable for extreme values. Overall, SWHs at mid-lake buoys determined from the GEM fields outperform the NNM-based predictions by providing more favorable values for the SI, NSTD, and RMSD. For the intermediate-water stations 45022 and 45026, none of the three wind fields consistently produce strong scores for the SI, NSTD, and RMSD. At the shallow-water station 45018 (with a water depth less than 5 m), all three simulations show a consistently overestimated SWH with large RB scores, especially for wave heights in the range of 0.5–1 m.

To further investigate the SWH variation created by different wind models, Fig. 11 presents the spatial distributions of maximum wind speeds and corresponding wave fields using the GEM, CFSv2, and NNM wind fields. During a northerly clipper storm (September 29–30, 2011), both the GEM and CFSv2 winds show a smoothly increasing trend of wind intensity southward along the lake's longitudinal axis (20–24 m/s), whereas the NNM wind field is characterized by several small lobes of local wind speed maxima (24–32 m/s) distributed around the lake's perimeter. These spatial differences are caused by the assimilation of wind data in the atmospheric models from multiple observational sites across the entire lake (Côté et al., 1998; Saha et al., 2014), whereas the observational data-based wind field is heavily dependent upon the limited buoys at mid-lake and near the coast, as well as the meteorological stations at coastal land sites (Lang and Leshkevich, 2014).

Similar to the spatial patterns of atmospherically modeled wind fields, the wind-induced waves increase in intensity along the lake's major axis, but to a greater degree, presumably because of the nonlinear dependence of SWH on wind speed and the enhanced wind fetch distance in the downwind direction (Fig. 11). In addition, the weaker GEM winds (relative to the CFSv2 winds) and the spatial incoherence of the NNM wind field are reflected in the associated wave field. In particular, wave heights driven by the atmospheric models exceed 6 m in the South Chippewa Basin, while they are less than 5 m near the adjacent southeastern coast when derived from the observational data-based winds. Because the interpolation distance of the NNM wind field is 30 km (Beletsky and Schwab, 2001), significant underestimations of wave height at the southern mid-lake buoy 45007 (see also Fig. 10b) tend to originate from both reduced wind intensity and shorter fetch distance along the lake's longitudinal axis. Another possible explanation is that the frequent variations in wind direction recorded at land–lake boundary sites may be transmitted into the lake's interior through the smoothing interpolation process of the NNM, which would further impede wave growth in that model. In contrast, the spatially coherent GEM and CFSv2 wind fields would facilitate the full development of larger wind waves.

Previous studies indicated that improvements to wave simulations could be achieved through the use of higher quality wind fields. For example, Jensen et al. (2012) reported that deep-water waves were more accurately captured by the WW3 model using the spatially coherent CFSR wind data, whereas the shallow-water waves were better reproduced by adopting the locally-optimized NNM winds from GLERL. Alves et al. (2014) confirmed that using the spatially coherent NAM wind field with the WW3 model outperformed using the NNM wind field with the same model for simulating deep-water waves under storm conditions. Accordingly, a more accurate wind field can be constructed with appropriate blending of atmospherically modeled and observational wind data (He et al., 2004), or with increased spatial coverage by lake buoys that collect data for the construction of observational data-based NNM wind fields (Schwab and Morton, 1984). Based on the greater spatial coherence of the GEM wind field and higher predictive skill of the un-SWAN model for reproducing mid-lake extreme waves, these methods are adopted to explore other factors that may further improve the simulation.

4.2. Sensitivity to wave physics formulations

To investigate the contribution of the representation of wave physics to the model inaccuracies described above, this section explores alternative formulations for both deep- and shallow-water source terms.

4.2.1. Comparison of wind input and whitecapping formulations

Sensitivity experiments for deep-water wave physics were conducted using three different combinations of wind input and whitecapping dissipation terms (Cases 1a–1c in Table 3). Case 1a represents the default Komen et al. (1984) expression with a dissipation rate of $C_{ds} = 2.36 \times 10^{-5}$, and weighting of the relative wave number at $\delta = 0$. Case 1b replaces the default wind input formula of Snyder et al. (1981) with that of Janssen (1991), which is implemented with WAM Cycle 4 (WAM4), and adjusts the tuning parameters to $C_{ds} = 3.0 \times 10^{-5}$ and $\delta = 0.3$. This tuning strategy, similar to the original settings of Rogers et al. (2003), has the effect of shifting the wave dissipation toward higher frequencies, and also matches the spectrum defined by Pierson and Moskowitz (1964). Case 1c considers a saturation-based whitecapping dissipation approach (Van der Westhuysen et al., 2007, hereafter referred to as WF07) with a recalibrated threshold level $B_r = 1.75 \times 10^{-3}$ and dissipation rate of $C_{ds} = 5.0 \times 10^{-5}$.

Figures 12a–c show the scatterplots for SWH, PWP, and SWH above the 99.5th percentile produced with the un-SWAN model versus observational data from various NDBC buoys using the above described deep-water wave physics settings. Overall, the NSTD score for SWH in Case 1b slightly outperforms Case 1a except for at the extreme shallow station 45018. The scores for the RB, SI, CC, NSTD, and RMSD for PWP at mid-lake buoys are significantly improved from Case 1a to Case 1b. This observation confirms the finding of Rogers et al. (2003) that increasing the weighting on the relative wave number improves the representation of whitecapping dissipation and PWP in wave frequency spectra. Under extreme conditions (i.e., SWH above the 99.5th percentile), Case 1b is found to have stronger values for the RB, SI, CC, and RMSD at both mid-lake stations. In particular, the RBs increased from -0.25 to -0.176 at buoy 45002 and from -0.109 to 0.042 at buoy 45007. An explanation for this improvement is that the wind input formulation of Janssen (1991) produces faster wave growth (i.e., quadratic dependence on u_*/c) than that of Snyder et al. (1981) (i.e., linear dependence on u_*/c) under strong wind forcing (i.e., $u_*/c > 0.1$), see details in Eqs. (4) and (5). However, this change becomes insignificant at shallower water-depth stations where wave processes such as depth-induced breaking become a key factor affecting wave dynamics.

Overall, the un-SWAN model with the WF07 expression yields comparable accuracy for SWH at mid-lake to that in the default model, but it reveals advantages by producing stronger RB, SI, NSTD, and RMSD scores at the extreme shallow-water station 45018. Under extreme wave conditions, the adoption of the WF07 formulation improves the accuracy of SWH values for the southern mid-lake buoy. However, the degree of improvement is not as great as that achieved using the recalibrated Rogers et al. (2003) formulation. On average, all cases tend to provide results more consistent with the observational data for SWH and PWP at intermediate- and deep-water buoys than for shallow-water stations. Donelan et al. (2006) postulated that conventional wind input formulations (e.g., Komen et al., 1984; Yan, 1987; Janssen, 1991) used for wave generation ignored the effect of air-sea flow separation, which may result in inaccurate estimation of momentum transfer in a young wave field, e.g., short-fetch wave growth near the shallow coast. Additionally, wind speeds and directions at land–lake interface stations (e.g., FSTI2, 45026, and 45022) are highly complex and unpredictable because of abrupt transitions of the atmospheric boundary layer.

Although models with Cases 1b and 1c settings show comparable levels of predictive skill, the deep-water wave physics represented by Case 1b is adopted for further study because of its superior ability for extreme wave simulation.

4.2.2. Parameterization of the depth-induced breaking term

After the deep-water source terms above have been selected, sensitivity studies turn to shallow-water wave physics, especially for the depth-induced breaking term (Cases 2a–2c in Table 3). Case 2a incorporates monthly lake level anomalies, Case 2b decreases the default breaker index γ_{BJ} to 0.3, and Case 2c uses the alternative TG83 model with a default breaker index of $\gamma_{TG} = 0.42$.

Figure 13 shows the SWH scatterplots for Cases 2a–2c versus observational data taken near the shallow southwestern (45018) and southeastern coasts (45026). As expected, the modifications to the depth-induced breaking term only influence the wave dynamics in shallow water (deep-water stations are not shown here), particularly at the shallowest-water station 45018. At this station, when monthly lake level variability is applied (Case 2a) to the model with constant water depth (Case 1b in Fig. 12a), the RB, SI, NSTD, and RMSD scores are reduced slightly from 0.37 to 0.34, 0.58 to 0.55, 1.46 to 1.42, and 0.19 m to 0.18 m, respectively. However, these values are further reduced greatly (e.g., the RB is decreased by about two thirds, and the SI, NSTD, and RMSD decrease by about half) by reducing the breaker index γ_{BJ} in Case 2b, presumably because of increased breaking intensity at the maximal individual wave height for a given water depth. It is noteworthy that in Case 2c, not only is the RB of Case 2a for station 45018 reduced by about half, but that high skill level is also maintained for station 45026. Therefore, the Case 2c settings are adopted for depth-induced breaking in the proposed model; its sensitivity to various mesh types is examined in the following section.

4.3. Sensitivity to mesh types

Figure 14 shows the scatterplots for SWH with the application of alternative mesh types, specifically the OC structured mesh (top panel), and the MR (middle panel, same as that applied above) and HR unstructured meshes (bottom panel). At mid-lake, all three configurations yield comparable accuracy for SWH, as expected. This consistency also holds true for the intermediate-water stations 45022 and 45026 where water depth is greater than about 20 m, which suggests that both the OC structured grid and the MR unstructured meshes can resolve offshore waves accurately. However, a clear difference can be detected at the shallow-water station 45018 (water depth = 3.9 m) where the model with the MR unstructured mesh outperforms the OC grid by reducing the scores of RB, SI/RMSD, and NSTD by about two thirds, half, and quarter, respectively.

To assess these spatial differences, Fig. 15 presents the spatial distributions of water depth, maximum wind speeds and SWHs from the MR un-SWAN model, OC SWAN minus HR un-SWAN, and MR minus HR un-SWAN. During a clipper storm, the northerly winds (U_{10} = 8–24 m/s) increase along the lake's longitudinal axis and turn northwesterly in an anticlockwise direction, which produces extreme waves with SWHs over 6 m in the South Chippewa Basin. Spatially, the relative differences in SWHs from the application of various mesh resolutions (i.e., MR and HR) are less than 10% in the South Chippewa Basin, 20% in most shallow-water regions, and 30% scattered in the shallow part of Green Bay and near the northern coast. By replacing the HR unstructured mesh with the OC structured grid, however, these variations spread, with relative differences of 20–60% spreading widely across the lake, reaching as high as 80% adjacent to the shallow northern coast and around North Manitou Island (note that different scales are used in Figs. 15c and d). This phenomenon is presumably because of different degrees of resolution for shallow-water wave processes with these different configurations of mesh type. Although strong waves prevail in the South Chippewa Basin, the variability in prediction of SWH among the three mesh types is insignificant because the smooth bathymetry in that region has already been resolved adequately with each mesh type.

The above findings enable us to confirm that the un-SWAN model with the MR unstructured mesh is able to reproduce wave heights as accurately as the HR version, but significantly outperforms the OC version for nearshore waves (water depth < 20 m). In addition, we find that the simulation of the MR un-SWAN is the most efficient version; it requires approximately one half and one fifth the computational time of the OC SWAN and HR un-SWAN, respectively (Table 4).

5. Discussion

In this study, we have demonstrated that wind forcing, deep- (i.e., wind input and whitecapping) and shallow-water wave physics (i.e., depth-induced breaking) play significant and distinct roles in the wave dynamics of deep-, intermediate-, and shallow-water regions. This finding is consistent with the conclusions drawn by Huang et al. (2013) who investigated the dynamic responses of wave energy dissipation to Hurricane Ike (2008) over different regions of the Gulf of Mexico. Huang et al. (2013) made meaningful improvements to wave simulation under hurricane conditions (in which wind speed reaches 43–49 m/s) by adopting different bulk formulae (e.g., Large and Pond, 1981; Wu, 1982; Oey et al., 2006) and/or setting cutoff values (e.g., $C_{dcap} = 2.5$, or wind speed U_{10} = 26.2 m/s) for the wind drag coefficient in the un-SWAN model. However, the maximum U_{10} in Lake Michigan (23.6 m/s in 2011 and 21.0 m/s in 2012) is below the cutoff limit suggested by Huang et al. (2013). Therefore, the improvements made in this study to storm wave simulation for mid-lake buoys were achieved by selecting different sources of wind fields for model input and alternative settings for the formulations of wind input and whitecapping. For example, using the spatially coherent GEM winds led directly to higher accuracy in the reproduction of mid-lake extreme waves, whereas the un-SWAN model driven by the locally-optimized (i.e., point-to-point comparison with NDBC buoy stations), observation-based NNM winds resulted in superior reproduction of shallow-water waves. Moreover, van der Westhuysen et al. (2007) noted that the wind input term becomes nonlinear for strongly forced waves ($u_*/c > 0.1$). Accordingly, a quadratic dependence (e.g., Janssen, 1991) of the wind-induced growth rate on the wind forcing parameter (u_*/c) is more realistic than a formulation based on a linear relationship (e.g., Snyder et al., 1981; Komen et al., 1984). To comply with the “closure mechanism” of wave action spectral energy, the tunable parameters for the whitecapping term (i.e., C_{ds} and δ) used by Rogers et al. (2003) were also slightly recalibrated herein.

Because of the relatively smaller geographic scale of this area, with a regional-scale O (100 km) domain, and because of its weaker wind conditions (U_{10} is usually less than 20 m/s), the intensity of wave energy dissipation from whitecapping (e.g., 15 W/m^2 maximum) in Lake Michigan is lower than that in the Gulf of Mexico (e.g., 20 W/m^2 maximum; Huang et al., 2013). However, the energy dissipation transitional zone (20 m < water depth < 40 m) that converts from whitecapping to depth-induced breaking was found to be similar in both domains. Consequently, the wave statistics for shallow-water stations were insensitive to modification by the whitecapping term, but strongly dependent upon the treatment of the depth-induced breaking term. By considering monthly lake level variations and decreasing the breaker index γ_{BJ} of the default BJ78 model, or by using an alternative TG83 model, the RB scores for the shallowest-water station 45018 were reduced from 0.37 to 0.34, 0.12, and 0.19, respectively. However, a slight decrease in the statistical accuracy of SWH was detected for the southeastern shore station 45026. Because of the complexity of wind–wave–bathymetry interactions, distinct wave growth conditions between the southwestern (45018) and southeastern (45026) locations may require different treatments for the breaker index (Van der Westhuysen, 2010). Under the conditions of finite water depth (with offshore winds near the southeastern coast) and sloping surf (with onshore winds near the southwestern coast), the responding statistical scores (i.e., the RB and SI) indicate an optimal minimum and a constantly increasing trend when the breaker index of the BJ78 model is decreased. The breaker indices for the BJ78 and TG83 models were rescaled to different values ($\gamma_{BJ} = 0.3$ and $\gamma_{TG} = 0.42$) for the depth-induced breaking term because they adopt different assumptions of the probability density function for breaking waves (Van der Westhuysen, 2010; Salmon et al., 2015).

One of our key findings is that the wind data used as model input (GEM, CFSv2, and NNM) show better agreement with the NDBC buoy data at mid-lake than along the lake's shoreline, most likely because the wind speeds at the land–lake interface are highly dynamic and complex, with abrupt transitions of the atmospheric boundary layer (Schwab and Morton, 1984) and/or the short-fetch, limited wave growth conditions (Breugem and Holthuijsen, 2007). In addition, the traditional wind input formulation adopted in the current third-generation wave model may overestimate the transfer of momentum in a young wind-wave field, which would limit the level of model improvement for this region (Donelan et al., 2006; van der Westhuysen et al., 2007). Alves et al. (2014) indicated that a wave model (e.g., GLERL or WW3) with improved physical parameterization for short-fetch wave growth could potentially yield superior storm wave simulation for the Great Lakes system. Based on these considerations, a thorough analysis and revisitation of energy transfer and wind–wave–bathymetry interactions in Lake Michigan would likely be a worthwhile future endeavor.

It must be emphasized that wave–current interactions (WCI) may have significant impacts on wave dynamics through a variety of processes (e.g., alteration of wave age and energy dissipation by the presence of current, or depth- and current-induced wave frequency shifting and refraction). However, the noticeable influence of these effects is largely confined to extremely shallow regions where current intensity and water depth variation are appreciable, as in tidal inlet areas (Van der Westhuysen, 2012; Van der Westhuysen et al., 2012; Dodet et al., 2013). In a large, semi-enclosed or enclosed basin, this effect might be neglected because of relatively weaker current conditions and the absence of tidal modulation on water depth (e.g., wetting and drying processes). Benetazzo et al. (2013) showed that the SWH variation caused by the following/opposite currents in the Adriatic Sea (a semi-enclosed basin) was 0.1 m and 0.6 m during the weak Sirocco and strong Bora events, respectively. In Lake Michigan, storm waves are affected to some degree by WCI, but it is of secondary importance compared to the variations that result from using alternative wind field sources and different formulations to describe deep- and shallow-water wave physics (not shown here). Moreover, changes to the statistical indices (i.e., the RB, SI, CC, NSTD, and RMSD) for SWH and PWP values caused by the WCI effect over a long-term (eight months) wave simulation are insignificant (Figs. 16a–b). Furthermore, the WCI-coupled model only achieves a slightly faster computational speed than the wave-only model at the cost of six times the computational cores (Table 4); therefore, the recalibrated wave-only model was selected to apply in this study. We do suggest, however, that it may be of interest in the future to explore the effects of WCI under storm conditions for shallower lakes (e.g., Lake Erie where the average water depth is 19 m), particularly during periods of high storm surges and intense currents.

6. Conclusions

This study investigated factors that lead to the improvement of a third-generation spectral wind-wave SWAN model for Lake Michigan. We compared observational data for SWHs and PWPs from the NDBC buoys to values produced through models using various sources for wind fields, alternative settings for deep- and shallow-water wave physics, and different mesh types. The main conclusions are:

(1) The GEM atmospheric model yields a spatially coherent wind field (i.e., smooth gradient of wind intensity) over the lake, whereas the observation-based NNM wind field agrees strongly with the NDBC buoy-recorded data. Consequently, the un-SWAN model driven by the GEM wind data captures extreme waves in the mid-lake region more accurately, while the model that uses the NNM wind data reproduces the SWHs along the lake's shoreline more accurately.

(2) Whitecapping dissipation is dominant in deep water (water depth > 40 m), whereas depth-induced breaking is the primary dissipation mechanism in the nearshore regions (10 m < water depth ≤ 20 m). Based on the GEM wind data, the un-SWAN model with the wind input formulation of Janssen (1991) and the recalibrated whitecapping formulation of Rogers et al. (2003) provided the best agreement with buoy observations at mid-lake and intermediate-water stations, especially for extreme wave heights. In the extreme shallow-water region, model improvement is achieved by reducing the breaker index γ_{BJ} or adopting the TG83 model for depth-induced breaking.

(3) Mesh types (specifically the OC SWAN and MR un-SWAN meshes) clearly affect the modeling of wave dynamics in nearshore regions characterized by complex bathymetry and irregular geometry. The MR un-SWAN model not only captures the wave processes from deep to shallow waters as accurately as the HR version, but it also greatly outperforms the OC SWAN model for nearshore waves. The model with the MR unstructured mesh configuration was found to be the most accurate and computationally efficient choice for Lake Michigan wave simulation.

Acknowledgements

This project was supported by a National Science Foundation grant to M.X (No. 1238044). We thank our reviewers for helpful comments that improved the manuscript. We also thank Gregory Lang for useful comments on processing NDBC buoy data. The GEM and NNM wind fields are available upon request to Miguel Tremblay (dps-client@ec.ga.ca) from the Canadian Meteorological Centre and from Gregory Lang (gregory.lang@noaa.gov) of NOAA-GLERL, respectively. The CFSv2 wind field data can be obtained by registering and making a request through the NCAR Computational & Information Systems Lab (CISL) Research Data Archive interface (rda.ucar.edu). The buoy records (including hourly wind speed, significant wave height, peak wave period, and mean wave direction) and monthly-averaged lake level data for Lake Michigan can be obtained from NOAA's NDBC (www.ndbc.noaa.gov) and GLWLD (http://www.glerl.noaa.gov/data/dashboard/GLWLD.html), respectively. Numerical experiments were supported by and carried out with the NCAR CISL and the Texas Advanced Computing Center (TACC) Stampede Supercomputer. Please contact the corresponding author at mxia@umes.edu with requests for the numerical results discussed in this manuscript.

References

Alves, J. H. G., A. Chawla, H. L. Tolman, D. J. Schwab, G. Lang, and G. Mann (2014), The Operational Implementation of a Great Lakes Wave Forecasting System at NOAA/NCEP, *Weather Forecast.*, 29(6), 1473–1497.

Battjes, J. A. and J. P. F. M Janssen (1978), Energy loss and set-up due to breaking of random waves, in *Coastal Engineering*, 1978, pp. 569–588, Am. Soc. Civil Eng., New York.

Beletsky, D., and D. J. Schwab (2001), Modeling circulation and thermal structure in Lake Michigan: Annual cycle and interannual variability, *J. Geophys. Res.*, 106(C9), 19745–19771.

Beletsky, D., and D. J. Schwab (2008), Climatological circulation in Lake Michigan, *Geophys. Res.* Lett., 35(21).

Benetazzo, A., S. Carniel, M. Sclavo, and A. Bergamasco (2013), Wave–current interaction: Effect on the wave field in a semi-enclosed basin, *Ocean Model.*, 70, 152–165.

Booij, N., R. C. Ris, and L. H. Holthuijsen (1999), A third-generation wave model for coastal regions: 1. Model description and validation, *J. Geophys. Res.*, 104(C4), 7649–7666.

Breugem, W. A. and L. H. Holthuijsen (2007), Generalized shallow water wave growth from Lake George. *J. Waterw. Port C-ASCE*, 133(3), 173–182.

Cavaleri, L. (2009), Wave modeling—missing the peaks, *J. Phys. Oceanogr.*, 39(11), 2757–2778.

Chen, C., L. Wang, R. Ji, J. W. Budd, D. J. Schwab, D. Beletsky, G. L. Fahnenstiel, H. Vanderploeg, B. Eadie, and J. Cotner (2004), Impacts of suspended sediment on the ecosystem in Lake Michigan: A comparison between the 1998 and 1999 plume events, *J. Geophys. Res.*, 109(C10), 1–18.

Collins, J. I. (1972), Prediction of shallow-water spectra, *J. Geophys. Res.*, 77(15), 2693–2707.

Côté, J., S. Gravel, A. Méthot, A. Patoine, M. Roch, and A. Staniforth (1998), The operational CMC-MRB global environmental multiscale (GEM) model. Part I: Design considerations and formulation, *Mon. Weather Rev.*, 126(6), 1373–1395.

Dietrich, J. C., M. Zijlema, P.-E. Allier, L. H. Holthuijsen, N. Booij, J. D. Meixner, J. K. Proft, C. N. Dawson, C. J. Bender, A. Naimaster, J. M. Smith, and J. J. Westerink (2013), Limiters for spectral propagation velocities in SWAN, *Ocean Model.*, 70, 85–102.

Dietrich, J. C., M. Zijlema, J. J. Westerink, L. H. Holthuijsen, C. Dawson, R. A. Luettich, Jr., R. Jensen, J. M. Smith, G. S. Stelling and G. W. Stone (2011), Modelling Hurricane Waves and Storm Surge using Integrally-Coupled, Scalable Computations, *Coast. Eng.*, 58, 45–65.

Dodet, G., X. Bertin, N. Bruneau, A. B. Fortunato, A. Nahon, and A. Roland (2013), Wave−current interactions in a wave-dominated tidal inlet, *J. Geophys. Res.*, 118(3), 1587–1605.

Donelan, M. A., A. V. Babanin, I. R. Young, and M. L. Banner (2006), Wave-follower field measurements of the wind-input spectral function. Part II: Parameterization of the wind input, *J. Phys. Oceanogr.*, 36(8), 1672–1689.

Gelci, R. and H. Cazalé (1953), Une théorie énergétique de la houle appliquée au Maroc, *C. R. Soc. Sci. Nat. Phys. Maroc.*, (4), 64–66.

Gronewold, A. D. and C. A. Stow (2014), Water loss from the Great Lakes, *Science*, 343(6175), 1084–1085.

Hasselmann, K. et al. (1973), Measurements of wind-wave growth and swell decay during the Joint North Sea Wave Project (JONSWAP), *Deutsche Hydrographische Zeitschrift,* A12, 95.

Hasselmann, K. (1974), On the spectral dissipation of ocean waves due to white capping, *Bound.-Lay. Meteorol.*, 6(1–2), 107–127.

He, R., Y. Liu, and R. H. Weisberg (2004), Coastal ocean wind fields gauged against the performance of an ocean circulation model, *Geophys. Res. Lett.*, 31(14).

Huang, Y., R. H. Weisberg, L. Zheng, and M. Zijlema (2013), Gulf of Mexico hurricane wave simulations using SWAN: Bulk formula-based drag coefficient sensitivity for Hurricane Ike, *J. Geophys. Res.*, 118(8), 3916–3938.

Janssen, P. A. E. M. (1991), Quasi-linear theory of wind-wave generation applied to wave forecasting, *J. Phys. Oceanogr.*, 21(11), 1631–1642.

Janssen, P. A. E. M. (1992), Consequences of the effect of surface gravity waves on the mean air flow. Breaking Waves: IVTAM Symposium, Sydney, Australia, 1991, *M. L. Banner and R. H. J. Grimshaw, Eds.*, *Springer-Verlag*, 193–198.

Jensen, R. E., M. A. Cialone, R. S. Chapman, B. A. Ebersole, M. Anderson, and L. Thomas (2012), Lake Michigan Storm: Wave and Water Level Modeling (No. ERDC/CHL-TR-12-26), U.S. Army Engineer Research and Development Center Coastal and Hydraulics Laboratory, Vicksburg, MS.

Kerr, P. C., R. C. Martyr, A. S. Donahue, M. E. Hope, J. J. Westerink, R. A. Luettich, and H. J. Westerink (2013), US IOOS coastal and ocean modeling testbed: Evaluation of tide, wave, and hurricane surge response sensitivities to mesh resolution and friction in the Gulf of Mexico, *J. Geophys. Res.*, 118(9), 4633–4661.

Komen, G. J., S. Hasselmann, and K. Hasselmann (1984), On the existence of a fully developed wind-sea spectrum, *J. Phys. Oceanogr.*, 14(8), 1271–1285.

Lang, G. A. and G. A. Leshkevich (2014), Persistent wind fields over the Great Lakes, 2002-2013, 57th Annual Conference on Great Lakes Research, May 26–30, 2014, McMaster University, Hamilton, Ontario, Canada.

Large, W. G. and S. Pond (1981), Open ocean momentum flux measurements in moderate to strong winds, *J. Phys. Oceanogr.*, 11(3), 324–336.

Lou, J., D. J. Schwab, D. Beletsky, and N. Hawley (2000), A model of sediment resuspension and transport dynamics in southern Lake Michigan, *J. Geophys. Res*., 105(C3), 6591–6610.

Madsen, O. S., Y. K. Poon, and H. C. Graber (1988), Spectral wave attenuation by bottom friction: Theory, *Proc. 21th Int. Conf. Coast. Eng.*, ASCE, 492–504.

Massey, T. C., M. E. Anderson, J M Smith, J. Gomez, and R. Jones (2011), STWAVE: Steady-state spectral wave model user's manual for STWAVE, version 6.0. ERDC/CHL SR-11-1. U.S. Army Engineer Research and Development Center, Vicksburg, MS.

Nelson, R. C. (1987), Design wave heights on very mild slopes-an experimental study, *Civil Eng. Trans. Inst. Eng. Aust.*, 29(3), 157–161.

Oey, L.-Y., T. Ezer, D. P. Wang, S. J. Fan, and X. Q. Yin (2006), Loop current warming by Hurricane Wilma, *Geophys. Res. Lett.*, 33(8).

Pierson, W. J. and L. Moskowitz (1964), A proposed spectral form for fully developed wind seas based on the similarity theory of S. A. Kitaigorodskii, *J. Geophys. Res.*, 69(24), 5181–5190.

Powell, M. D., P. J. Vickery, and T. A. Reinhold (2003), Reduced drag coefficient for high wind speeds in tropical cyclones, *Nature*, 422(6929), 279–283.

Rogers, W. E., A. V. Babanin, and D. W. Wang (2012), Observation-consistent input and whitecapping dissipation in a model for wind-generated surface waves: description and simple calculations, *J. Atmos. Ocean. Tech.*, 29(9), 1329–1346.

Rogers, W. E., P. A. Hwang, and D. W. Wang (2003), Investigation of Wave Growth and Decay in the SWAN Model: Three Regional-Scale Applications, *J. Phys. Oceanogr.*, 33(2), 366–389.

Rogers, W. E., J. M. Kaihatu, L. Hsu, R. E. Jensen, J. D. Dykes, and K. T. Holland (2007), Forecasting and hindcasting waves with the SWAN model in the Southern California Bight, *Coast. Eng.*, 54(1), 1–15.

Ruessink, B. G., D. J. R. Walstra, and H. N. Southgate (2003), Calibration and verification of a parametric wave model on barred beaches, *Coast. Eng.*, 48(3), 139–149.

Saha, S. et al. (2014), The NCEP climate forecast system version 2, *J. Climate*, 27(6), 2185–2208.

Salmon, J. E., L. H. Holthuijsen, M. Zijlema, G. P. van Vledder, and J. D. Pietrzak (2015), Scaling depth-induced wave-breaking in two-dimensional spectral wave models, *Ocean. Model.,* 87, 30–47.

Schwab, D. J., D. Beletsky, and J. Lou (2000), The 1998 coastal turbidity plume in Lake Michigan, *Estuar. Coast. Shelf S.*, 50(1), 49–58.

Schwab, D. J. and J. A. Morton (1984), Estimation of overlake wind speed from overland wind speed: A comparison of three methods, *J. Great Lakes Res.*, 10(1), 68–72.

Sellinger, C. E., C. A. Stow, E. C. Lamon, and S. S. Qian (2007), Recent water level declines in the Lake Michigan−Huron System, *Environ. Sci. Technol*., 42(2), 367–373.

SWAN Group (2012a), SWAN Scientific and Technical Documentation — SWAN Cycle III version 40.91, C3, P43–P51, Delft University of Technology, Delft, Netherlands. [Available at http://www.swan.tudelft.nl/]

SWAN Group (2012b), SWAN User Manual-SWAN Cycle III version 40.91, C4, P55–56, Delft University of Technology, Delft Netherlands. [Available at http://www.swan.tudelft.nl/]

Snyder, R. L., F. W. Dobson, J. A. Elliott, and R. B. Long (1981), Array measurements of atmospheric pressure fluctuations above surface gravity waves, *J. Fluid Mech.*, 102, 1–59.

Taylor, K. E. (2001), Summarizing multiple aspects of model performance in a single diagram, *J. Geophys. Res.*, 106(D7), 7183–7192.

Thornton, E. B., and R. T. Guza (1983), Transformation of wave height distribution, *J. Geophys. Res.*, 88(C10), 5925–5938.

Tolman, H. L. (2002), User manual and system documentation of WAVEWATCH III version 2.22, Environmental Modeling Center, Marine Modeling and Analysis Brach, NOAA.

Van der Westhuysen, A. J. (2010), Modeling of depth-induced wave breaking under finite depth wave growth conditions, *J. Geophys. Res.*, 115(C1).

Van der Westhuysen, A. J. (2012), Spectral modeling of wave dissipation on negative current gradients. *Coast. Eng.*, 68, 17–30.

Van der Westhuysen, A. J., A. R. Dongeren, J. Groeneweg, G. P. van Vledder, H. Peters, C. Gautier, and J. C. C. Nieuwkoop (2012), Improvements in spectral wave modeling in tidal inlet seas*, J. Geophys. Res.*, 117(C11), C00J28.

Van der Westhuysen, A. J., M. Zijlema, and J. A. Battjes (2007), Nonlinear saturation-based whitecapping dissipation in SWAN for deep and shallow water, *Coast. Eng.*, 54(2), 151–170.

Wu, J. (1982), Wind-stress coefficients over sea surface from breeze to hurricane, *J. Geophys. Res.*, 87(C12), 9704–9706.

Yan, L. (1987), An improved wind input source term for third generation ocean wave modeling, *Royal Dutch Meteorol. Inst.*, Rep., No. 87–8.

Zijlema, M. (2010), Computation of wind-wave spectra in coastal waters with SWAN on unstructured grids, *Coast. Eng.*, 57(3), 267–277.

List of tables and figures

Table 1 Model meshes and geometric information for Lake Michigan.

Table 2 Locations and water depths for the NDBC buoys of Lake Michigan.

Table 3 MR un-SWAN model cases with different wind field sources, settings for wind input and whitecapping dissipation, and depth-induced breaking terms.

Table 4 Computational speed of wave models with different mesh types for Lake Michigan wave simulations of the year 2011.

Fig. 1. Maps of (a) the Great Lakes system and (b) Lake Michigan. Note that the red solid line in panel (a) marks the Canada–U.S.A. border.

Fig. 2. Bathymetry and computational meshes for Lake Michigan: (a) Bathymetry and NDBC buoy stations, (b) orthogonal curvilinear grid, (c) unstructured triangular mesh with medium resolution, and (d) with high resolution. The black lines represent the coast and island outlines.

Fig. 3a. Rose diagrams for wind (left column) and SWH (right column) directions for the northern mid-lake (45002), southern mid-lake (45007), and near mid-eastern (45029) and southeastern (45026) coasts, from the top panels to the bottom.

Fig. 3b. Rose diagrams for wind directions at locations near the southwestern (FSTI2), mid-western (45013), northwestern (0Y2W3; left panels), and northeastern coasts (45024), and in Little Traverse Bay (45022) and Green Bay (45014; right panels).

Fig. 4. Monthly-averaged (a) SWH and (b) wind speed of NDBC *in-situ* buoys in the northern (45002) and southern mid-lake areas (45007), in Green Bay (45014) and Little Traverse Bay (45022), and near the western (45013 and 0Y2W3) and eastern coasts (45024, 45026, 45029, and 45161).

Fig. 5a Scatterplots of wind speeds determined by the NNM ($U_{10,NNM}$) versus observed values ($U_{10,obs}$) at various NDBC buoys. Note that because no wind data are available from NDBC stations 45015, 45016, and 45018, the observed winds from the adjacent FSTI2 station are used.

Fig. 5b. Scatterplots of SWH ($H_{sig,NNM}$) values from the un-SWAN model with NNM winds versus observed values ($H_{sig,obs}$) taken at various NDBC buoys.

Fig. 6a. Scatterplots of SWHs from the un-SWAN model with the default ($H_{sig,dft}$) and recalibrated settings ($H_{sig,rec}$) versus SWH observational data ($H_{sig,obs}$) taken at various NDBC buoys in 2012.

Fig. 6b. Same as Fig. 6a except for that SWH (H_{sig}) is replaced by PWP (T_{peak}).

Fig. 7. Taylor diagrams summarizing the CC, NSTD, and RMSD values for un-SWAN model estimations with default (green) and recalibrated settings (red) compared with NDBC *in-situ* observations for (a) SWH and (b) PWP.

Fig. 8 Time series of (a) wind speed and (b) wind direction taken from the GEM and NNM fields, and (c) SWH, (d) PWP, and (e) MWD determined through the un-SWAN models driven by these two fields compared with observations taken at various NDBC buoys during Superstorm Sandy (2012). Note: Cartesian conventions are adopted here for wind direction.

Fig. 9. Spatial distributions of (a) water depth and maximum (b) total energy dissipation, (c) whitecapping dissipation, and (d) depth-induced wave breaking during Superstorm Sandy (2012).

Fig. 10a. Scatterplots of wind speeds from the GEM ($U_{10,GEM}$; top), CFSv2 ($U_{10,CFSv2}$; middle), and NNM ($U_{10,NNM}$; bottom) wind fields versus observed wind speed values ($U_{10,obs}$) taken at various NDBC buoys. Note: because no wind data are available at station 45018, the observed winds from the adjacent FSTI2 station are used.

Fig. 10b. Scatterplots of modeled SWH values from the un-SWAN model with default deep-water wave growth formulation (Komen et al., 1984) driven by the GEM ($H_{sig,GEM+WAM3}$; top panel), CFSv2 ($H_{sig,CFSv2+WAM3}$; middle panel), and NNM wind fields ($H_{sig,NNM+WAM3}$; bottom panel) versus observations of SWH ($H_{sig,obs}$) from various NDBC buoys.

Fig. 11. Spatial distributions of the maximum wind speeds determined with the (a) GEM, (b) CFSv2, and (c) NNM wind fields, and corresponding SWHs (d–f), during a 2011 clipper storm. Note that black crosses denote the locations of mid-lake buoys 45002 and 45007, and that black circles cover the adjacent interpolation smoothing distance (30 km) for the NNM.

Fig. 12a. Scatterplots of modeled SWHs from the un-SWAN model with various wind input and whitecapping settings versus observed SWH values ($H_{sig,obs}$) taken at various

NDBC buoys. The top, middle, and bottom panels are $H_{sig,C1a}$, $H_{sig,C1b}$, and $H_{sig,C1c}$ for the Case 1a (Komen et al., 1984), Case 1b (recalibrated Rogers et al., 2003), and Case 1c (van der Westhuysen et al., 2007) formulations for deep-water wave physics, respectively.

Fig. 12b. Same as Fig. 12a except for that SWH (H_{sig}) is replaced with PWP (T_{peak}).

Fig. 12c. Same as Fig. 12a except for that the SWH values (H_{sig}) are replaced with extreme values (above the 99.5th percentile) from the mid-lake buoys 45002 and 45007.

Fig. 13. Scatterplots of modeled SWHs from the un-SWAN model with various depth-induced breaking settings versus observed SWH values ($H_{sig,obs}$) taken at the shallow-water buoys 45018 and 45022. The top, middle, and bottom panels are $H_{sig,C2a}$, $H_{sig,C2b}$, and $H_{sig,C2c}$ from Case 2a (the BJ78 model with default $\gamma_{BJ} = 0.3$), Case 2b (the BJ78 model with a decreased $\gamma_{BJ} = 0.3$), and Case 2c (the TG83 model with default $\gamma_{TG} = 0.42$) for estimating shallow-water wave physics, respectively.

Fig. 14. Scatterplots of modeled SWHs, ($H_{sig,OC}$, $H_{sig,MR}$, and $H_{sig,HR}$) from the wave model using orthogonal curvilinear (top panel), medium- (middle panel), and high-resolution (bottom panel) meshes, respectively, versus observed SWH values ($H_{sig,obs}$) taken at various NDBC buoys.

Fig. 15. Spatial distributions of the maximum (a) wind speed and (b) SWH, and the differences in percentages of SWHs from (c) the MR un-SWAN results minus the HR un-SWAN results, and (d) the OC SWAN results minus the HR un-SWAN results, during a clipper storm in 2011. Note the difference in scale between panels (c) and (d).

Fig. 16a. Scatterplots of modeled SWHs from the recalibrated wave-only ($H_{sig,rec}$; first and third rows) and wave–current interactions (WCI) coupled models ($H_{sig,rec+WCI}$; second and fourth rows) versus observed SWH values ($H_{sig,obs}$) taken at various NDBC buoys in 2012.

Fig. 16b. Scatterplots of modeled PWPs from the recalibrated wave-only ($T_{peak,rec}$; first and third rows) and wave–current interactions (WCI) coupled models ($T_{peak,rec+WCI}$; second and fourth rows) versus observed PWP values ($T_{peak,obs}$) taken at various NDBC buoys in 2012.

Table 1 Model meshes and geometric information for Lake Michigan.

Model mesh type / Model information	Orthogonal Curvilinear (OC) SWAN	Medium-resolution (MR) un-SWAN	High-resolution (HR) un-SWAN
Elements/Cells	52,975	9,581	38,324
Nodes	52,975 (163 × 325)	5,256	20,108
Grid Resolution (water depth ≤ 20 m)	1.8 × 1.8 km	0.34–4.4 km	0.21–2.2 km
Grid Resolution (20 m < water depth ≤ 50 m)		0.34–7.1 km	0.22–3.6 km
Grid Resolution (water depth > 50 m)		0.44–7.6 km	0.22–3.8 km
Average Water Depth	85 m		
Lake Width	259 km		
Lake Length	493 km		

Table 2 Locations and water depths for the NDBC buoys of Lake Michigan.

Station		Data source	Data availability years	Longitude (°)	Latitude (°)	Water depth (m)
1	45002	NDBC	2002–2012	-86.411	45.344	175.3
2	45014	Univ. W-M	2012	-87.760	44.800	13
3	0Y2W3	USCG	2012	-87.313	44.794	5.4
4	C58W3	USCG	2012	-87.563	44.146	5.9
5	45013	Univ. W-M	2012	-87.850	43.100	20
6	45018/ FSTI2	Chicago Park District	2011–2012	-87.637	41.968	3.9
7	45016	Chicago Park District	2011–2012	-87.573	41.783	4.8
8	45015	Chicago Park District	2011–2012	-87.527	41.714	3.5
9	45026	Limno Tech	2011–2012	-86.617	41.983	20.7
10	45007	NDBC	2002–2012	-87.026	42.674	160
11	45029	Limno Tech	2012	-86.272	42.900	27
12	45161	GLERL	2012	-86.361	43.178	25
13	45024	UM CILER	2012	-86.559	43.977	30.3
14	45022	MTU	2011–2012	-85.088	45.403	49.1

Table 3 MR un-SWAN model cases with different wind field sources, settings for wind input and whitecapping dissipation, and depth-induced breaking terms.

Case	Wind field source	Wind input	Whitecapping dissipation	Depth-induced breaking formulation	Spatial lake level
Case1a (default)	NNM	Snyder et al. (1981)	Komen et al. (1984) $C_{ds} = 2.36 \times 10^{-5}$ $\delta = 0$	Battjes and Janssen (1978) $\gamma_{BJ} = 0.73$	Constant
Case1b	GEM	Janssen (1991)	Readjusted Rogers et al. (2003) $C_{ds} = 3.0 \times 10^{-5}$ $\delta = 0.3$	Battjes and Janssen (1978) $\gamma_{BJ} = 0.73$	Constant
Case 1c	GEM	Refitted Yan (1987)	Van der Westhuysen et al. (2007) $C_{ds} = 5.0 \times 10^{-5}$ $B_r = 1.75 \times 10^{-3}$	Battjes and Janssen (1978) $\gamma_{BJ} = 0.73$	Constant
Case 2a	GEM	Janssen (1991)	Readjusted Rogers et al. (2003) $C_{ds} = 3.0 \times 10^{-5}$ $\delta = 0.3$	Battjes and Janssen (1978) $\gamma_{BJ} = 0.73$	Monthly variable
Case 2b	GEM	Janssen (1991)	Readjusted Rogers et al. (2003) $C_{ds} = 3.0 \times 10^{-5}$ $\delta = 0.3$	Battjes and Janssen (1978) $\gamma_{BJ} = 0.3$	Monthly variable
Case 2c (recali-brated)	GEM	Janssen (1991)	Readjusted Rogers et al. (2003) $C_{ds} = 3.0 \times 10^{-5}$ $\delta = 0.3$	Thornton and Guza (1983) $\gamma_{TG} = 0.42$	Monthly variable

Table 4 Computational speed of wave models with different mesh types for Lake Michigan wave simulations of the year 2011.

Model type	HPCC System	Core number	Computational time (min/day)
OC SWAN	TACC/ UT Stampede	16	6
MR un-SWAN		16	3
HR un-SWAN		16	15
MR un-SWAN with WCI	CISL Yellowstone	96	2.5

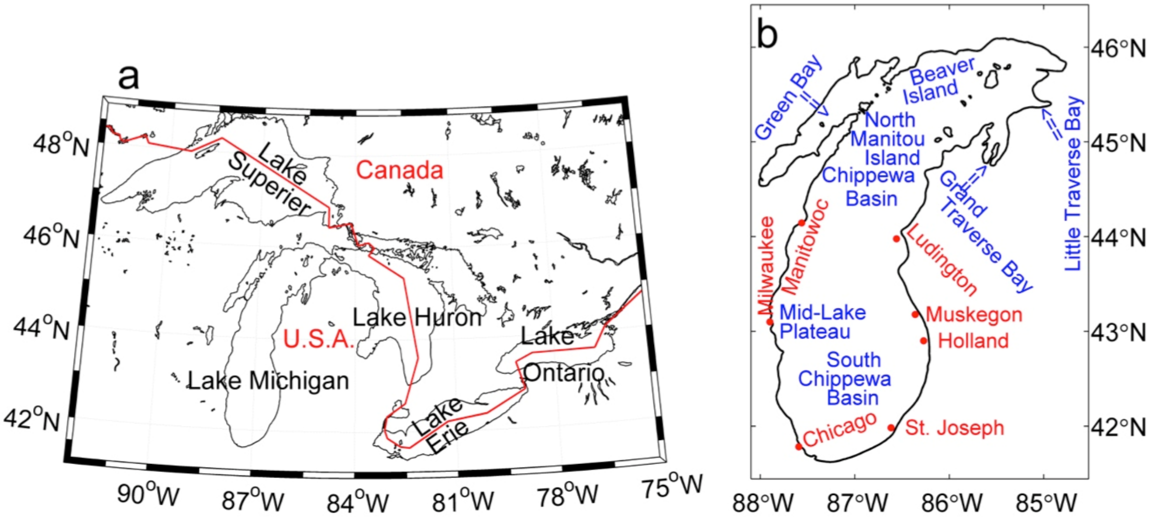

Fig. 1. Maps of (a) the Great Lakes system and (b) Lake Michigan. Note that the red solid line in panel (a) marks the Canada–U.S.A. border.

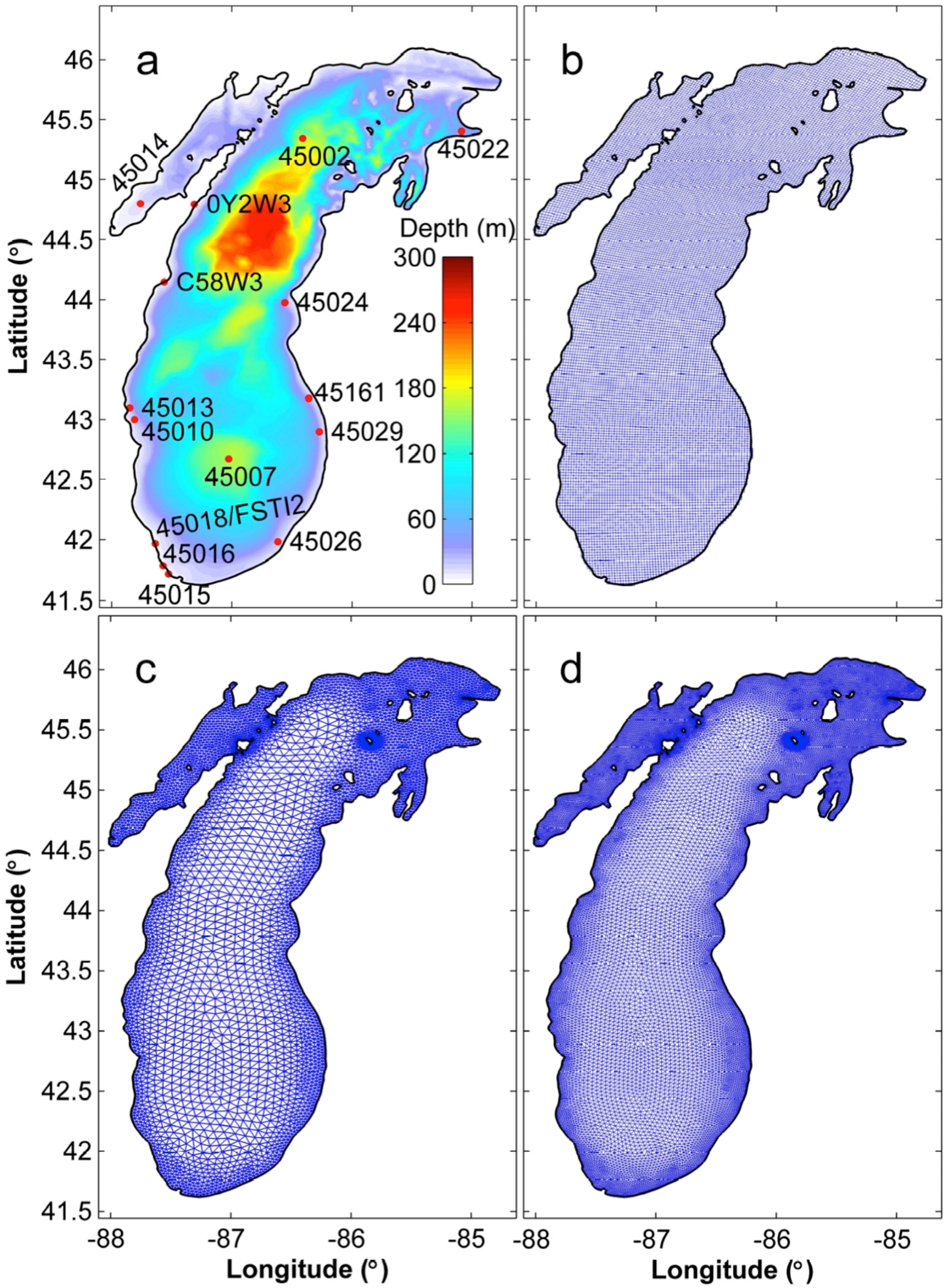

Fig. 2. Bathymetry and computational meshes for Lake Michigan: (a) Bathymetry and NDBC buoy stations, (b) orthogonal curvilinear grid, (c) unstructured triangular mesh with medium resolution, and (d) with high resolution. The black lines represent the coast and island outlines.

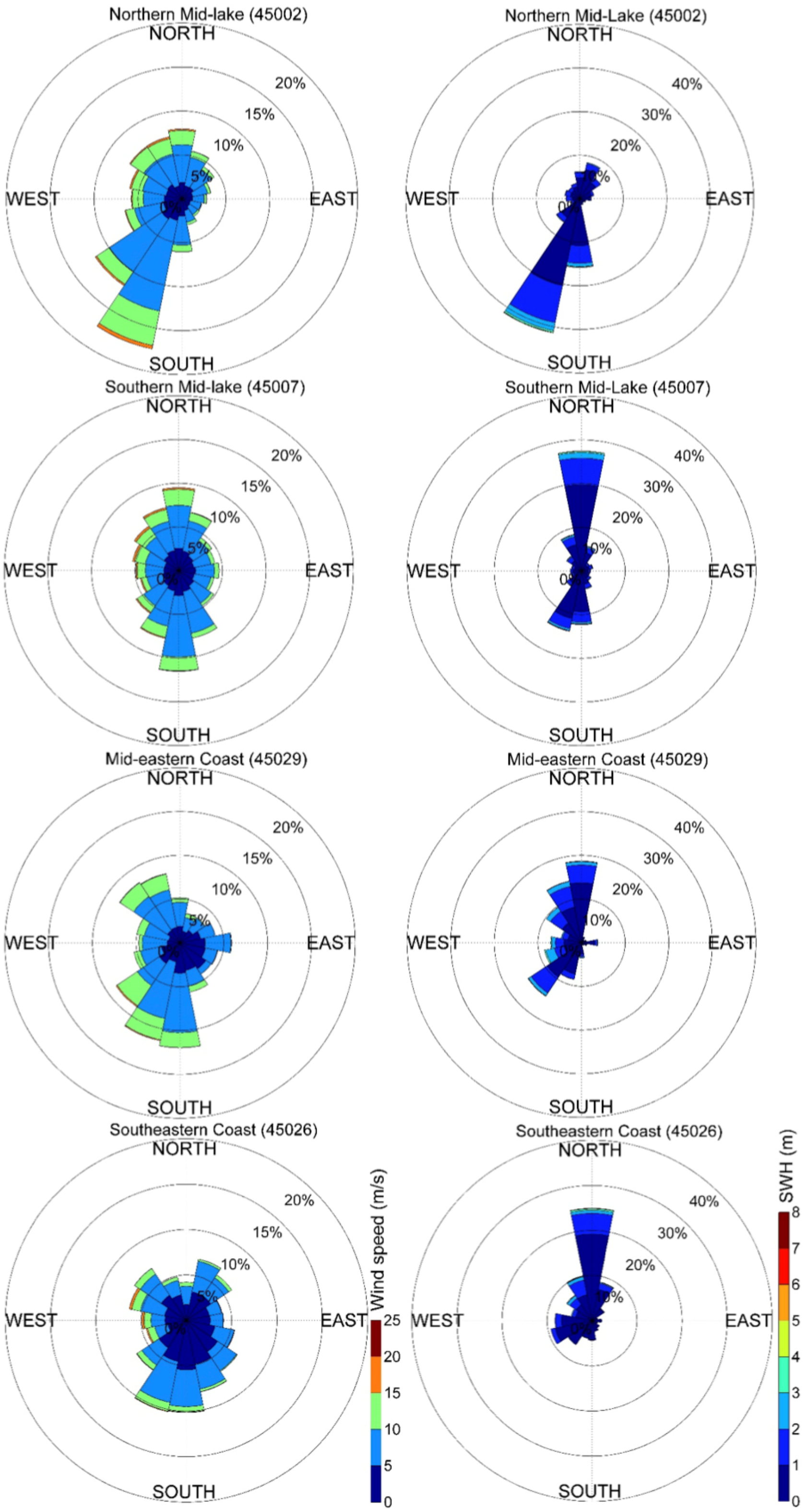

Fig. 3a. Rose diagrams for wind (left column) and SWH (right column) directions for the northern mid-lake (45002), southern mid-lake (45007), and near mid-eastern (45029) and southeastern (45026) coasts, from the top panels to the bottom.

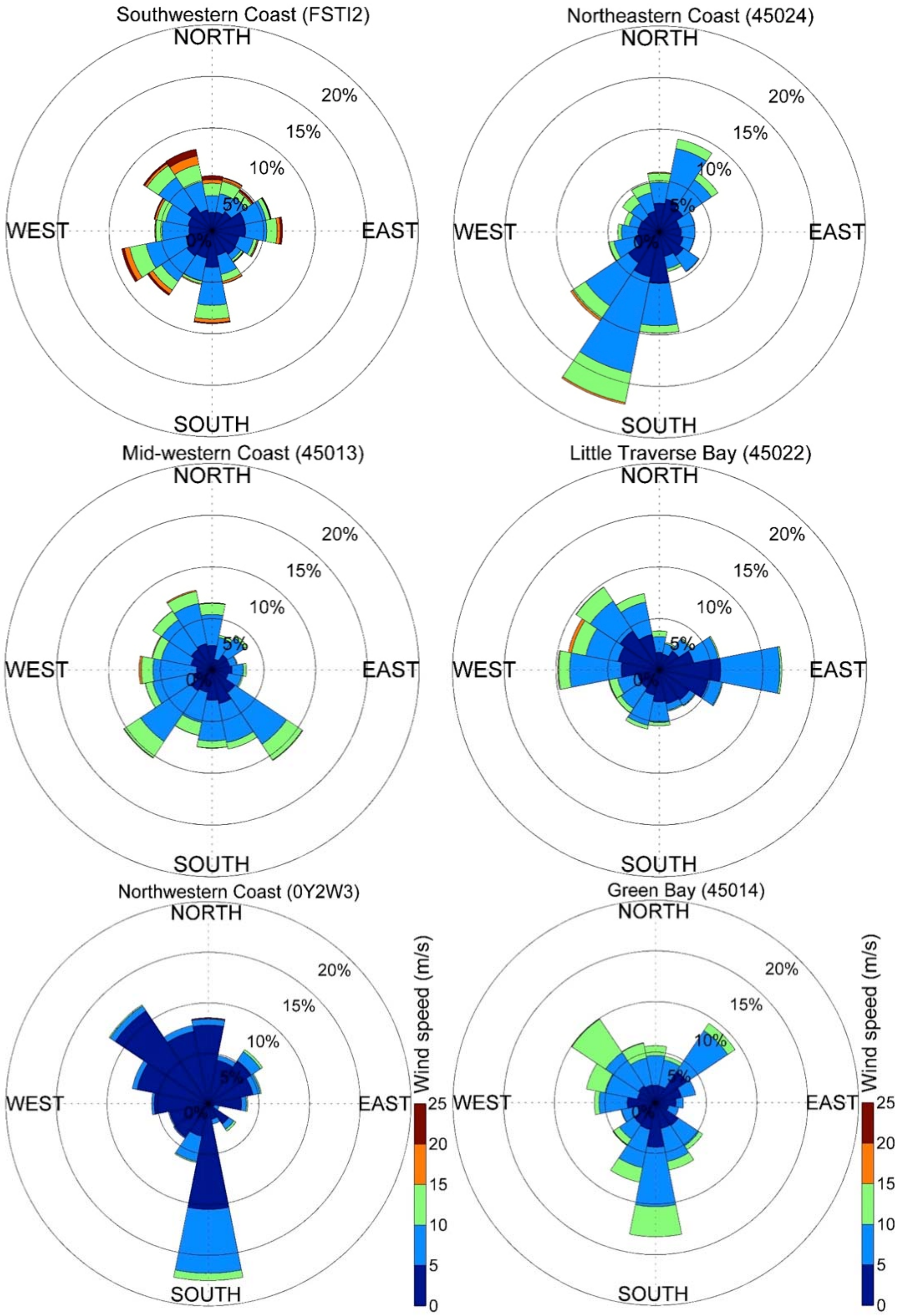

Fig. 3b. Rose diagrams for wind directions at locations near the southwestern (FSTI2), mid-western (45013), northwestern (0Y2W3; left panels), and northeastern coasts (45024), and in Little Traverse Bay (45022) and Green Bay (45014; right panels).

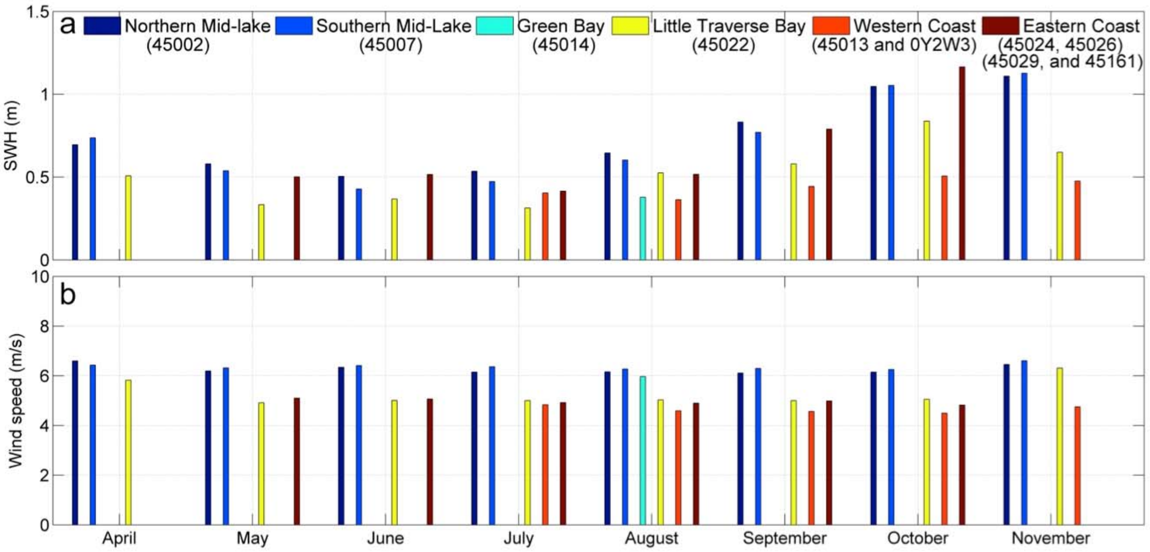

Fig. 4. Monthly-averaged (a) SWH and (b) wind speed of NDBC *in-situ* buoys in the northern (45002) and southern mid-lake areas (45007), in Green Bay (45014) and Little Traverse Bay (45022), and near the western (45013 and 0Y2W3) and eastern coasts (45024, 45026, 45029, and 45161).

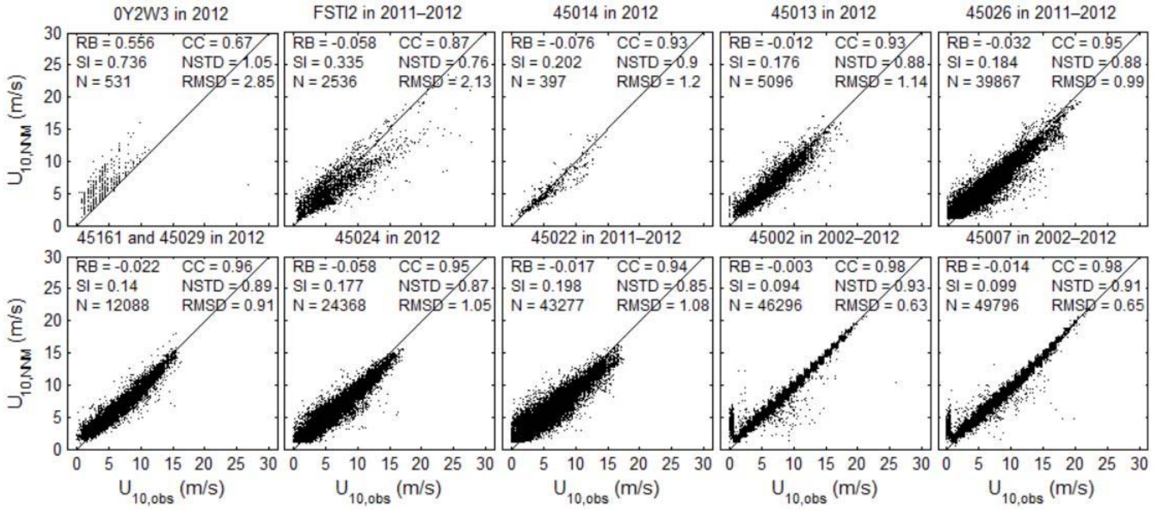

Fig. 5a. Scatterplots of wind speeds determined by the NNM ($U_{10,NNM}$) versus observed values ($U_{10,obs}$) at various NDBC buoys. Note that because no wind data are available from NDBC stations 45015, 45016, and 45018, the observed winds from the adjacent FSTI2 station are used.

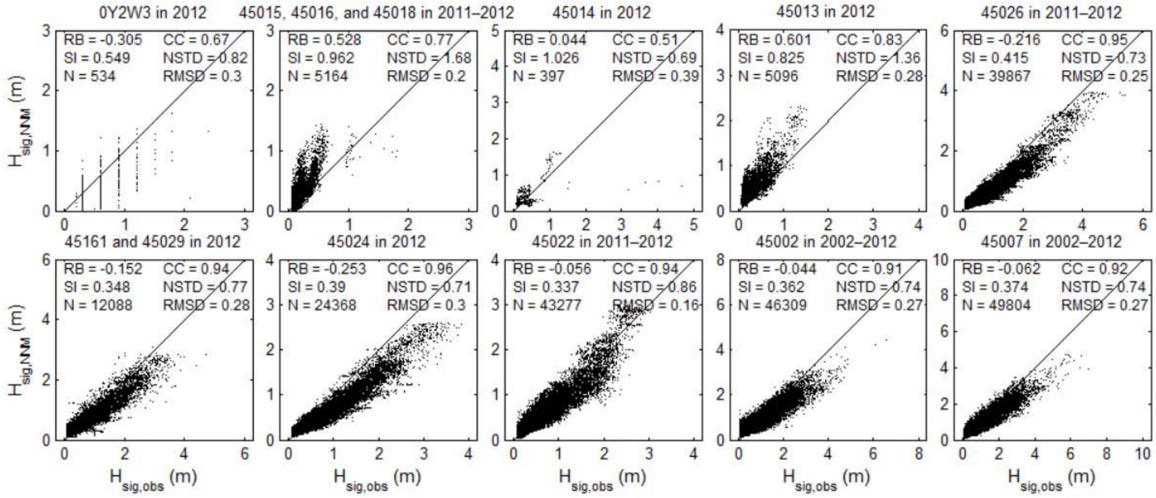

Fig. 5b. Scatterplots of SWH ($H_{sig,NNM}$) values from the un-SWAN model with NNM winds versus observed values ($H_{sig,obs}$) taken at various NDBC buoys.

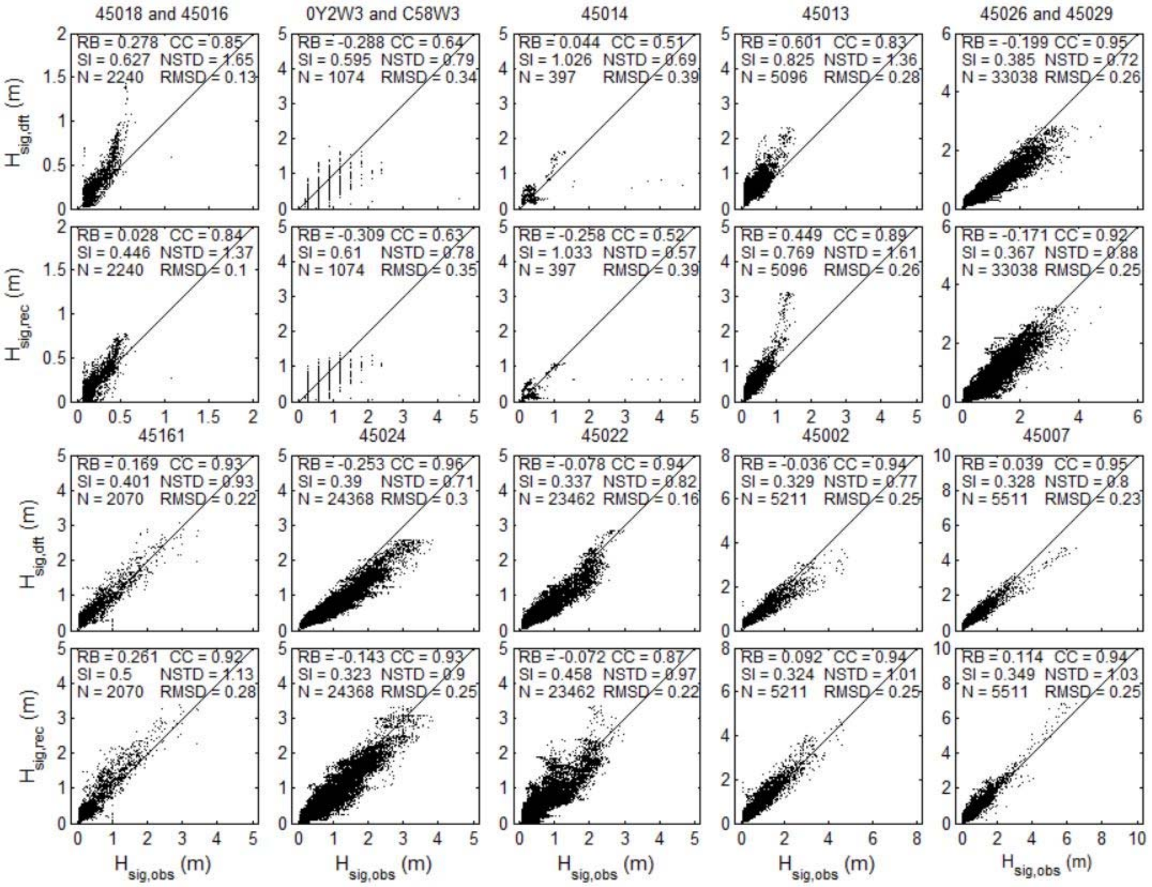

Fig. 6a. Scatterplots of SWHs from the un-SWAN model with the default ($H_{sig,dft}$) and recalibrated settings ($H_{sig,rec}$) versus SWH observational data ($H_{sig,obs}$) taken at various NDBC buoys in 2012.

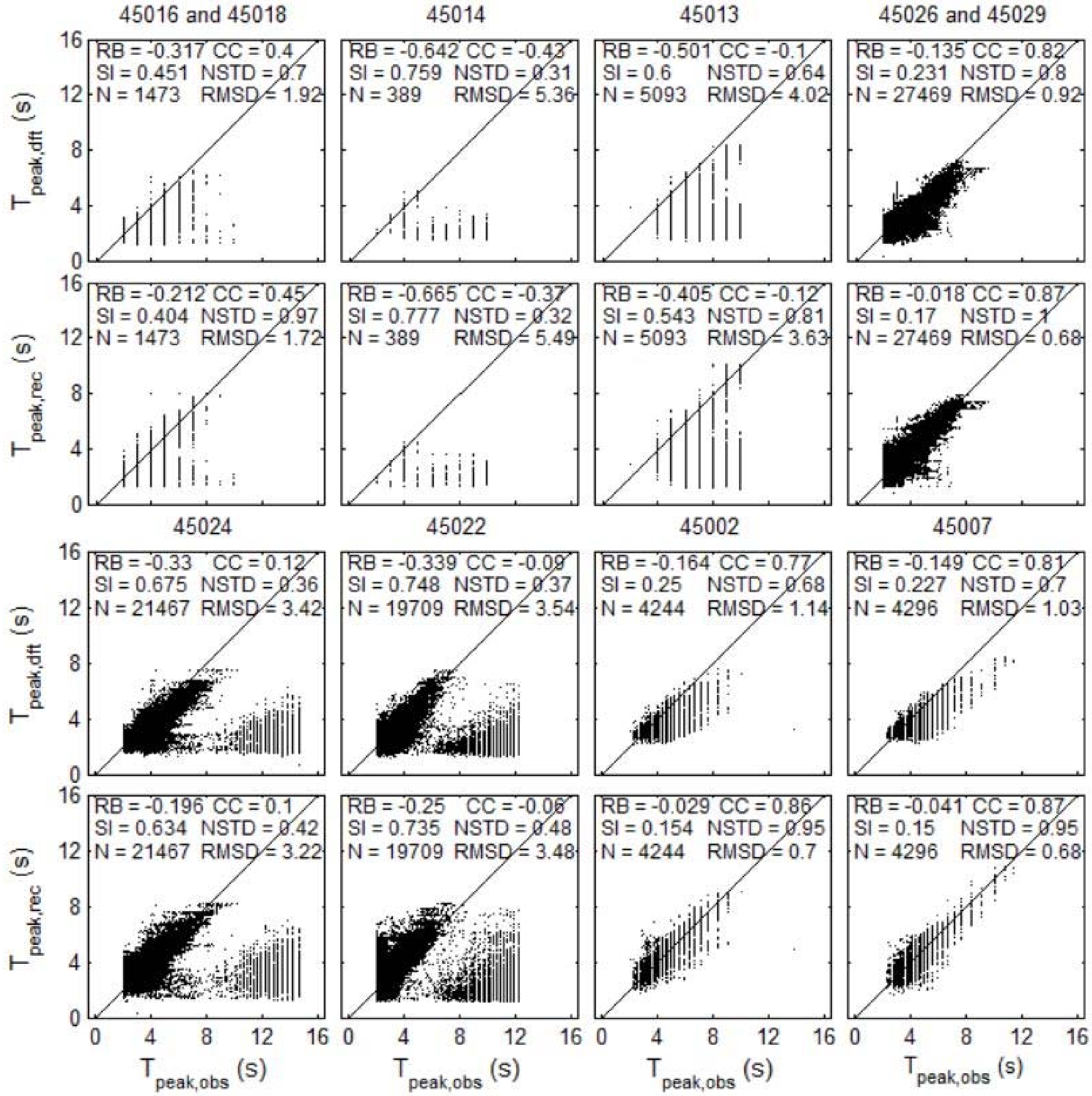

Fig. 6b. Same as Fig. 6a except for that SWH (H_{sig}) is replaced by PWP (T_{peak}).

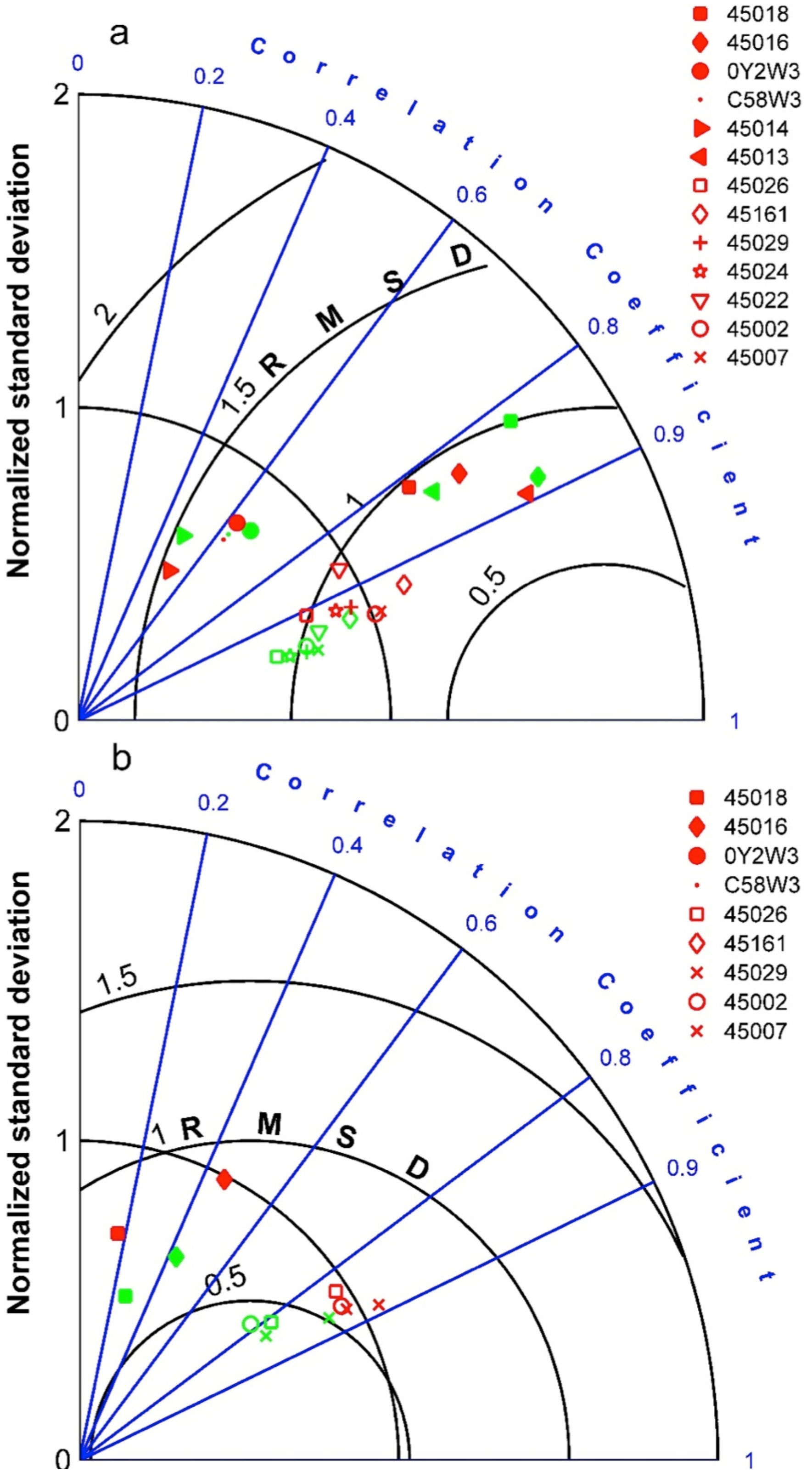

Fig. 7. Taylor diagrams summarizing the CC, NSTD, and RMSD values for un-SWAN model estimations with default (green) and recalibrated settings (red) compared with NDBC *in-situ* observations for (a) SWH and (b) PWP.

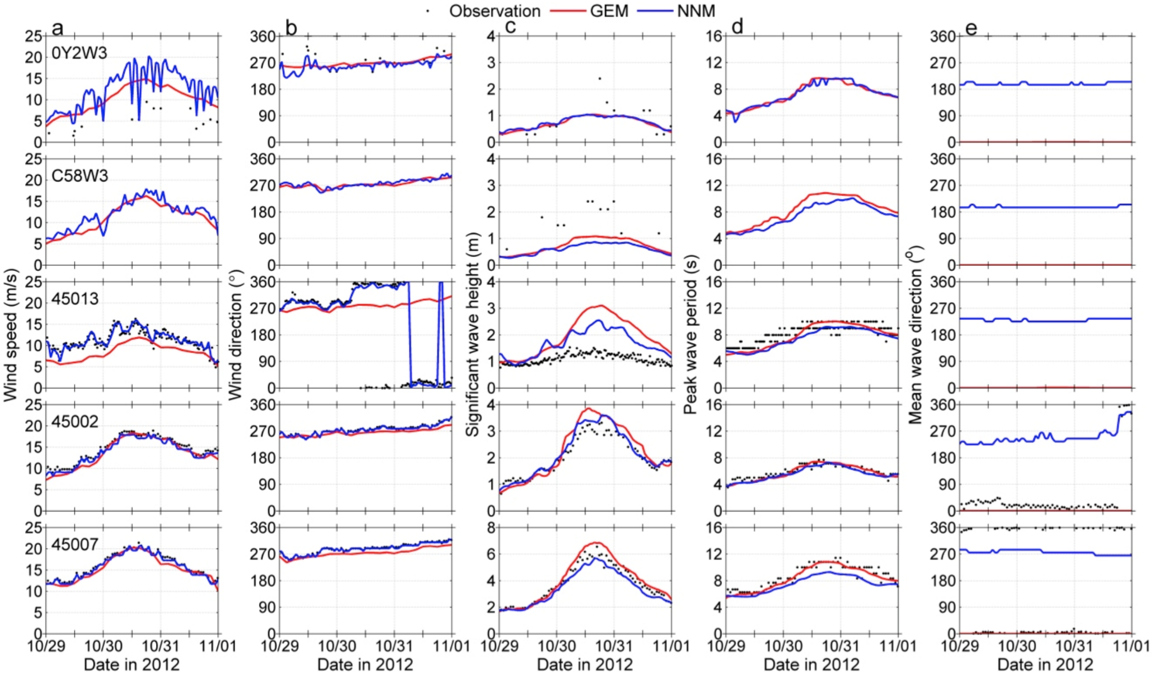

Fig. 8 Time series of (a) wind speed and (b) wind direction taken from the GEM and NNM fields, and (c) SWH, (d) PWP, and (e) MWD determined through the un-SWAN models driven by these two fields compared with observations taken at various NDBC buoys during Superstorm Sandy (2012). Note: Cartesian conventions are adopted here for wind direction.

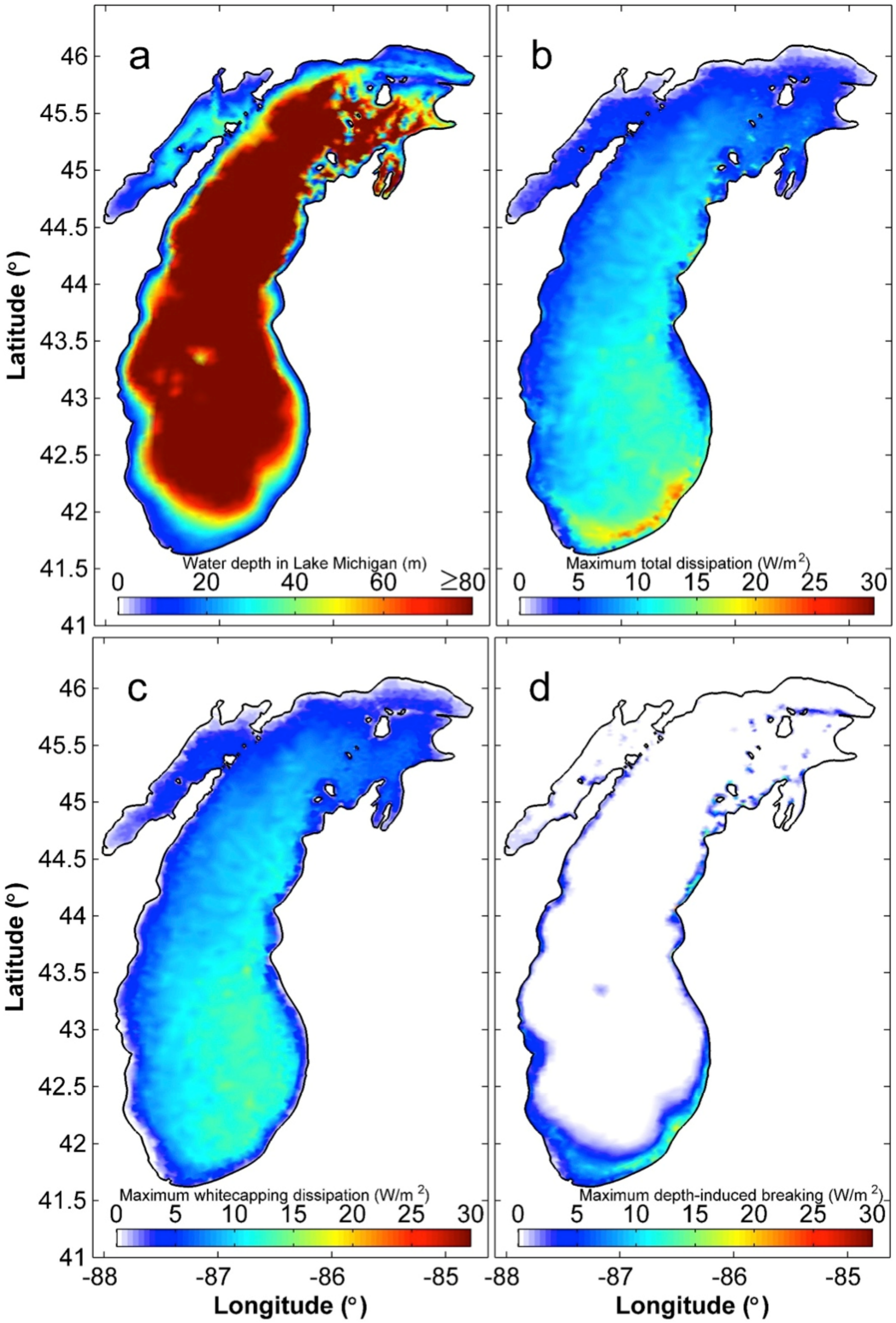

Fig. 9. Spatial distributions of (a) water depth and maximum (b) total energy dissipation, (c) whitecapping dissipation, and (d) depth-induced wave breaking during Superstorm Sandy (2012).

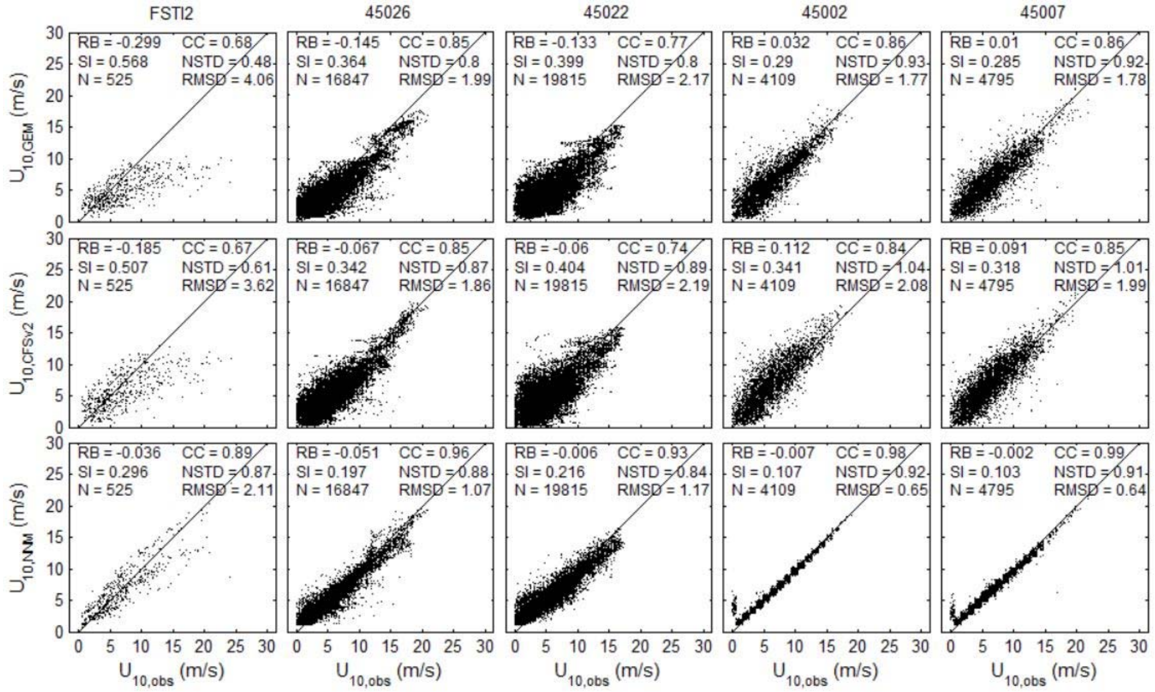

Fig. 10a. Scatterplots of wind speeds from the GEM ($U_{10,GEM}$; top), CFSv2 ($U_{10,CFSv2}$; middle), and NNM ($U_{10,NNM}$; bottom) wind fields versus observed wind speed values ($U_{10,obs}$) taken at various NDBC buoys. Note: because no wind data are available at station 45018, the observed winds from the adjacent FSTI2 station are used.

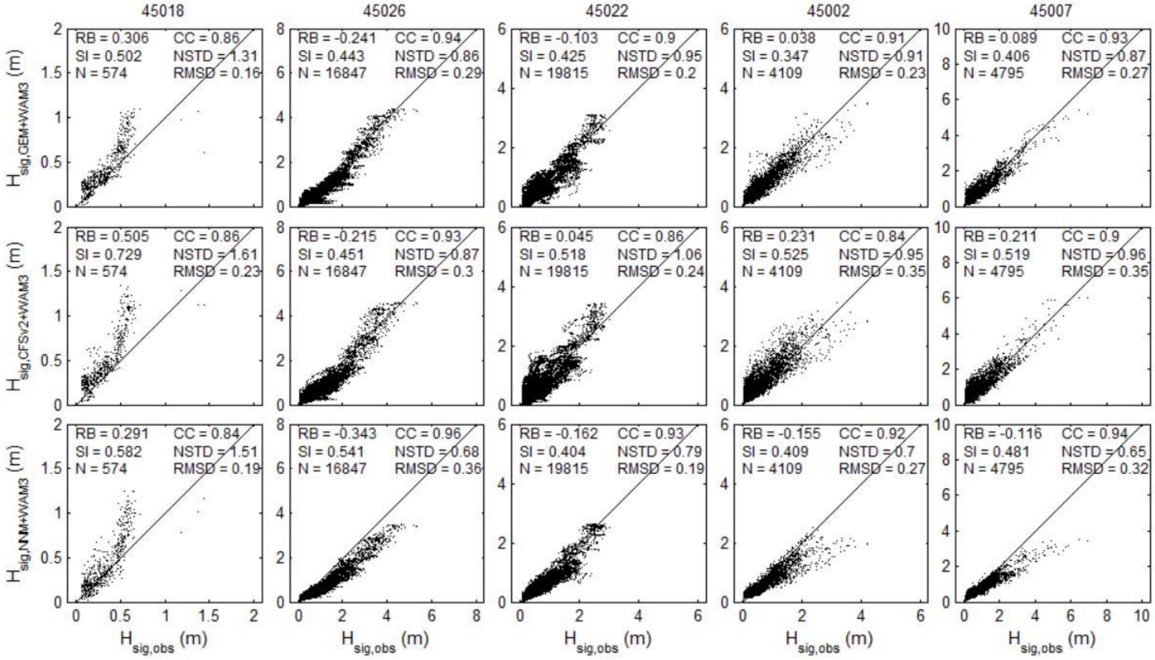

Fig. 10b. Scatterplots of modeled SWH values from the un-SWAN model with default deep-water wave growth formulation (Komen et al., 1984) driven by the GEM ($H_{sig,GEM+WAM3}$; top panel), CFSv2 ($H_{sig,CFSv2+WAM3}$; middle panel), and NNM wind fields ($H_{sig,NNM+WAM3}$; bottom panel) versus observations of SWH ($H_{sig,obs}$) from various NDBC buoys.

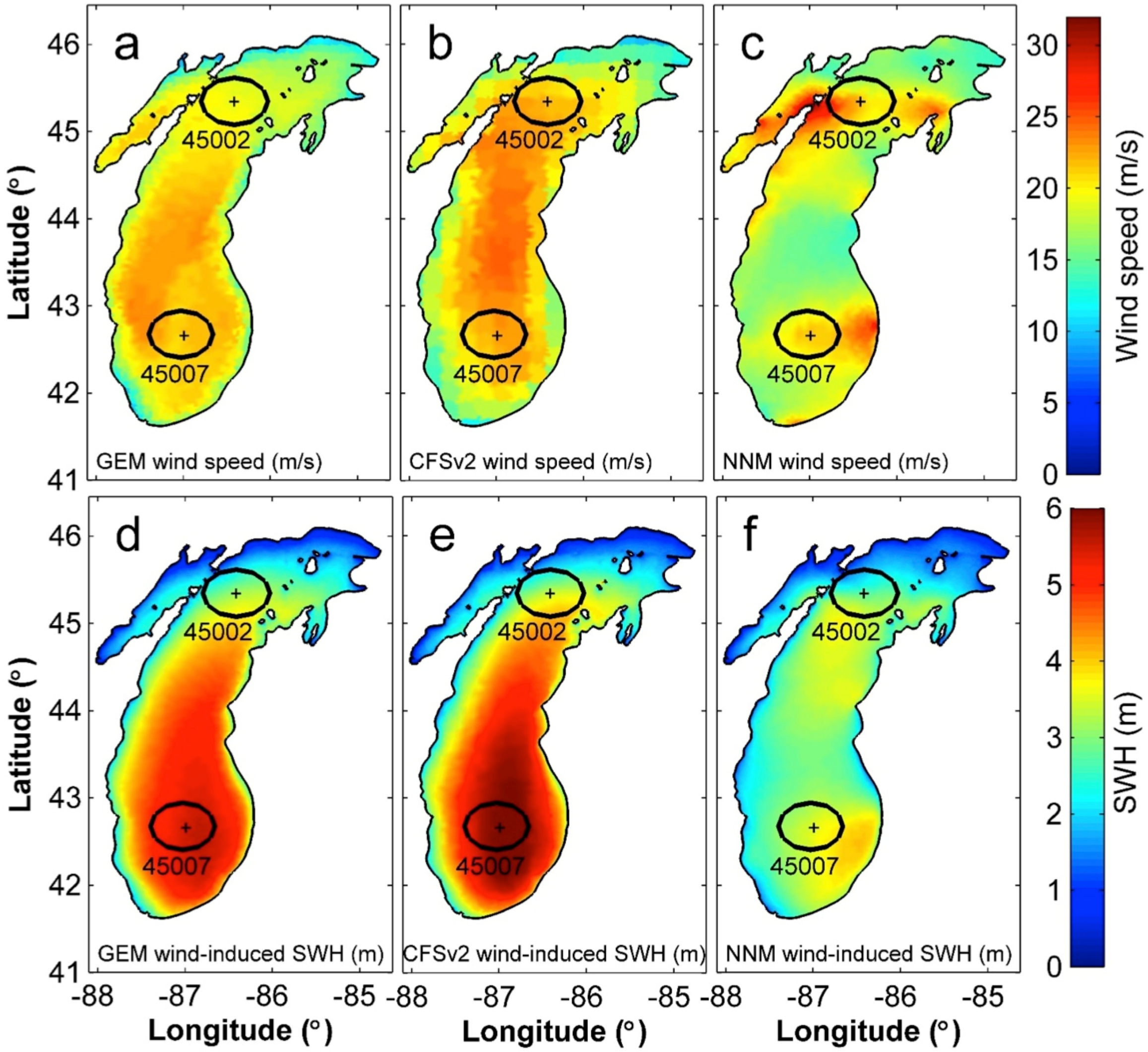

Fig. 11. Spatial distributions of the maximum wind speeds determined with the (a) GEM, (b) CFSv2, and (c) NNM wind fields, and corresponding SWHs (d–f), during a 2011 clipper storm. Note that black crosses denote the locations of mid-lake buoys 45002 and 45007, and that black circles cover the adjacent interpolation smoothing distance (30 km) for the NNM.

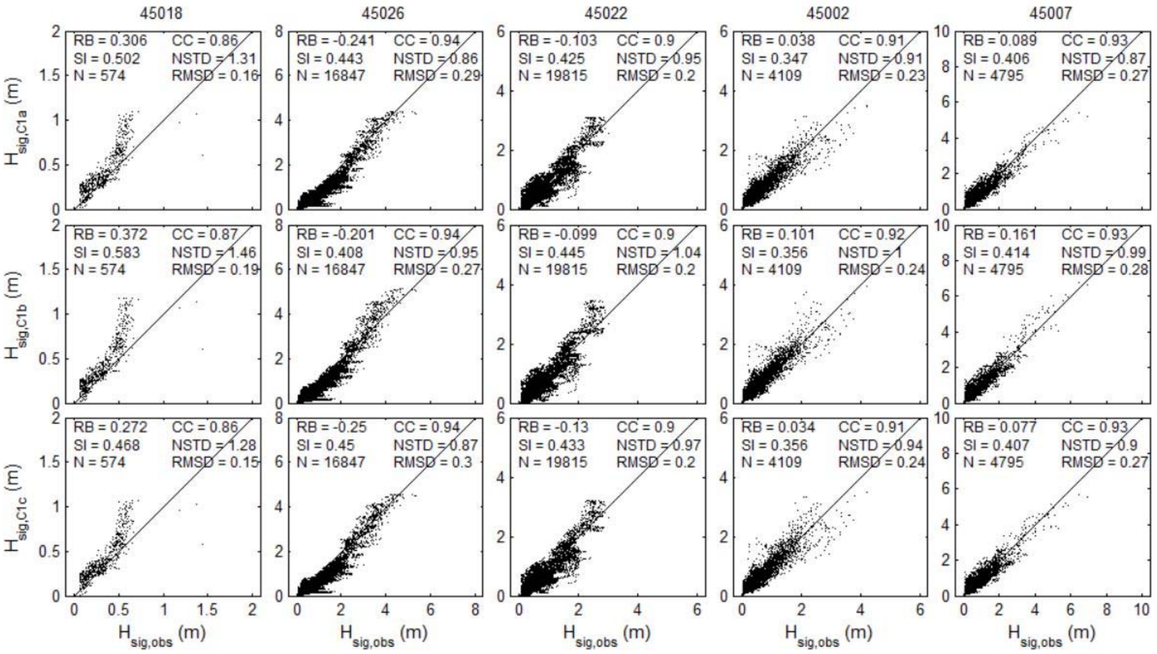

Fig. 12a. Scatterplots of modeled SWHs from the un-SWAN model with various wind input and whitecapping settings versus observed SWH values ($H_{sig,obs}$) taken at various NDBC buoys. The top, middle, and bottom panels are $H_{sig,C1a}$, $H_{sig,C1b}$, and $H_{sig,C1c}$ for the Case 1a (Komen et al., 1984), Case 1b (recalibrated Rogers et al., 2003), and Case 1c (van der Westhuysen et al., 2007) formulations for deep-water wave physics, respectively.

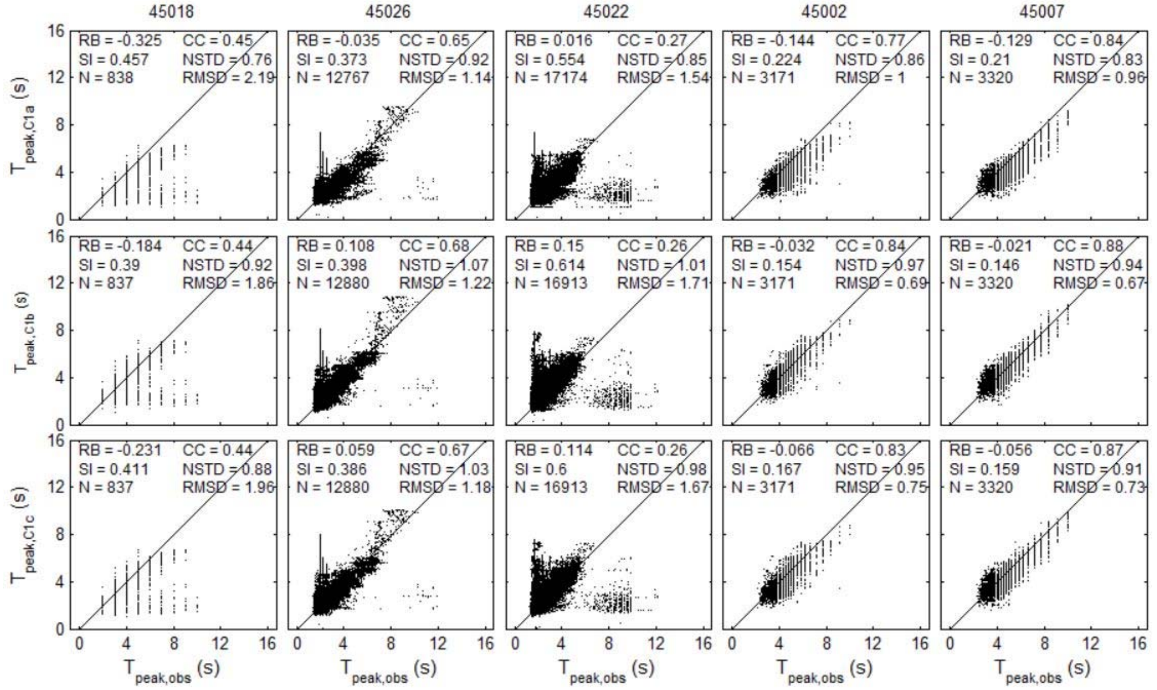

Fig. 12b. Same as Fig. 12a except for that SWH (H_{sig}) is replaced with PWP (T_{peak}).

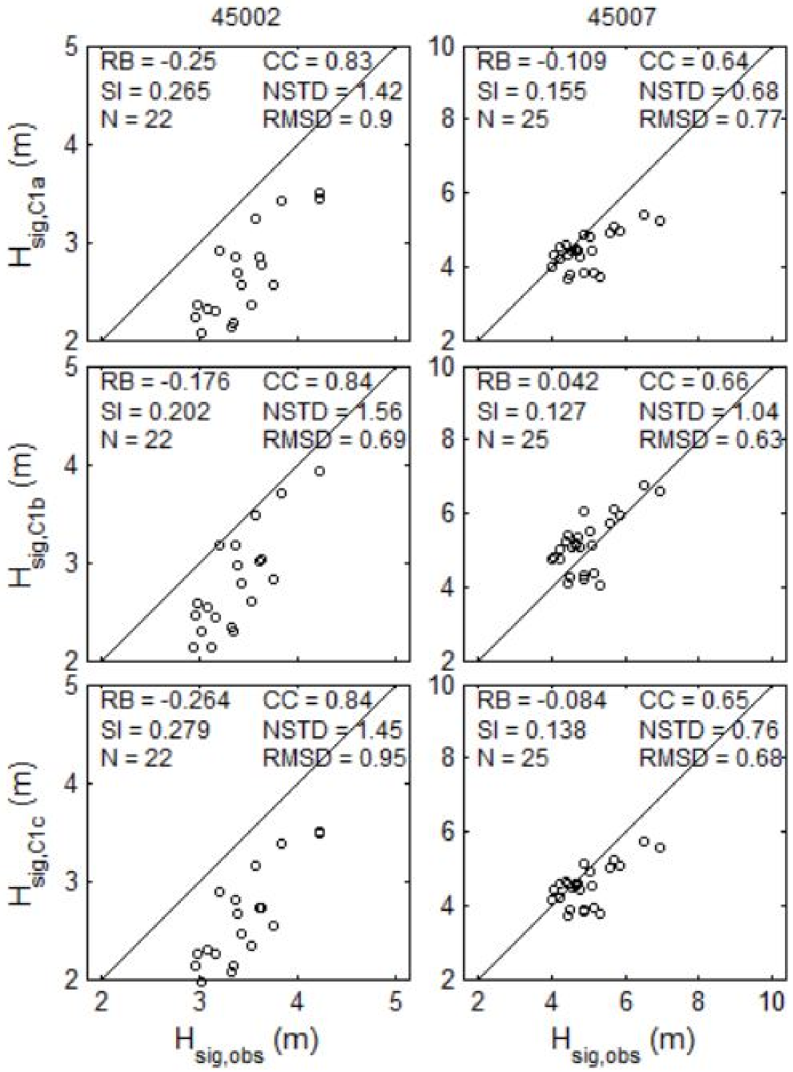

Fig. 12c. Same as Fig. 12a except for that the SWH values (H_{sig}) are replaced with extreme values (above the 99.5th percentile) from the mid-lake buoys 45002 and 45007.

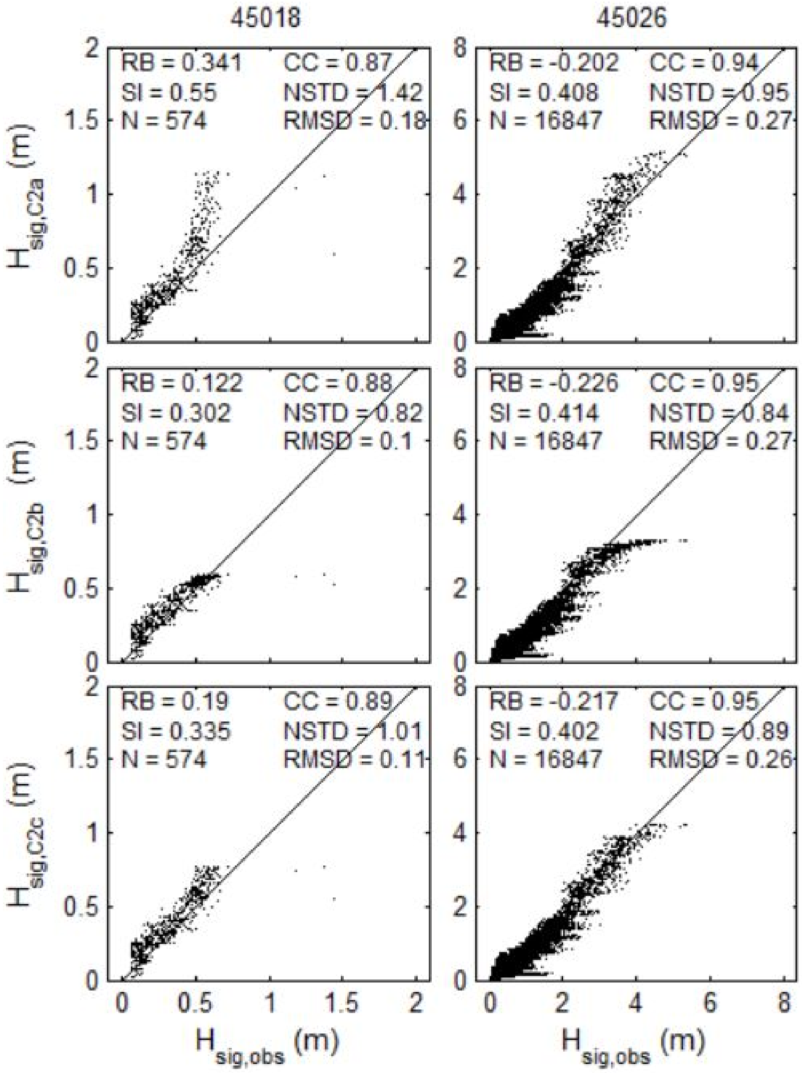

Fig. 13. Scatterplots of modeled SWHs from the un-SWAN model with various depth-induced breaking settings versus observed SWH values ($H_{sig,obs}$) taken at the shallow-water buoys 45018 and 45022. The top, middle, and bottom panels are $H_{sig,C2a}$, $H_{sig,C2b}$, and $H_{sig,C2c}$ from Case 2a (the BJ78 model with default $\gamma_{BJ} = 0.3$), Case 2b (the BJ78 model with a decreased $\gamma_{BJ} = 0.3$), and Case 2c (the TG83 model with default $\gamma_{TG} = 0.42$) for estimating shallow-water wave physics, respectively.

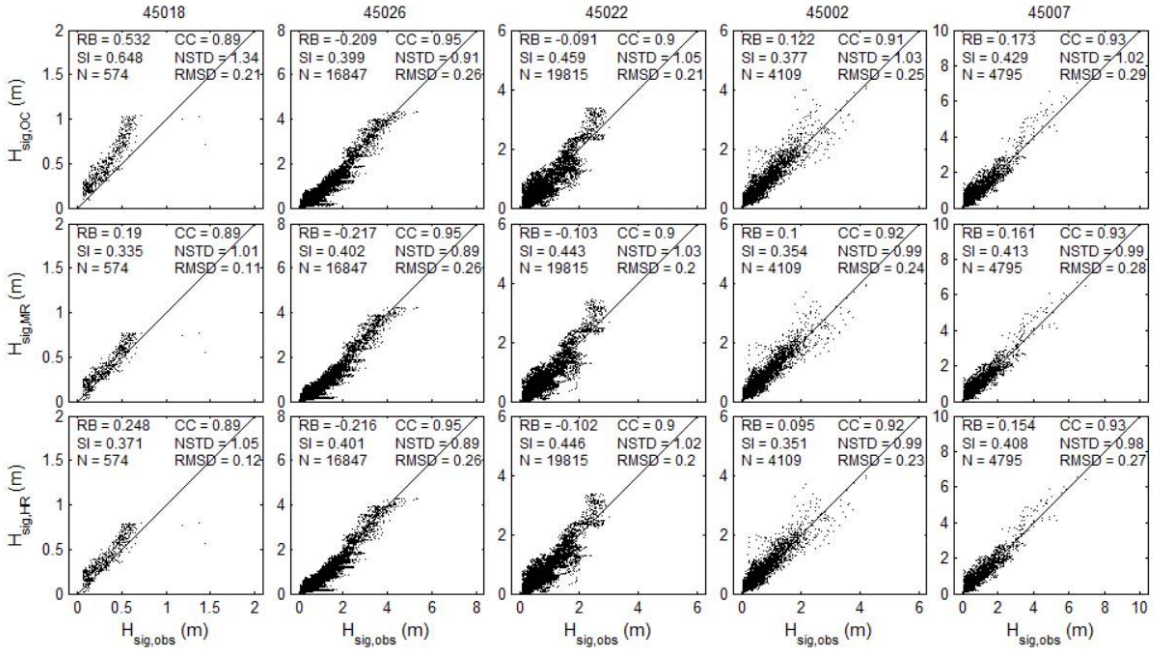

Fig. 14. Scatterplots of modeled SWHs ($H_{sig,OC}$, $H_{sig,MR}$, and $H_{sig,HR}$) from the wave model using orthogonal curvilinear (top panel), medium- (middle panel), and high-resolution (bottom panel) meshes, respectively, versus observed SWH values ($H_{sig,obs}$) taken at various NDBC buoys.

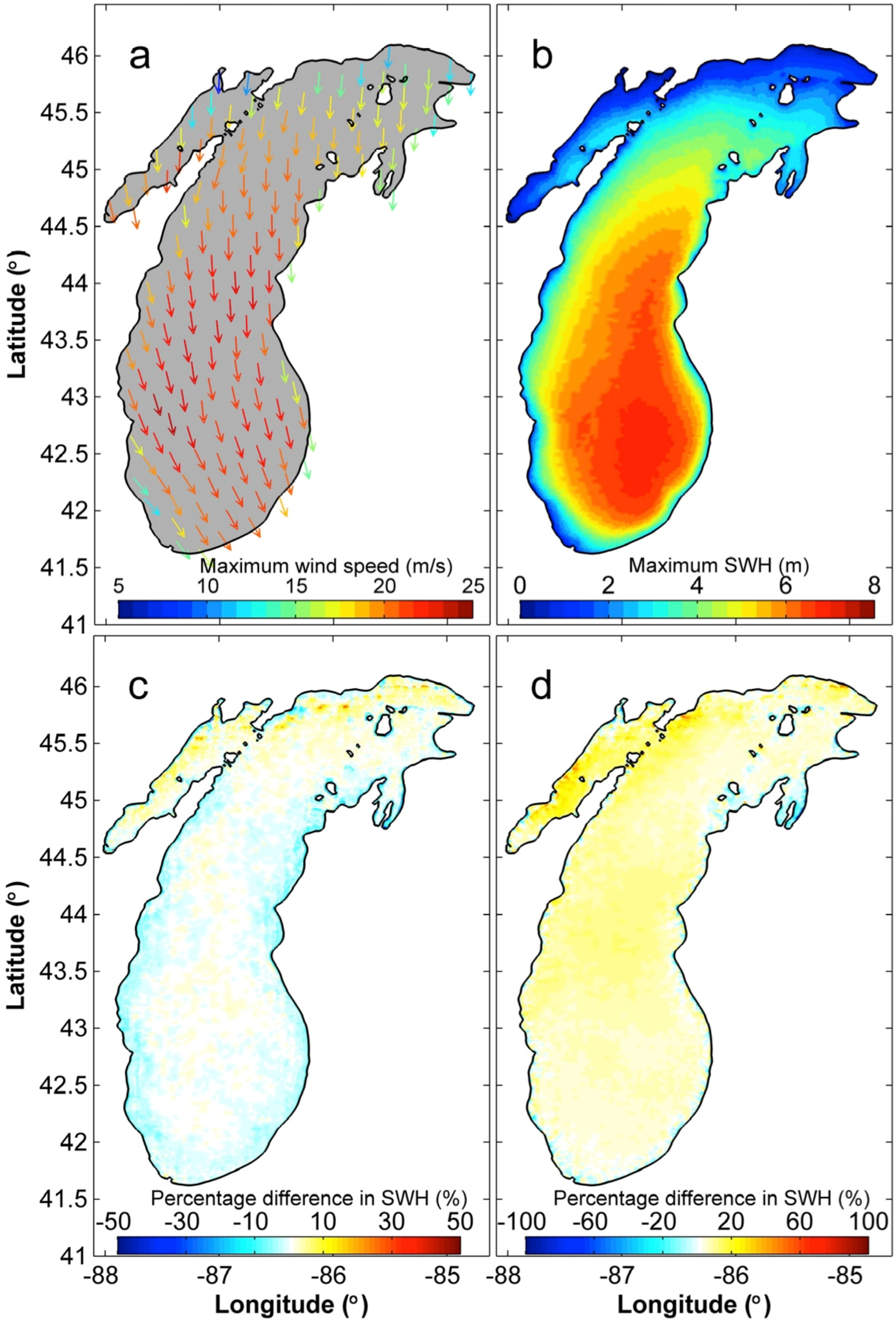

Fig. 15. Spatial distributions of the maximum (a) wind speed and (b) SWH, and the differences in percentages of SWHs from (c) the MR un-SWAN results minus the HR un-SWAN results, and (d) the OC SWAN results minus the HR un-SWAN results, during a clipper storm in 2011. Note the difference in scale between panels (c) and (d).

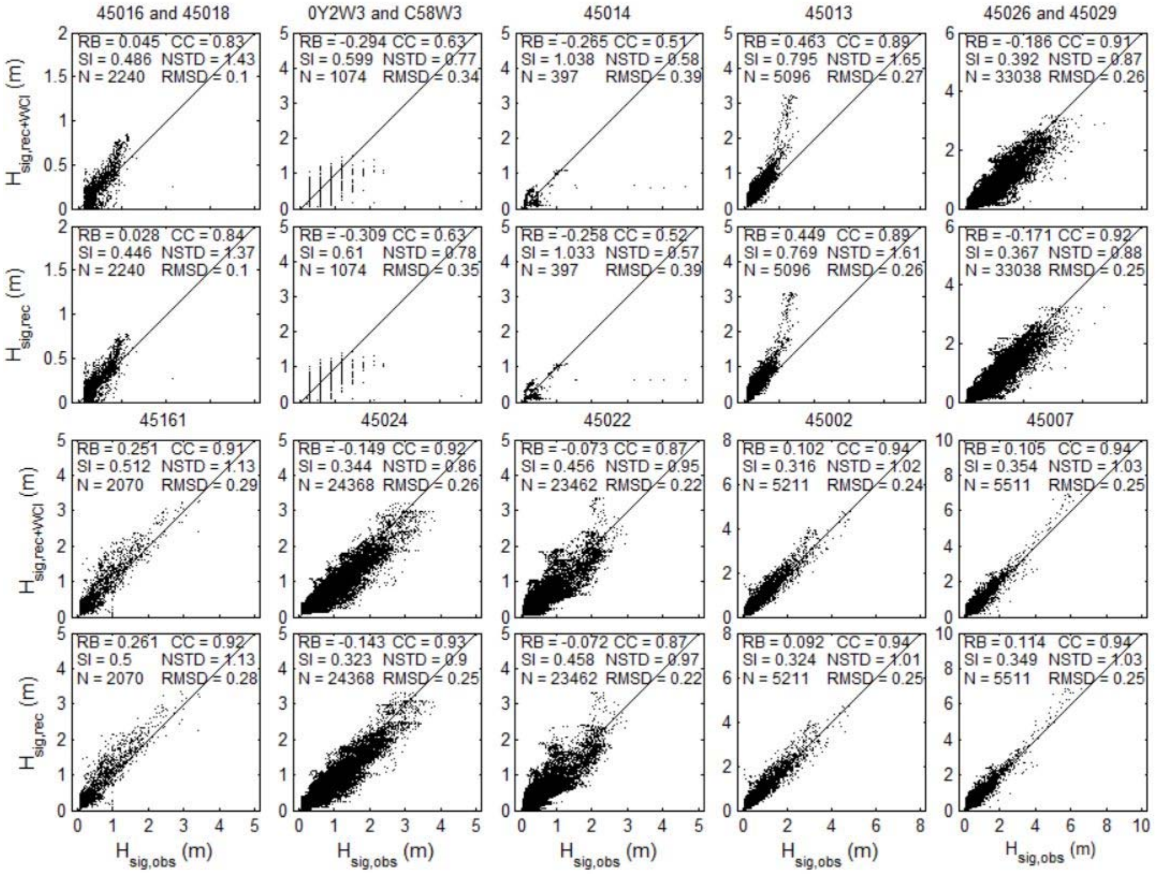

Fig. 16a. Scatterplots of modeled SWHs from the recalibrated wave-only ($H_{sig,rec}$; first and third rows) and wave−current interactions (WCI) coupled models ($H_{sig,rec+WCI}$; second and fourth rows) versus observed SWH values ($H_{sig,obs}$) taken at various NDBC buoys in 2012.

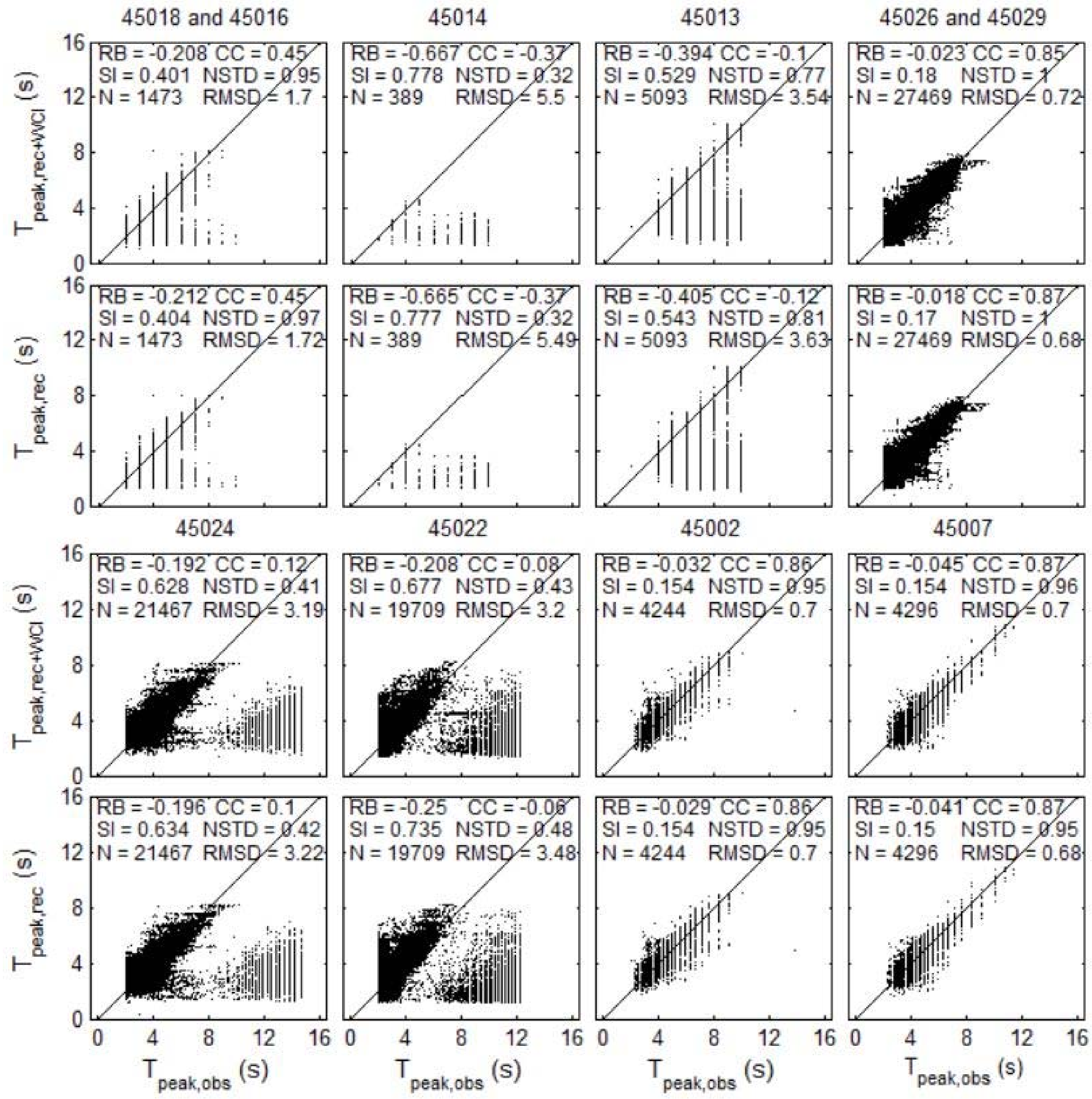

Fig. 16b. Scatterplots of modeled PWPs from the recalibrated wave-only ($T_{peak,rec}$; first and third rows) and wave–current interactions (WCI) coupled models ($T_{peak,rec+WCI}$; second and fourth rows) versus observed PWP values ($T_{peak,obs}$) taken at various NDBC buoys in 2012.

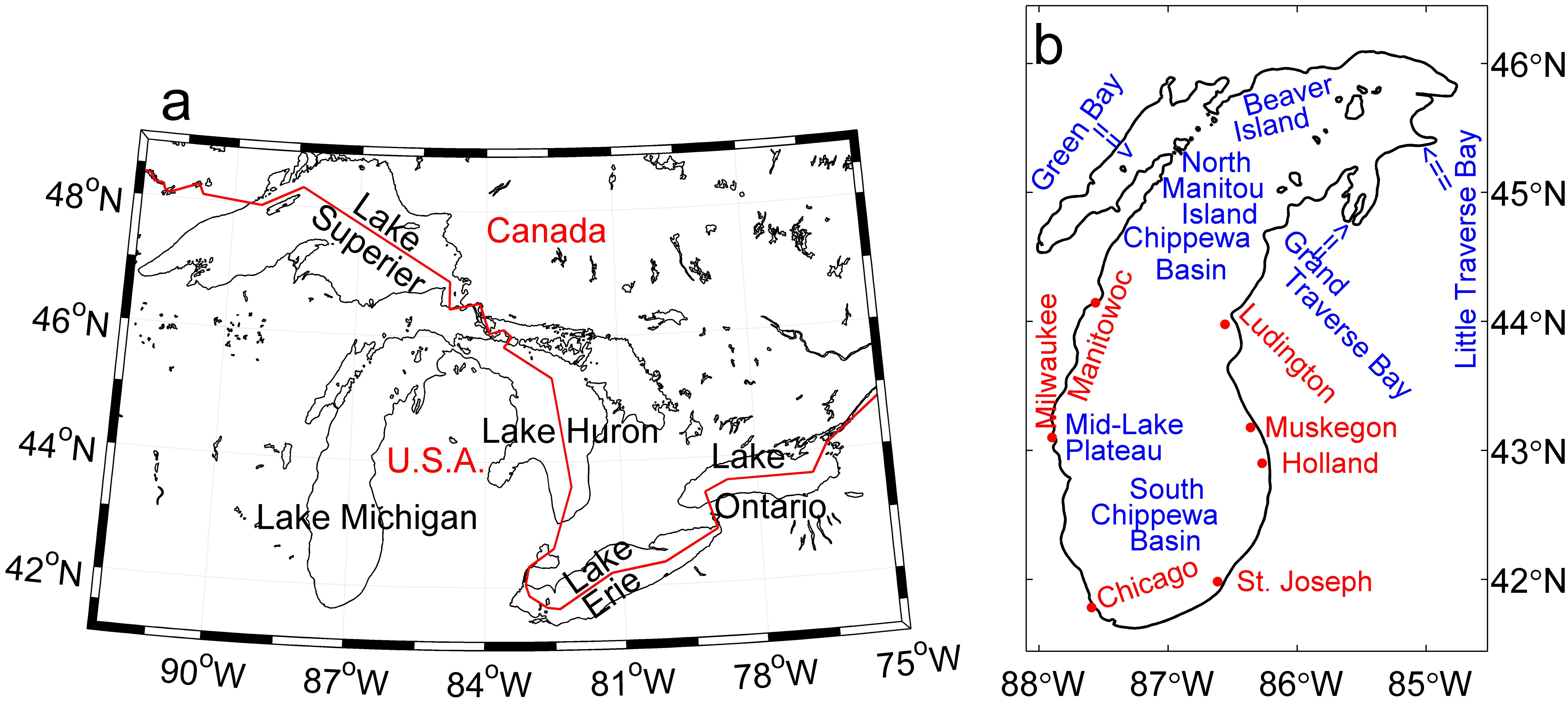
a
48°N
46°N
44°N
42°N
90°W
87°W
84°W
81°W
78°W
75°W
Lake Superier
Canada
Lake Huron
U.S.A.
Lake Ontario
Lake Michigan
Lake Erie
b
Green Bay
Beaver Island
North Manitou Island
Chippewa Basin
Grand Traverse Bay
Little Traverse Bay
Milwaukee
Manitowoc
Ludington
Mid-Lake Plateau
Muskegon
Holland
South Chippewa Basin
Chicago
St. Joseph
46°N
45°N
44°N
43°N
42°N
88°W
87°W
86°W
85°W

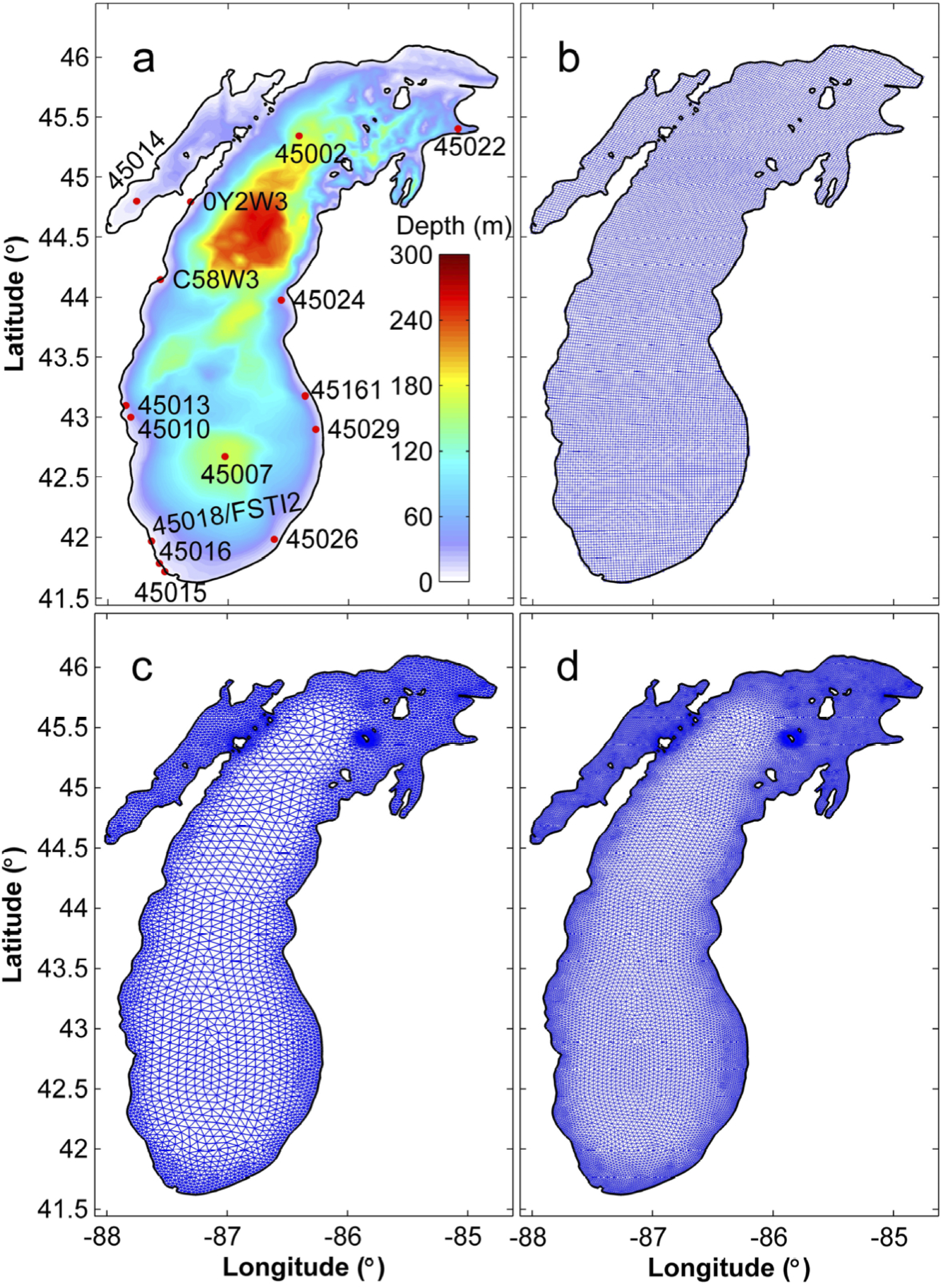
a
b
c
d
45014
45002
45022
0Y2W3
Depth (m)
300
240
180
120
60
0
C58W3
45024
45161
45013
45010
45029
45007
45018/FSTI2
45016
45026
45015
Latitude (°)
46
45.5
45
44.5
44
43.5
43
42.5
42
41.5
Longitude (°)
-88
-87
-86
-85

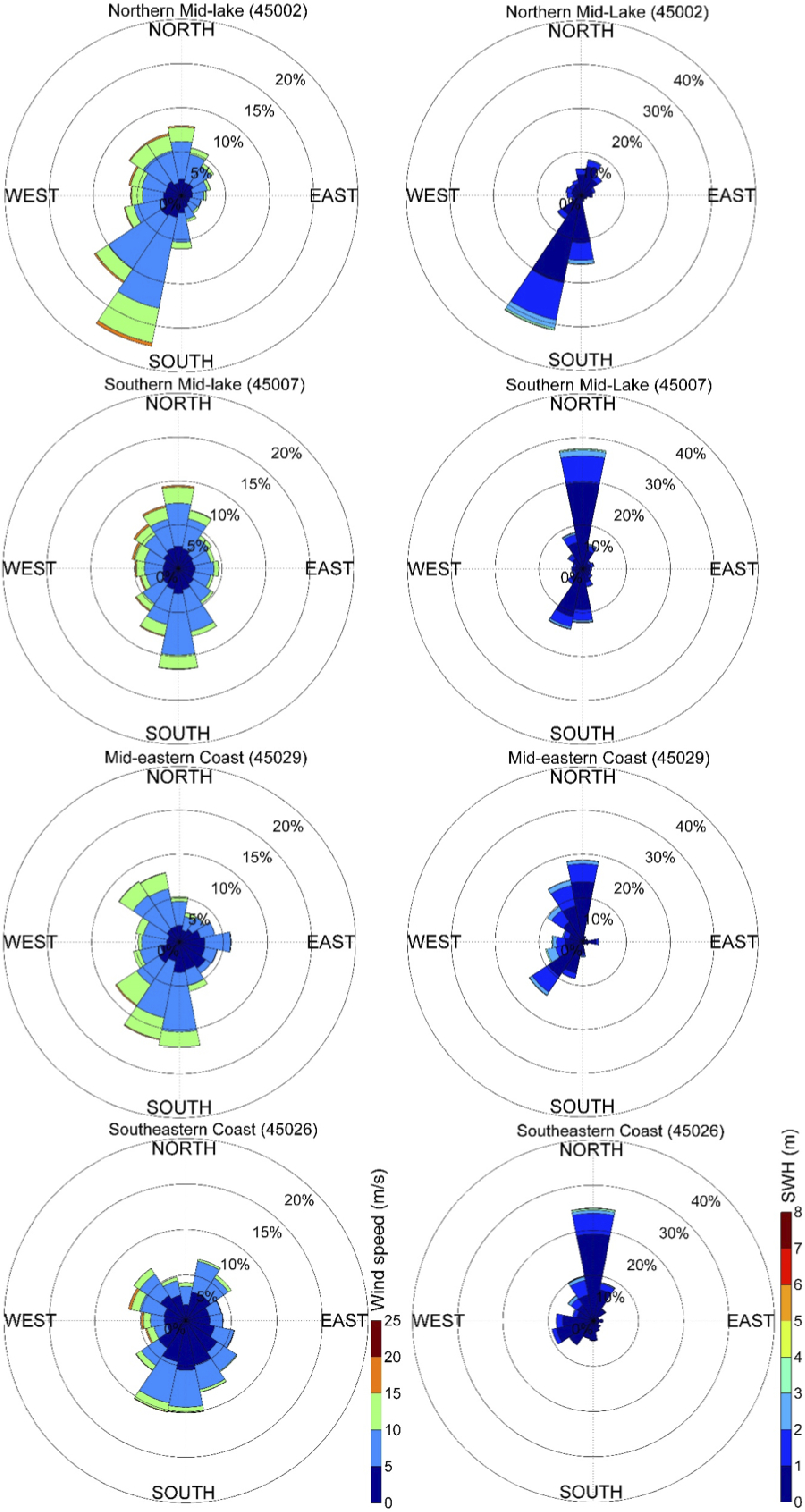
Northern Mid-lake (45002)
Northern Mid-Lake (45002)
Southern Mid-lake (45007)
Southern Mid-Lake (45007)
Mid-eastern Coast (45029)
Mid-eastern Coast (45029)
Southeastern Coast (45026)
Southeastern Coast (45026)
NORTH
SOUTH
EAST
WEST
0%
5%
10%
15%
20%
30%
40%
Wind speed (m/s)
0
5
10
15
20
25
SWH (m)
0
1
2
3
4
5
6
7
8

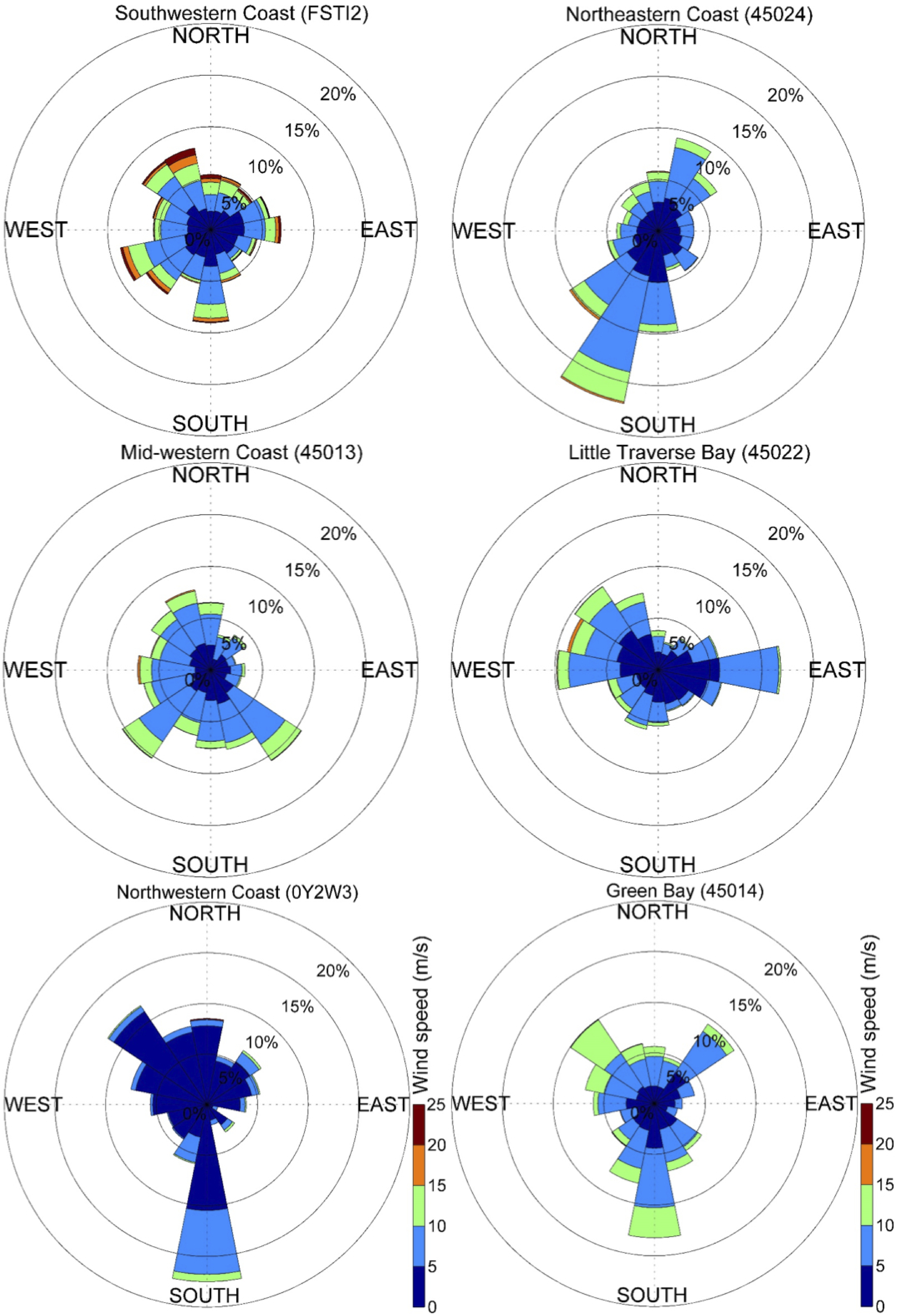
Southwestern Coast (FSTI2)
Northeastern Coast (45024)
Mid-western Coast (45013)
Little Traverse Bay (45022)
Northwestern Coast (0Y2W3)
Green Bay (45014)
NORTH
SOUTH
EAST
WEST
0%
5%
10%
15%
20%
Wind speed (m/s)
0
5
10
15
20
25


a
b
Northern Mid-lake (45002)
Southern Mid-Lake (45007)
Green Bay (45014)
Little Traverse Bay (45022)
Western Coast (45013 and 0Y2W3)
Eastern Coast (45024, 45026) (45029, and 45161)
SWH (m)
Wind speed (m/s)
1.5
1
0.5
0
10
8
6
4
2
0
April
May
June
July
August
September
October
November

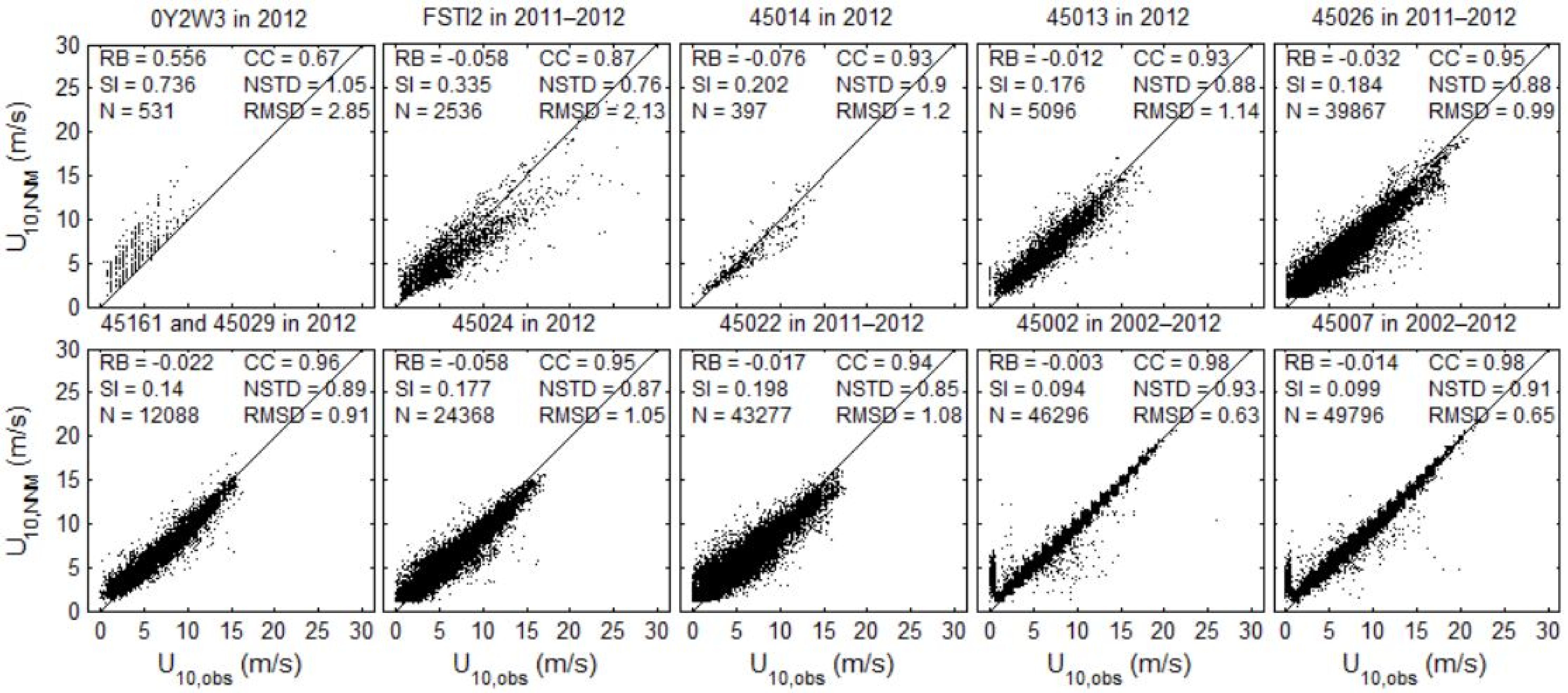
0Y2W3 in 2012
RB = 0.556 CC = 0.67
SI = 0.736 NSTD = 1.05
N = 531 RMSD = 2.85
FSTI2 in 2011–2012
RB = -0.058 CC = 0.87
SI = 0.335 NSTD = 0.76
N = 2536 RMSD = 2.13
45014 in 2012
RB = -0.076 CC = 0.93
SI = 0.202 NSTD = 0.9
N = 397 RMSD = 1.2
45013 in 2012
RB = -0.012 CC = 0.93
SI = 0.176 NSTD = 0.88
N = 5096 RMSD = 1.14
45026 in 2011–2012
RB = -0.032 CC = 0.95
SI = 0.184 NSTD = 0.88
N = 39867 RMSD = 0.99
45161 and 45029 in 2012
RB = -0.022 CC = 0.96
SI = 0.14 NSTD = 0.89
N = 12088 RMSD = 0.91
45024 in 2012
RB = -0.058 CC = 0.95
SI = 0.177 NSTD = 0.87
N = 24368 RMSD = 1.05
45022 in 2011–2012
RB = -0.017 CC = 0.94
SI = 0.198 NSTD = 0.85
N = 43277 RMSD = 1.08
45002 in 2002–2012
RB = -0.003 CC = 0.98
SI = 0.094 NSTD = 0.93
N = 46296 RMSD = 0.63
45007 in 2002–2012
RB = -0.014 CC = 0.98
SI = 0.099 NSTD = 0.91
N = 49796 RMSD = 0.65
$U_{10,NNM}$ (m/s)
$U_{10,obs}$ (m/s)
0
5
10
15
20
25
30

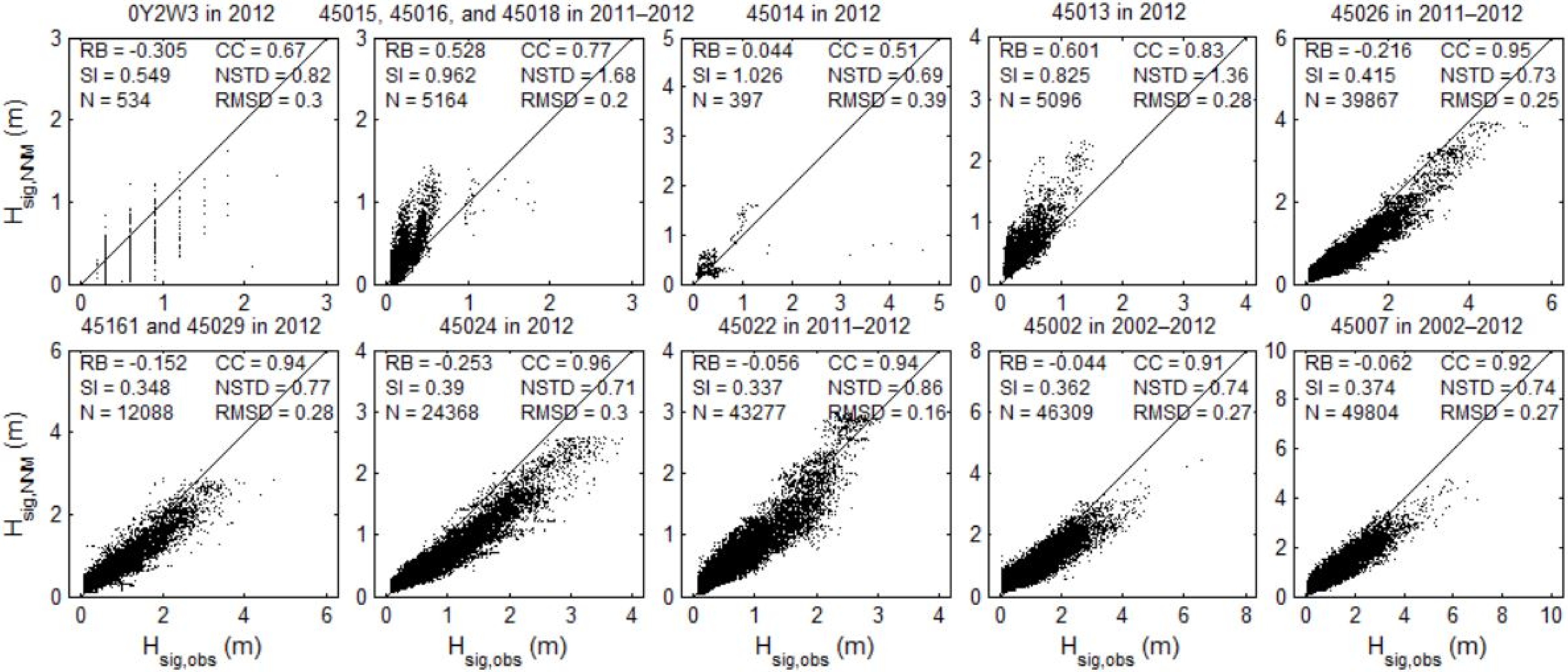
0Y2W3 in 2012
RB = -0.305 CC = 0.67
SI = 0.549 NSTD = 0.82
N = 534 RMSD = 0.3
45015, 45016, and 45018 in 2011–2012
RB = 0.528 CC = 0.77
SI = 0.962 NSTD = 1.68
N = 5164 RMSD = 0.2
45014 in 2012
RB = 0.044 CC = 0.51
SI = 1.026 NSTD = 0.69
N = 397 RMSD = 0.39
45013 in 2012
RB = 0.601 CC = 0.83
SI = 0.825 NSTD = 1.36
N = 5096 RMSD = 0.28
45026 in 2011–2012
RB = -0.216 CC = 0.95
SI = 0.415 NSTD = 0.73
N = 39867 RMSD = 0.25
45161 and 45029 in 2012
RB = -0.152 CC = 0.94
SI = 0.348 NSTD = 0.77
N = 12088 RMSD = 0.28
45024 in 2012
RB = -0.253 CC = 0.96
SI = 0.39 NSTD = 0.71
N = 24368 RMSD = 0.3
45022 in 2011–2012
RB = -0.056 CC = 0.94
SI = 0.337 NSTD = 0.86
N = 43277 RMSD = 0.16
45002 in 2002–2012
RB = -0.044 CC = 0.91
SI = 0.362 NSTD = 0.74
N = 46309 RMSD = 0.27
45007 in 2002–2012
RB = -0.062 CC = 0.92
SI = 0.374 NSTD = 0.74
N = 49804 RMSD = 0.27
H_sig,NNM (m)
H_sig,obs (m)

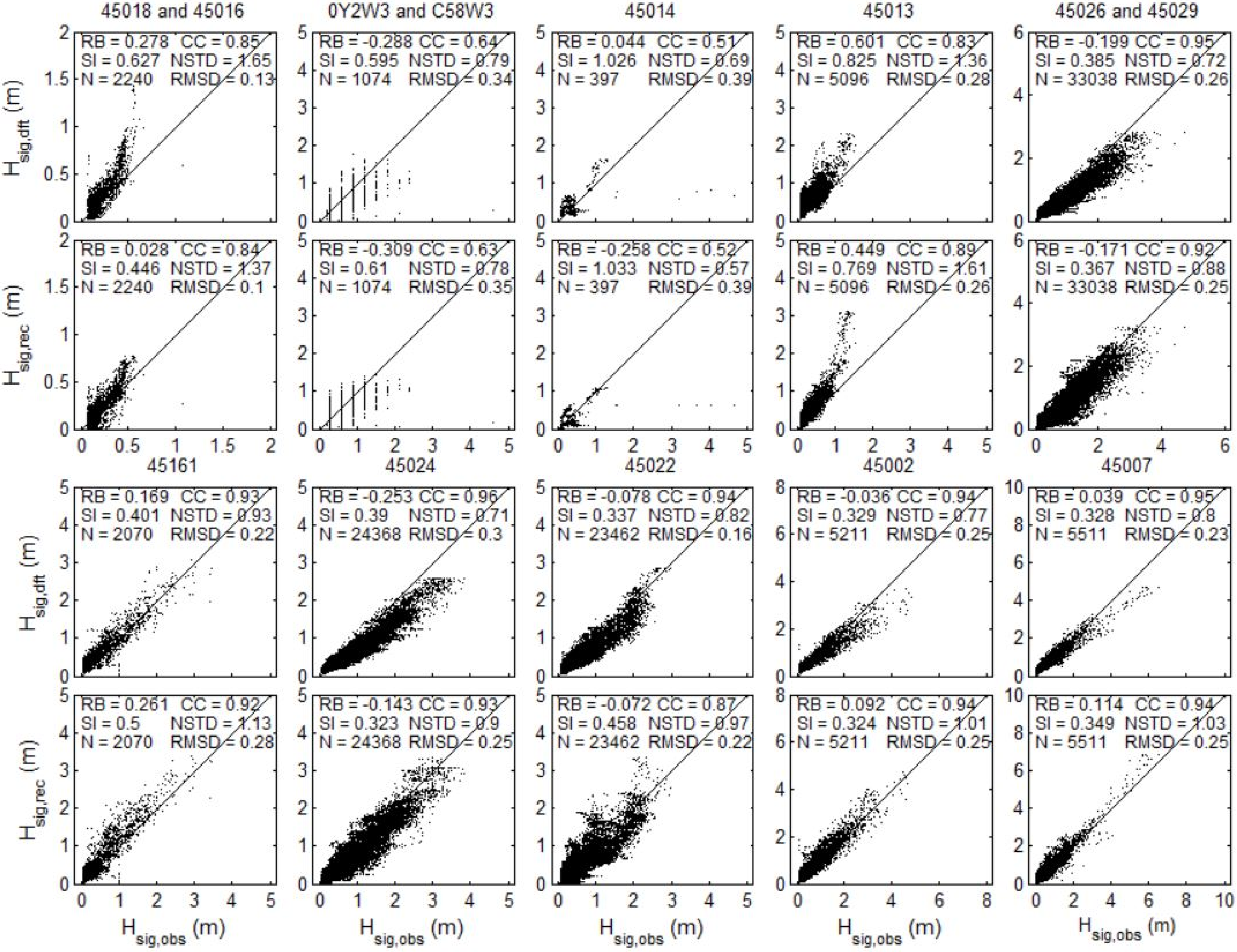
45018 and 45016
RB = 0.278 CC = 0.85
SI = 0.627 NSTD = 1.65
N = 2240 RMSD = 0.13
0Y2W3 and C58W3
RB = -0.288 CC = 0.64
SI = 0.595 NSTD = 0.79
N = 1074 RMSD = 0.34
45014
RB = 0.044 CC = 0.51
SI = 1.026 NSTD = 0.69
N = 397 RMSD = 0.39
45013
RB = 0.601 CC = 0.83
SI = 0.825 NSTD = 1.36
N = 5096 RMSD = 0.28
45026 and 45029
RB = -0.199 CC = 0.95
SI = 0.385 NSTD = 0.72
N = 33038 RMSD = 0.26
$H_{sig,dft}$ (m)
RB = 0.028 CC = 0.84
SI = 0.446 NSTD = 1.37
N = 2240 RMSD = 0.1
RB = -0.309 CC = 0.63
SI = 0.61 NSTD = 0.78
N = 1074 RMSD = 0.35
RB = -0.258 CC = 0.52
SI = 1.033 NSTD = 0.57
N = 397 RMSD = 0.39
RB = 0.449 CC = 0.89
SI = 0.769 NSTD = 1.61
N = 5096 RMSD = 0.26
RB = -0.171 CC = 0.92
SI = 0.367 NSTD = 0.88
N = 33038 RMSD = 0.25
$H_{sig,rec}$ (m)
45161
RB = 0.169 CC = 0.93
SI = 0.401 NSTD = 0.93
N = 2070 RMSD = 0.22
45024
RB = -0.253 CC = 0.96
SI = 0.39 NSTD = 0.71
N = 24368 RMSD = 0.3
45022
RB = -0.078 CC = 0.94
SI = 0.337 NSTD = 0.82
N = 23462 RMSD = 0.16
45002
RB = -0.036 CC = 0.94
SI = 0.329 NSTD = 0.77
N = 5211 RMSD = 0.25
45007
RB = 0.039 CC = 0.95
SI = 0.328 NSTD = 0.8
N = 5511 RMSD = 0.23
$H_{sig,dft}$ (m)
RB = 0.261 CC = 0.92
SI = 0.5 NSTD = 1.13
N = 2070 RMSD = 0.28
RB = -0.143 CC = 0.93
SI = 0.323 NSTD = 0.9
N = 24368 RMSD = 0.25
RB = -0.072 CC = 0.87
SI = 0.458 NSTD = 0.97
N = 23462 RMSD = 0.22
RB = 0.092 CC = 0.94
SI = 0.324 NSTD = 1.01
N = 5211 RMSD = 0.25
RB = 0.114 CC = 0.94
SI = 0.349 NSTD = 1.03
N = 5511 RMSD = 0.25
$H_{sig,rec}$ (m)
$H_{sig,obs}$ (m)
$H_{sig,obs}$ (m)
$H_{sig,obs}$ (m)
$H_{sig,obs}$ (m)
$H_{sig,obs}$ (m)

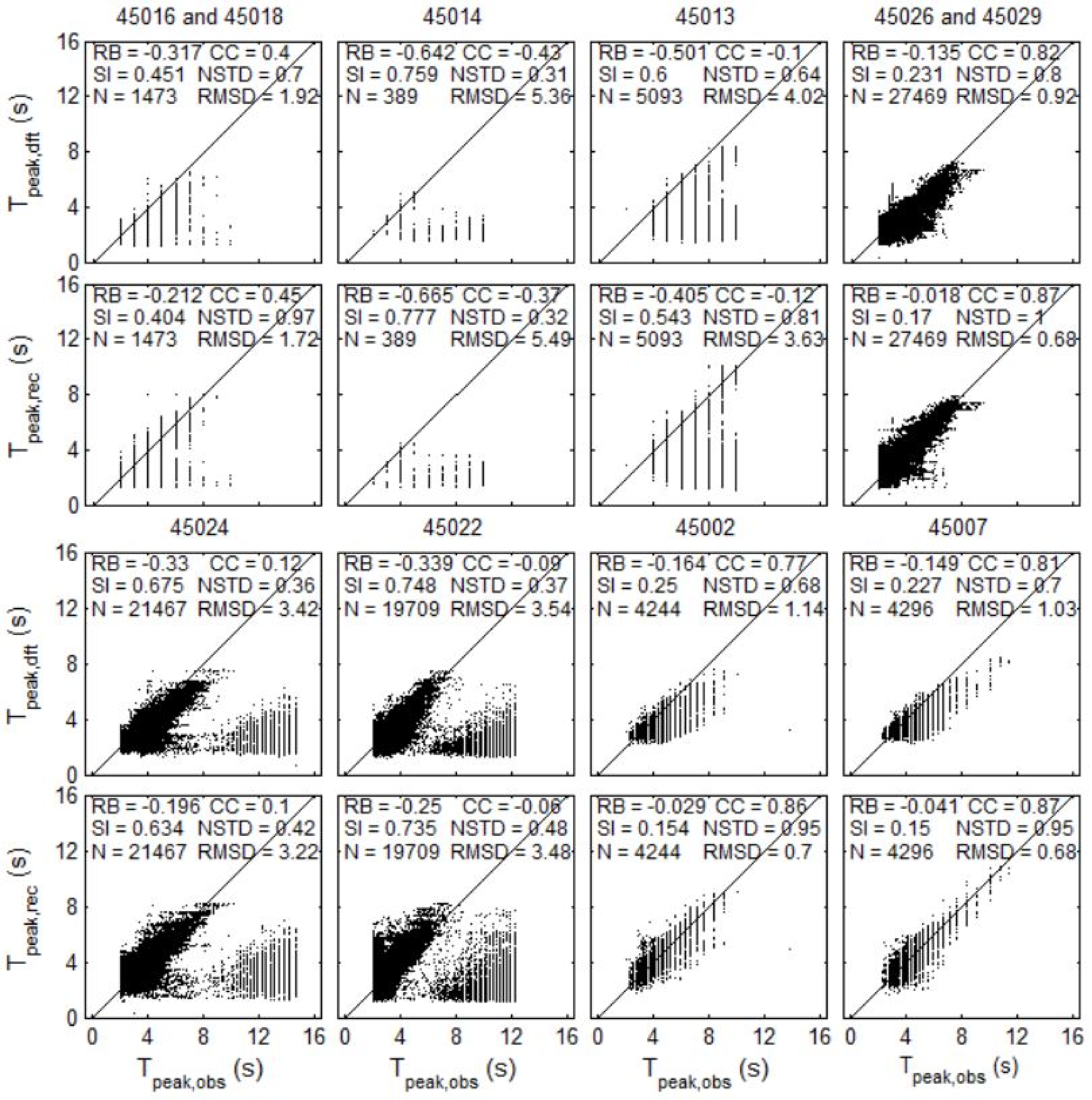
45016 and 45018
45014
45013
45026 and 45029
RB = -0.317 CC = 0.4
SI = 0.451 NSTD = 0.7
N = 1473 RMSD = 1.92
RB = -0.642 CC = -0.43
SI = 0.759 NSTD = 0.31
N = 389 RMSD = 5.36
RB = -0.501 CC = -0.1
SI = 0.6 NSTD = 0.64
N = 5093 RMSD = 4.02
RB = -0.135 CC = 0.82
SI = 0.231 NSTD = 0.8
N = 27469 RMSD = 0.92
RB = -0.212 CC = 0.45
SI = 0.404 NSTD = 0.97
N = 1473 RMSD = 1.72
RB = -0.665 CC = -0.37
SI = 0.777 NSTD = 0.32
N = 389 RMSD = 5.49
RB = -0.405 CC = -0.12
SI = 0.543 NSTD = 0.81
N = 5093 RMSD = 3.63
RB = -0.018 CC = 0.87
SI = 0.17 NSTD = 1
N = 27469 RMSD = 0.68
45024
45022
45002
45007
RB = -0.33 CC = 0.12
SI = 0.675 NSTD = 0.36
N = 21467 RMSD = 3.42
RB = -0.339 CC = -0.09
SI = 0.748 NSTD = 0.37
N = 19709 RMSD = 3.54
RB = -0.164 CC = 0.77
SI = 0.25 NSTD = 0.68
N = 4244 RMSD = 1.14
RB = -0.149 CC = 0.81
SI = 0.227 NSTD = 0.7
N = 4296 RMSD = 1.03
RB = -0.196 CC = 0.1
SI = 0.634 NSTD = 0.42
N = 21467 RMSD = 3.22
RB = -0.25 CC = -0.06
SI = 0.735 NSTD = 0.48
N = 19709 RMSD = 3.48
RB = -0.029 CC = 0.86
SI = 0.154 NSTD = 0.95
N = 4244 RMSD = 0.7
RB = -0.041 CC = 0.87
SI = 0.15 NSTD = 0.95
N = 4296 RMSD = 0.68
$T_{peak,dft}$ (s)
$T_{peak,rec}$ (s)
$T_{peak,obs}$ (s)
0
4
8
12
16

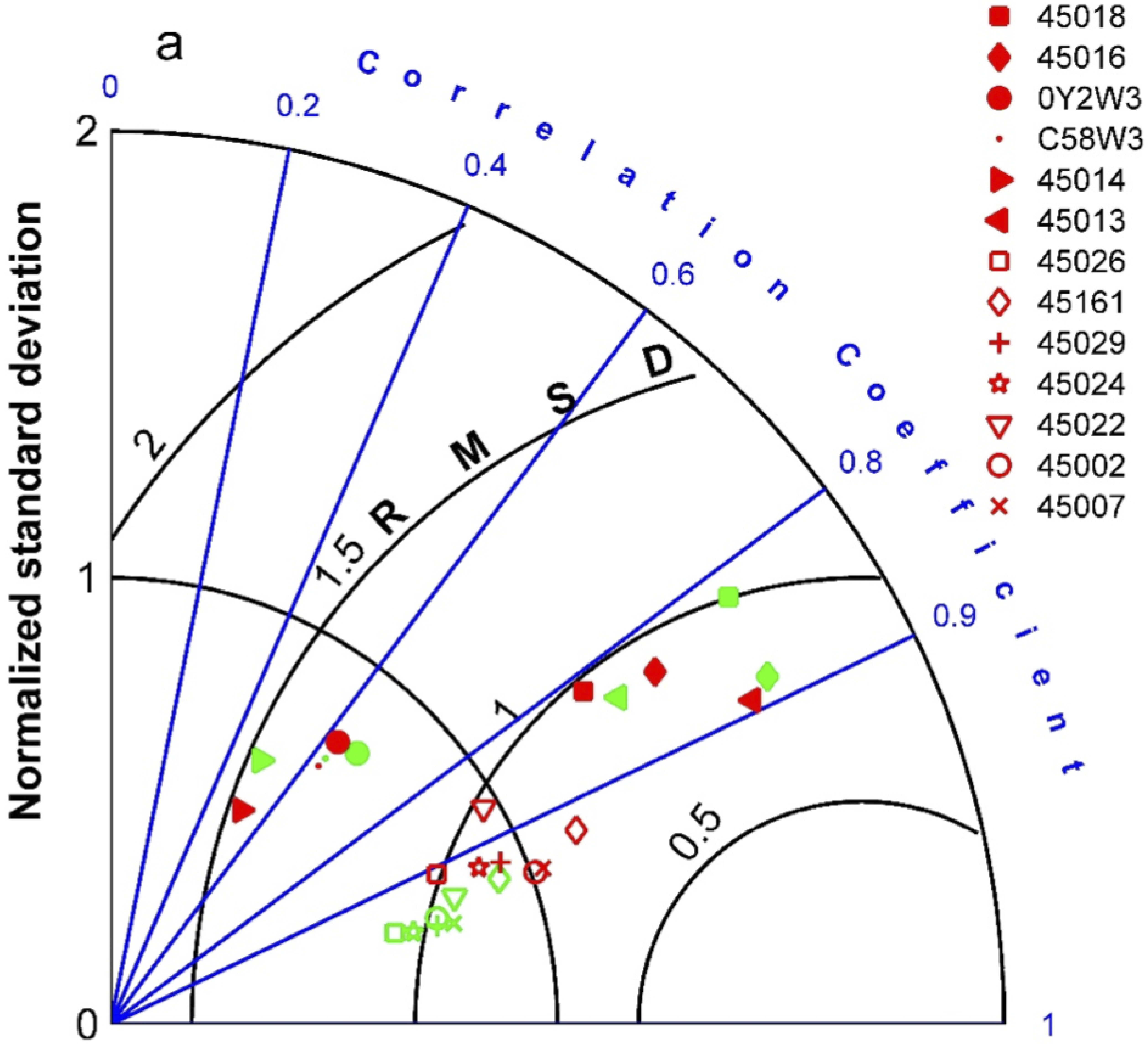
a
Correlation Coefficient
0
0.2
0.4
0.6
0.8
0.9
1
Normalized standard deviation
0
1
2
RMSD
2
1.5
1
0.5
45018
45016
0Y2W3
C58W3
45014
45013
45026
45161
45029
45024
45022
45002
45007

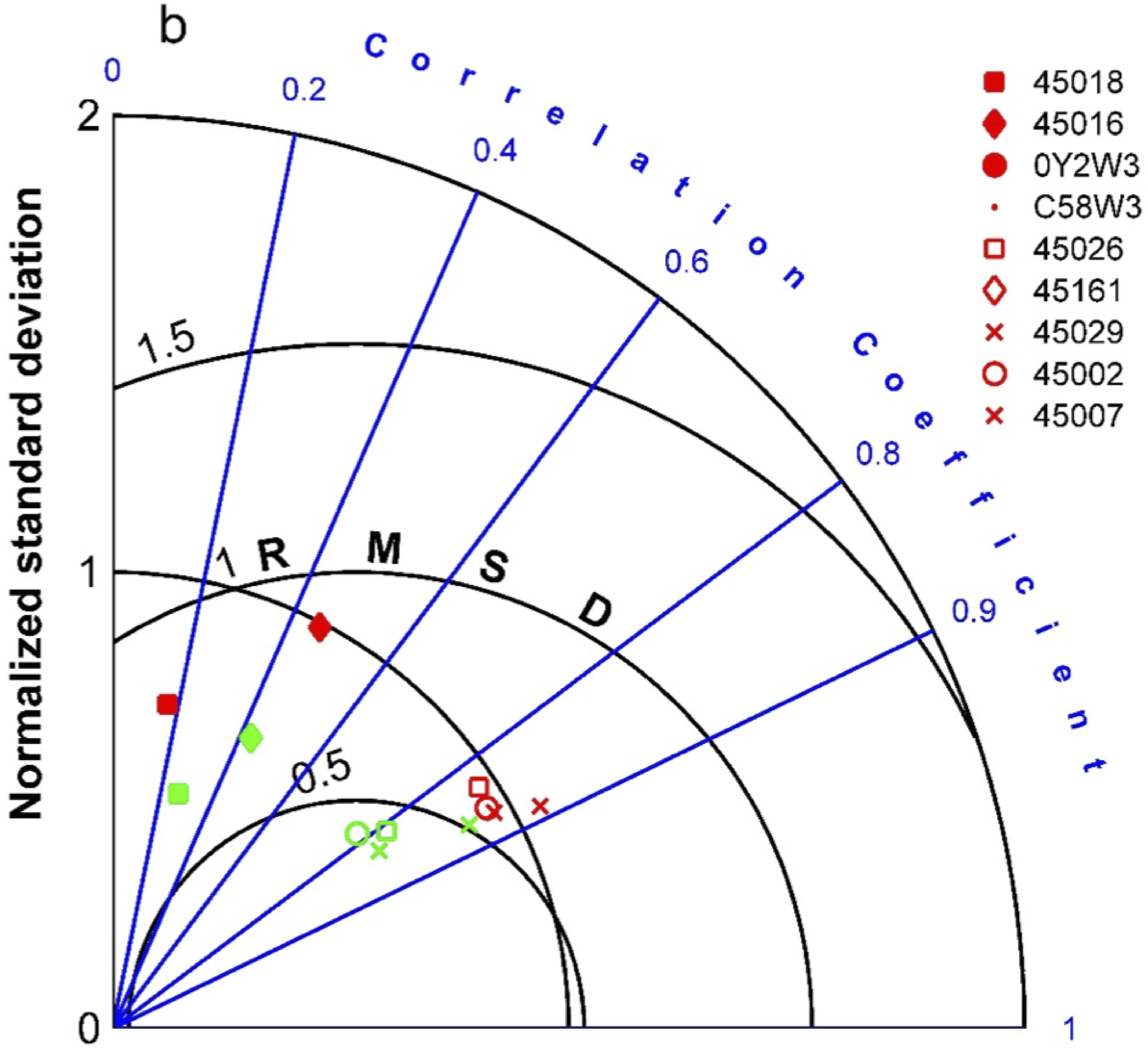
b
Correlation Coefficient
0
0.2
0.4
0.6
0.8
0.9
1
Normalized standard deviation
0
1
2
RMSD
1.5
1
0.5
45018
45016
0Y2W3
C58W3
45026
45161
45029
45002
45007

Observation
GEM
NNM
a
b
c
d
e
0Y2W3
C58W3
45013
45002
45007
Wind speed (m/s)
Wind direction (°)
Significant wave height (m)
Peak wave period (s)
Mean wave direction (°)
0
5
10
15
20
25
90
180
270
360
1
2
3
4
6
8
12
16
10/29
10/30
10/31
11/01
Date in 2012

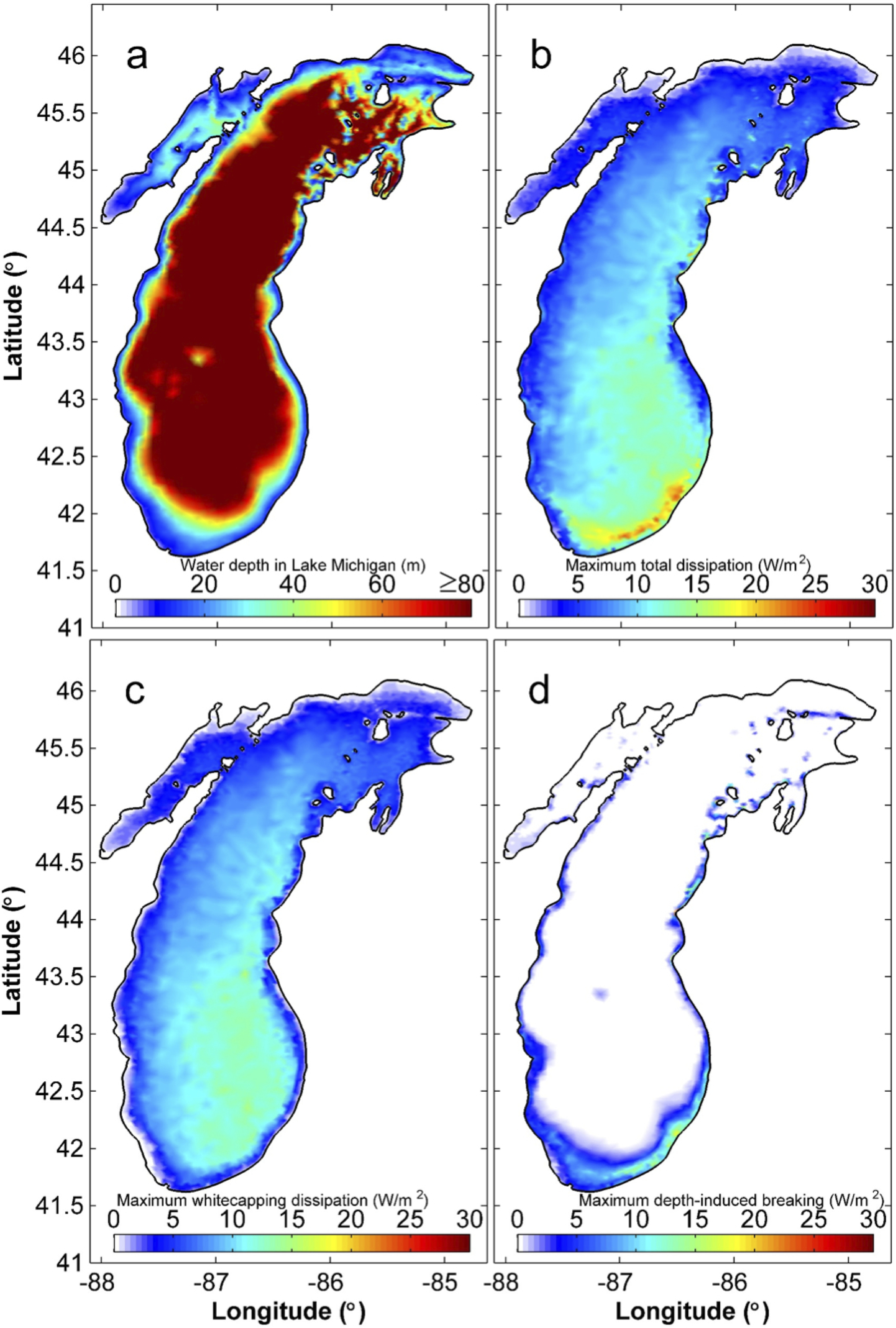
a
b
c
d
Water depth in Lake Michigan (m)
0 20 40 60 ≥80
Maximum total dissipation (W/m²)
Maximum whitecapping dissipation (W/m²)
Maximum depth-induced breaking (W/m²)
0 5 10 15 20 25 30
Latitude (°)
46 45.5 45 44.5 44 43.5 43 42.5 42 41.5 41
Longitude (°)
-88 -87 -86 -85

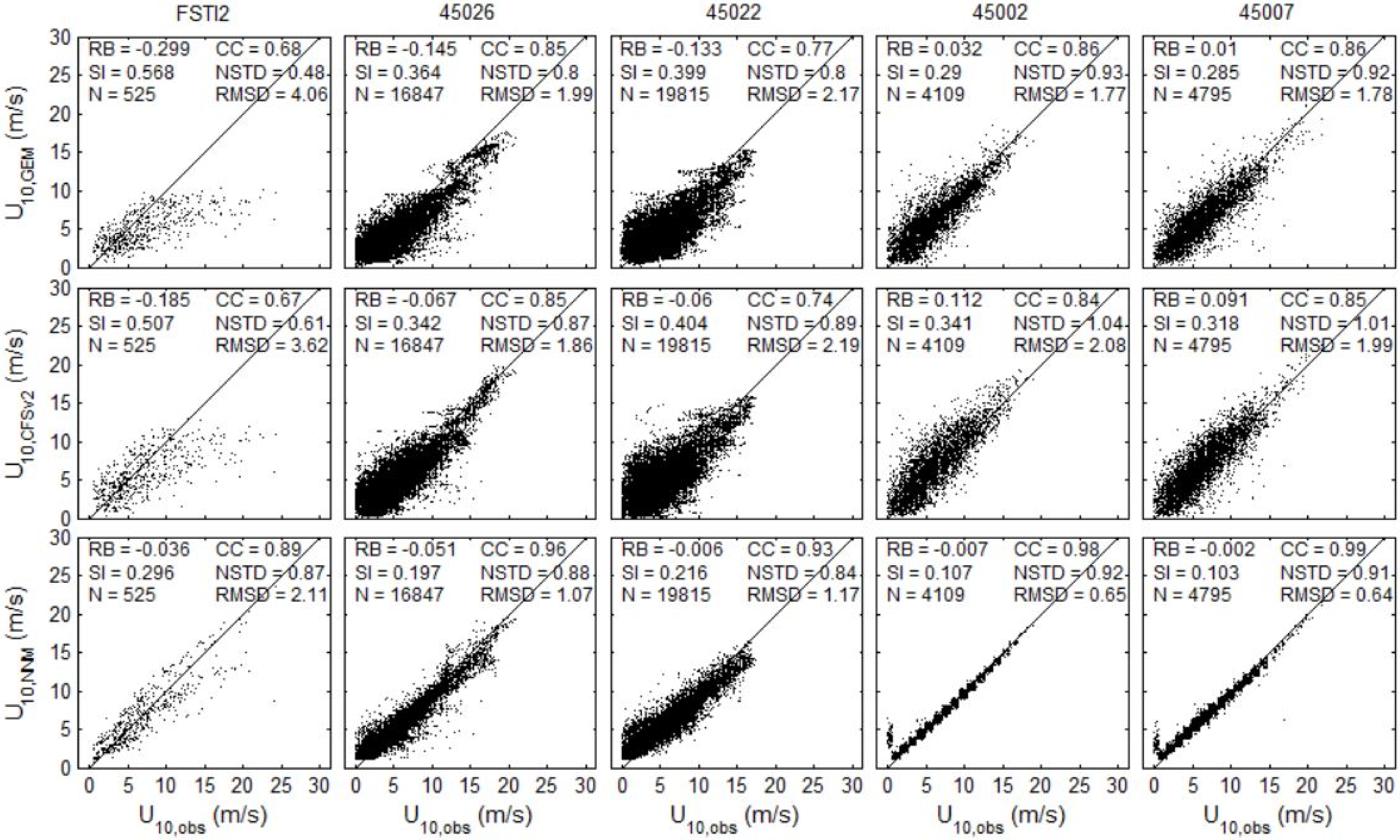
FSTI2
45026
45022
45002
45007
$U_{10,GEM}$ (m/s)
$U_{10,CFSv2}$ (m/s)
$U_{10,NMM}$ (m/s)
$U_{10,obs}$ (m/s)
0
5
10
15
20
25
30
RB = -0.299 CC = 0.68
SI = 0.568 NSTD = 0.48
N = 525 RMSD = 4.06
RB = -0.145 CC = 0.85
SI = 0.364 NSTD = 0.8
N = 16847 RMSD = 1.99
RB = -0.133 CC = 0.77
SI = 0.399 NSTD = 0.8
N = 19815 RMSD = 2.17
RB = 0.032 CC = 0.86
SI = 0.29 NSTD = 0.93
N = 4109 RMSD = 1.77
RB = 0.01 CC = 0.86
SI = 0.285 NSTD = 0.92
N = 4795 RMSD = 1.78
RB = -0.185 CC = 0.67
SI = 0.507 NSTD = 0.61
N = 525 RMSD = 3.62
RB = -0.067 CC = 0.85
SI = 0.342 NSTD = 0.87
N = 16847 RMSD = 1.86
RB = -0.06 CC = 0.74
SI = 0.404 NSTD = 0.89
N = 19815 RMSD = 2.19
RB = 0.112 CC = 0.84
SI = 0.341 NSTD = 1.04
N = 4109 RMSD = 2.08
RB = 0.091 CC = 0.85
SI = 0.318 NSTD = 1.01
N = 4795 RMSD = 1.99
RB = -0.036 CC = 0.89
SI = 0.296 NSTD = 0.87
N = 525 RMSD = 2.11
RB = -0.051 CC = 0.96
SI = 0.197 NSTD = 0.88
N = 16847 RMSD = 1.07
RB = -0.006 CC = 0.93
SI = 0.216 NSTD = 0.84
N = 19815 RMSD = 1.17
RB = -0.007 CC = 0.98
SI = 0.107 NSTD = 0.92
N = 4109 RMSD = 0.65
RB = -0.002 CC = 0.99
SI = 0.103 NSTD = 0.91
N = 4795 RMSD = 0.64

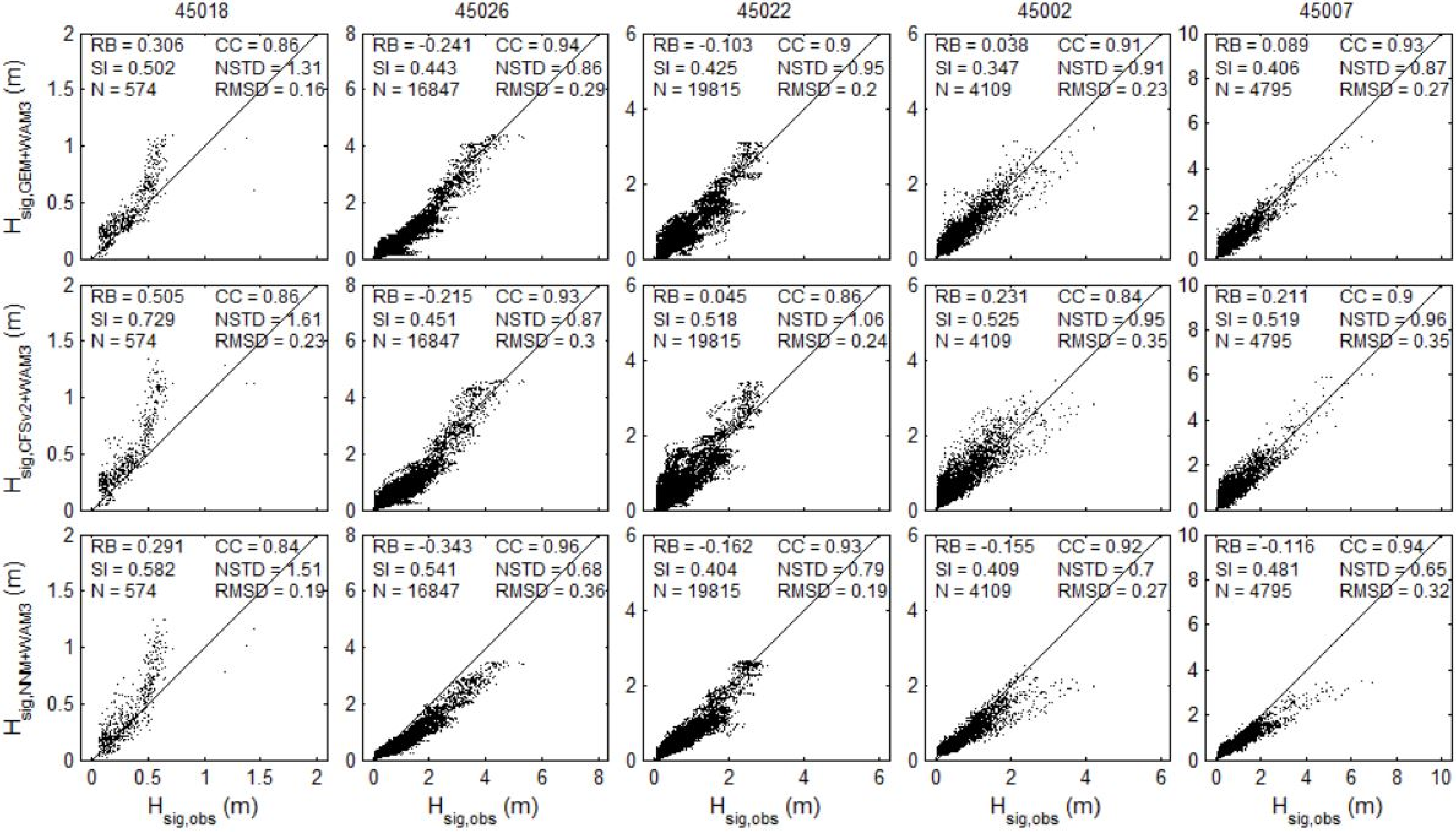
45018
45026
45022
45002
45007
RB = 0.306 CC = 0.86
SI = 0.502 NSTD = 1.31
N = 574 RMSD = 0.16
RB = -0.241 CC = 0.94
SI = 0.443 NSTD = 0.86
N = 16847 RMSD = 0.29
RB = -0.103 CC = 0.9
SI = 0.425 NSTD = 0.95
N = 19815 RMSD = 0.2
RB = 0.038 CC = 0.91
SI = 0.347 NSTD = 0.91
N = 4109 RMSD = 0.23
RB = 0.089 CC = 0.93
SI = 0.406 NSTD = 0.87
N = 4795 RMSD = 0.27
RB = 0.505 CC = 0.86
SI = 0.729 NSTD = 1.61
N = 574 RMSD = 0.23
RB = -0.215 CC = 0.93
SI = 0.451 NSTD = 0.87
N = 16847 RMSD = 0.3
RB = 0.045 CC = 0.86
SI = 0.518 NSTD = 1.06
N = 19815 RMSD = 0.24
RB = 0.231 CC = 0.84
SI = 0.525 NSTD = 0.95
N = 4109 RMSD = 0.35
RB = 0.211 CC = 0.9
SI = 0.519 NSTD = 0.96
N = 4795 RMSD = 0.35
RB = 0.291 CC = 0.84
SI = 0.582 NSTD = 1.51
N = 574 RMSD = 0.19
RB = -0.343 CC = 0.96
SI = 0.541 NSTD = 0.68
N = 16847 RMSD = 0.36
RB = -0.162 CC = 0.93
SI = 0.404 NSTD = 0.79
N = 19815 RMSD = 0.19
RB = -0.155 CC = 0.92
SI = 0.409 NSTD = 0.7
N = 4109 RMSD = 0.27
RB = -0.116 CC = 0.94
SI = 0.481 NSTD = 0.65
N = 4795 RMSD = 0.32
$H_{sig,GEM+WAM3}$ (m)
$H_{sig,CFSv2+WAM3}$ (m)
$H_{sig,NM+WAM3}$ (m)
$H_{sig,obs}$ (m)
0
0.5
1
1.5
2
4
6
8
10

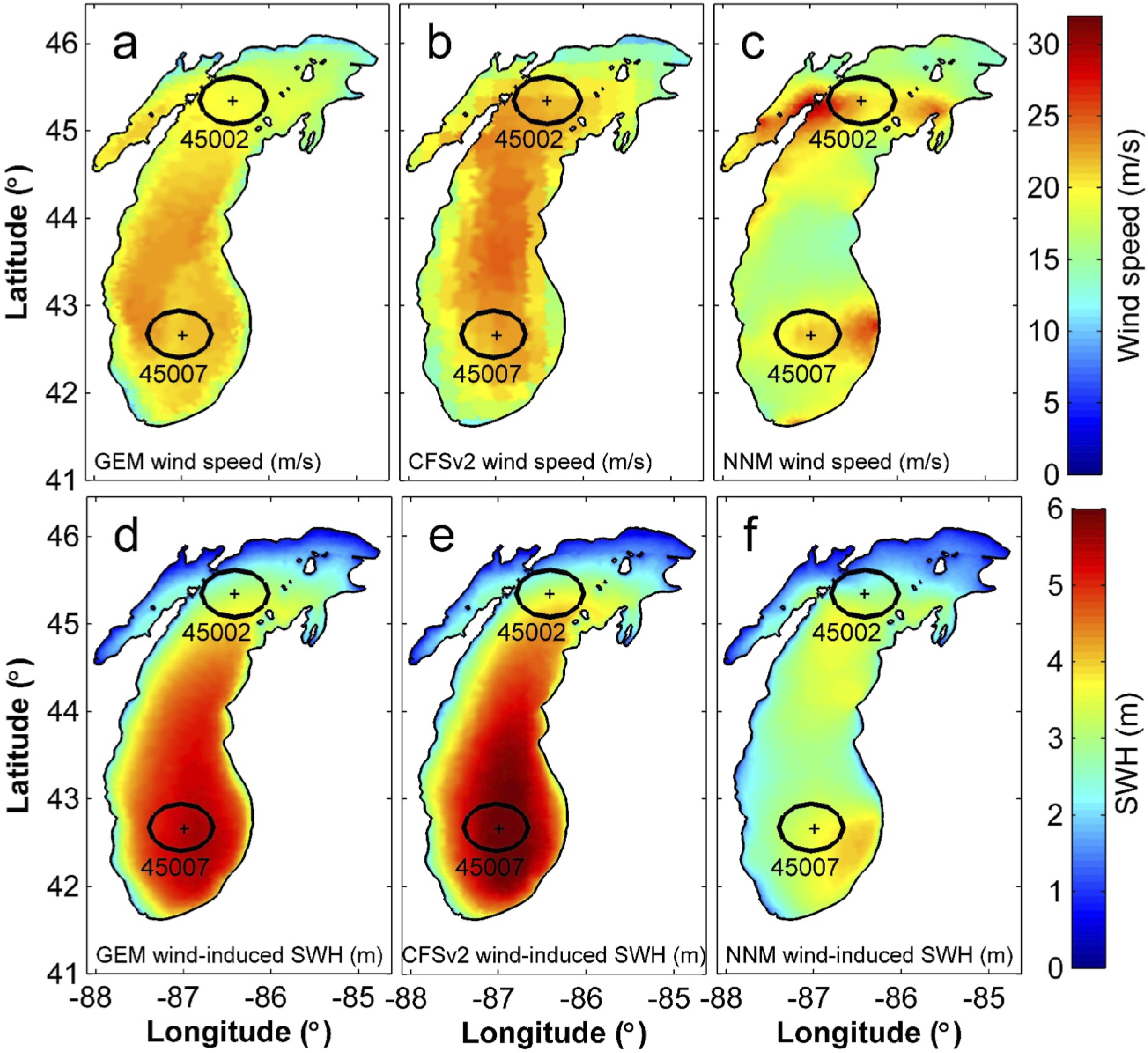
a
b
c
d
e
f
45002
45007
GEM wind speed (m/s)
CFSv2 wind speed (m/s)
NNM wind speed (m/s)
GEM wind-induced SWH (m)
CFSv2 wind-induced SWH (m)
NNM wind-induced SWH (m)
Latitude (°)
Longitude (°)
Wind speed (m/s)
SWH (m)
41
42
43
44
45
46
-88
-87
-86
-85
0
5
10
15
20
25
30
0
1
2
3
4
5
6

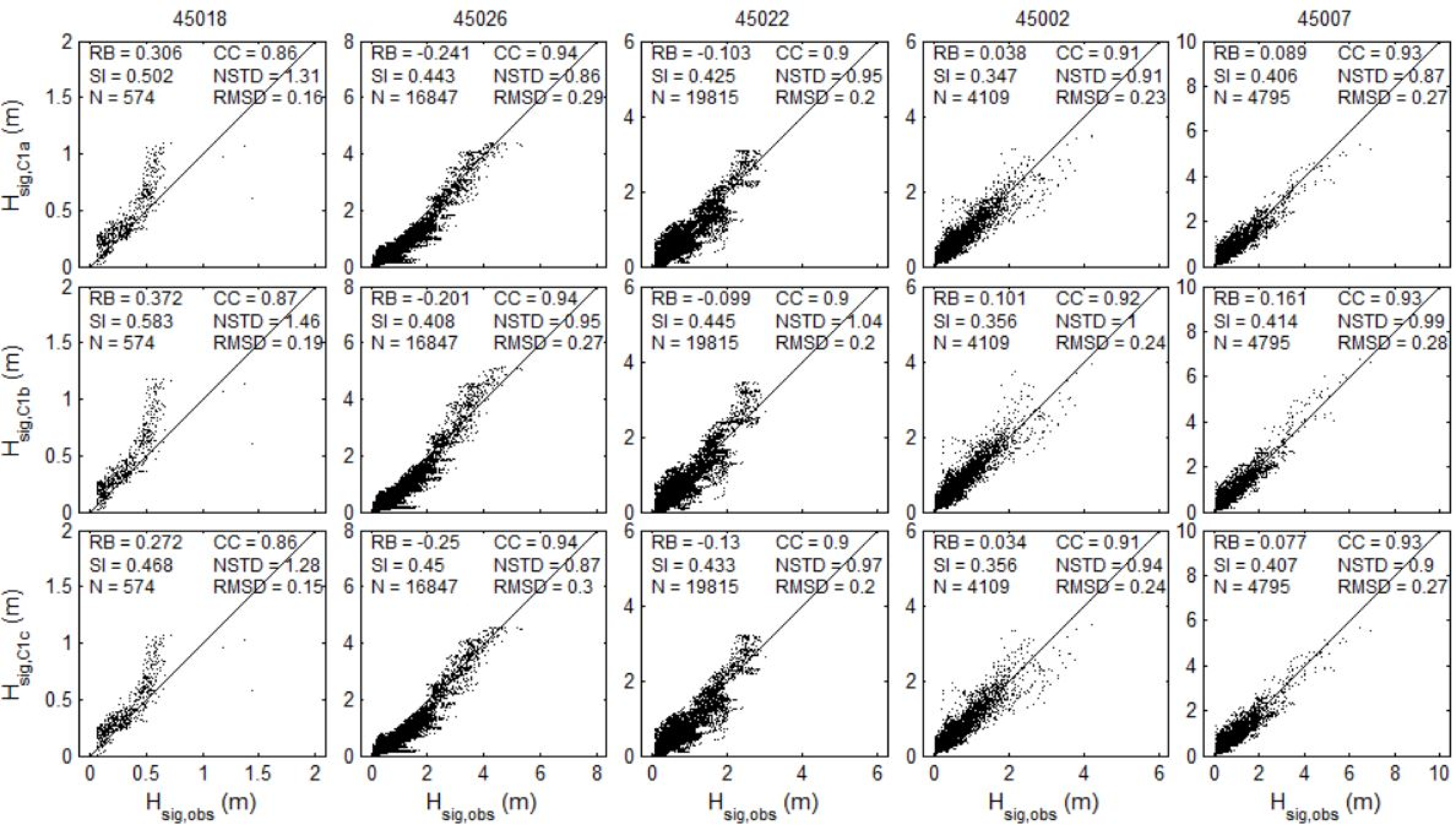
45018
45026
45022
45002
45007
RB = 0.306 CC = 0.86
SI = 0.502 NSTD = 1.31
N = 574 RMSD = 0.16
RB = -0.241 CC = 0.94
SI = 0.443 NSTD = 0.86
N = 16847 RMSD = 0.29
RB = -0.103 CC = 0.9
SI = 0.425 NSTD = 0.95
N = 19815 RMSD = 0.2
RB = 0.038 CC = 0.91
SI = 0.347 NSTD = 0.91
N = 4109 RMSD = 0.23
RB = 0.089 CC = 0.93
SI = 0.406 NSTD = 0.87
N = 4795 RMSD = 0.27
RB = 0.372 CC = 0.87
SI = 0.583 NSTD = 1.46
N = 574 RMSD = 0.19
RB = -0.201 CC = 0.94
SI = 0.408 NSTD = 0.95
N = 16847 RMSD = 0.27
RB = -0.099 CC = 0.9
SI = 0.445 NSTD = 1.04
N = 19815 RMSD = 0.2
RB = 0.101 CC = 0.92
SI = 0.356 NSTD = 1
N = 4109 RMSD = 0.24
RB = 0.161 CC = 0.93
SI = 0.414 NSTD = 0.99
N = 4795 RMSD = 0.28
RB = 0.272 CC = 0.86
SI = 0.468 NSTD = 1.28
N = 574 RMSD = 0.15
RB = -0.25 CC = 0.94
SI = 0.45 NSTD = 0.87
N = 16847 RMSD = 0.3
RB = -0.13 CC = 0.9
SI = 0.433 NSTD = 0.97
N = 19815 RMSD = 0.2
RB = 0.034 CC = 0.91
SI = 0.356 NSTD = 0.94
N = 4109 RMSD = 0.24
RB = 0.077 CC = 0.93
SI = 0.407 NSTD = 0.9
N = 4795 RMSD = 0.27
$H_{sig,C1a}$ (m)
$H_{sig,C1b}$ (m)
$H_{sig,C1c}$ (m)
$H_{sig,obs}$ (m)
0 0.5 1 1.5 2
0 2 4 6 8
0 2 4 6
0 2 4 6 8 10

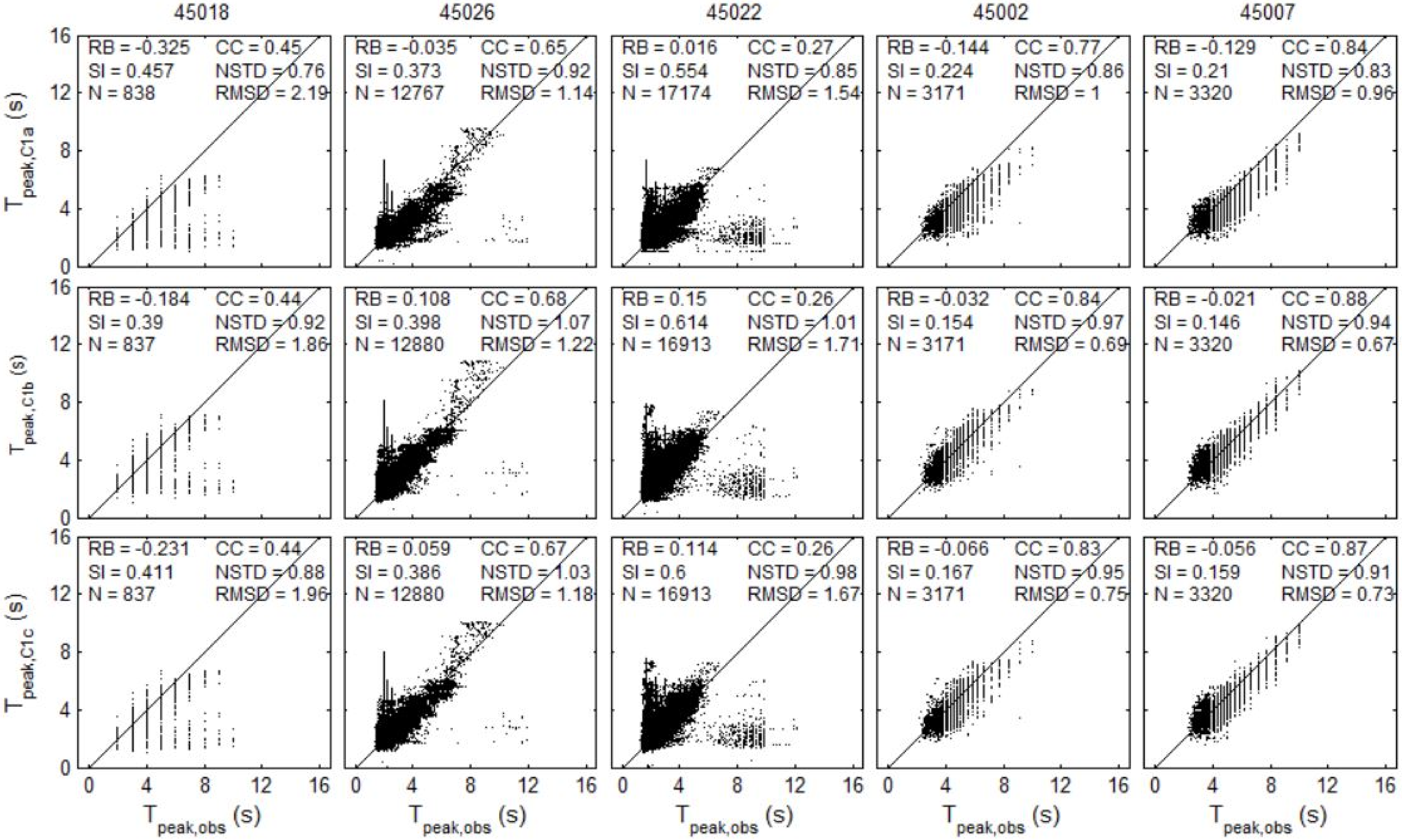
45018
45026
45022
45002
45007
RB = -0.325 CC = 0.45
SI = 0.457 NSTD = 0.76
N = 838 RMSD = 2.19
RB = -0.035 CC = 0.65
SI = 0.373 NSTD = 0.92
N = 12767 RMSD = 1.14
RB = 0.016 CC = 0.27
SI = 0.554 NSTD = 0.85
N = 17174 RMSD = 1.54
RB = -0.144 CC = 0.77
SI = 0.224 NSTD = 0.86
N = 3171 RMSD = 1
RB = -0.129 CC = 0.84
SI = 0.21 NSTD = 0.83
N = 3320 RMSD = 0.96
RB = -0.184 CC = 0.44
SI = 0.39 NSTD = 0.92
N = 837 RMSD = 1.86
RB = 0.108 CC = 0.68
SI = 0.398 NSTD = 1.07
N = 12880 RMSD = 1.22
RB = 0.15 CC = 0.26
SI = 0.614 NSTD = 1.01
N = 16913 RMSD = 1.71
RB = -0.032 CC = 0.84
SI = 0.154 NSTD = 0.97
N = 3171 RMSD = 0.69
RB = -0.021 CC = 0.88
SI = 0.146 NSTD = 0.94
N = 3320 RMSD = 0.67
RB = -0.231 CC = 0.44
SI = 0.411 NSTD = 0.88
N = 837 RMSD = 1.96
RB = 0.059 CC = 0.67
SI = 0.386 NSTD = 1.03
N = 12880 RMSD = 1.18
RB = 0.114 CC = 0.26
SI = 0.6 NSTD = 0.98
N = 16913 RMSD = 1.67
RB = -0.066 CC = 0.83
SI = 0.167 NSTD = 0.95
N = 3171 RMSD = 0.75
RB = -0.056 CC = 0.87
SI = 0.159 NSTD = 0.91
N = 3320 RMSD = 0.73
$T_{peak,C1a}$ (s)
$T_{peak,C1b}$ (s)
$T_{peak,C1c}$ (s)
0
4
8
12
16
$T_{peak,obs}$ (s)

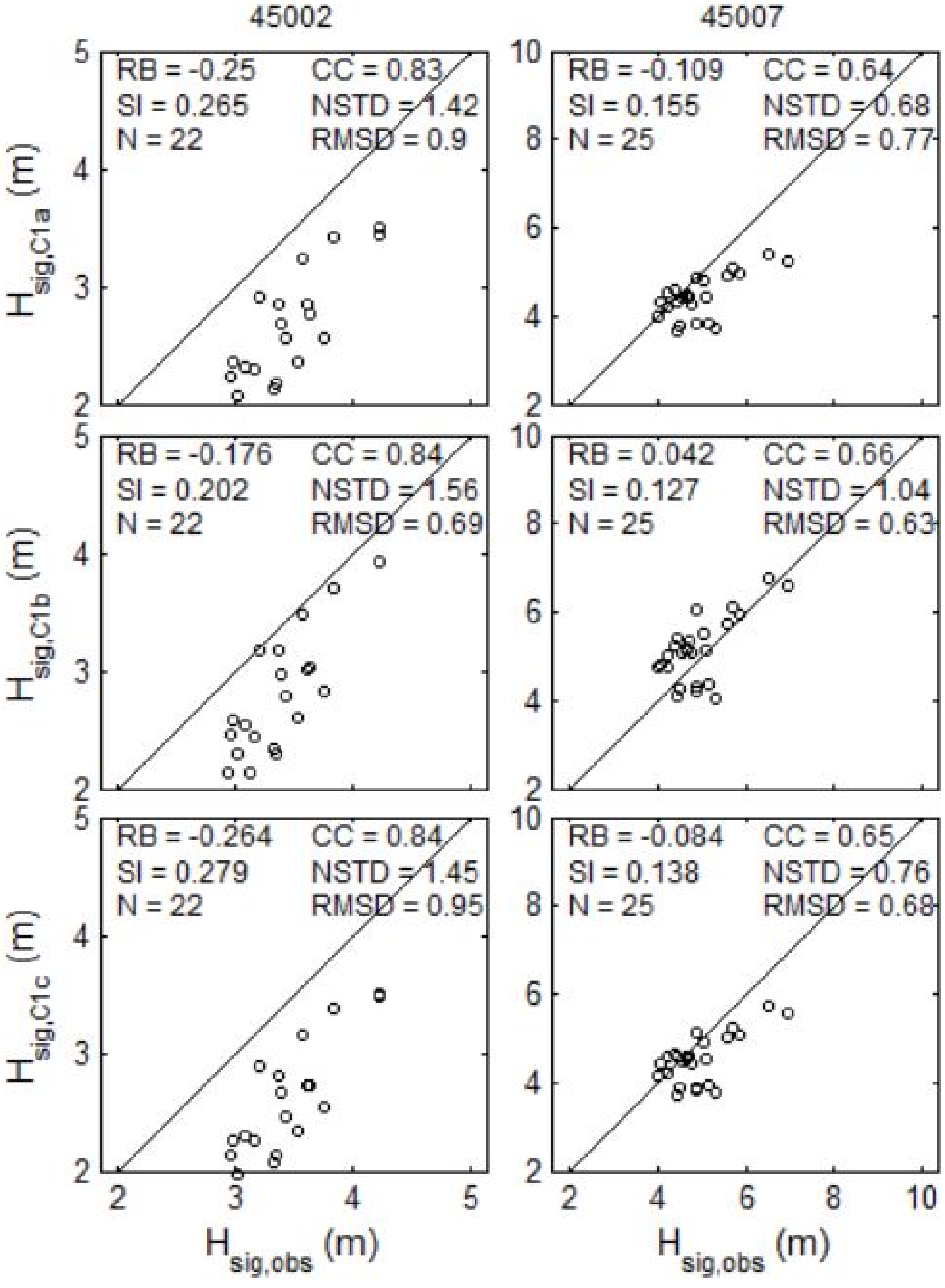
45002
45007
RB = -0.25
CC = 0.83
SI = 0.265
NSTD = 1.42
N = 22
RMSD = 0.9
RB = -0.109
CC = 0.64
SI = 0.155
NSTD = 0.68
N = 25
RMSD = 0.77
RB = -0.176
CC = 0.84
SI = 0.202
NSTD = 1.56
N = 22
RMSD = 0.69
RB = 0.042
CC = 0.66
SI = 0.127
NSTD = 1.04
N = 25
RMSD = 0.63
RB = -0.264
CC = 0.84
SI = 0.279
NSTD = 1.45
N = 22
RMSD = 0.95
RB = -0.084
CC = 0.65
SI = 0.138
NSTD = 0.76
N = 25
RMSD = 0.68
$H_{sig,C1a}$ (m)
$H_{sig,C1b}$ (m)
$H_{sig,C1c}$ (m)
$H_{sig,obs}$ (m)
$H_{sig,obs}$ (m)
2
3
4
5
2
4
6
8
10

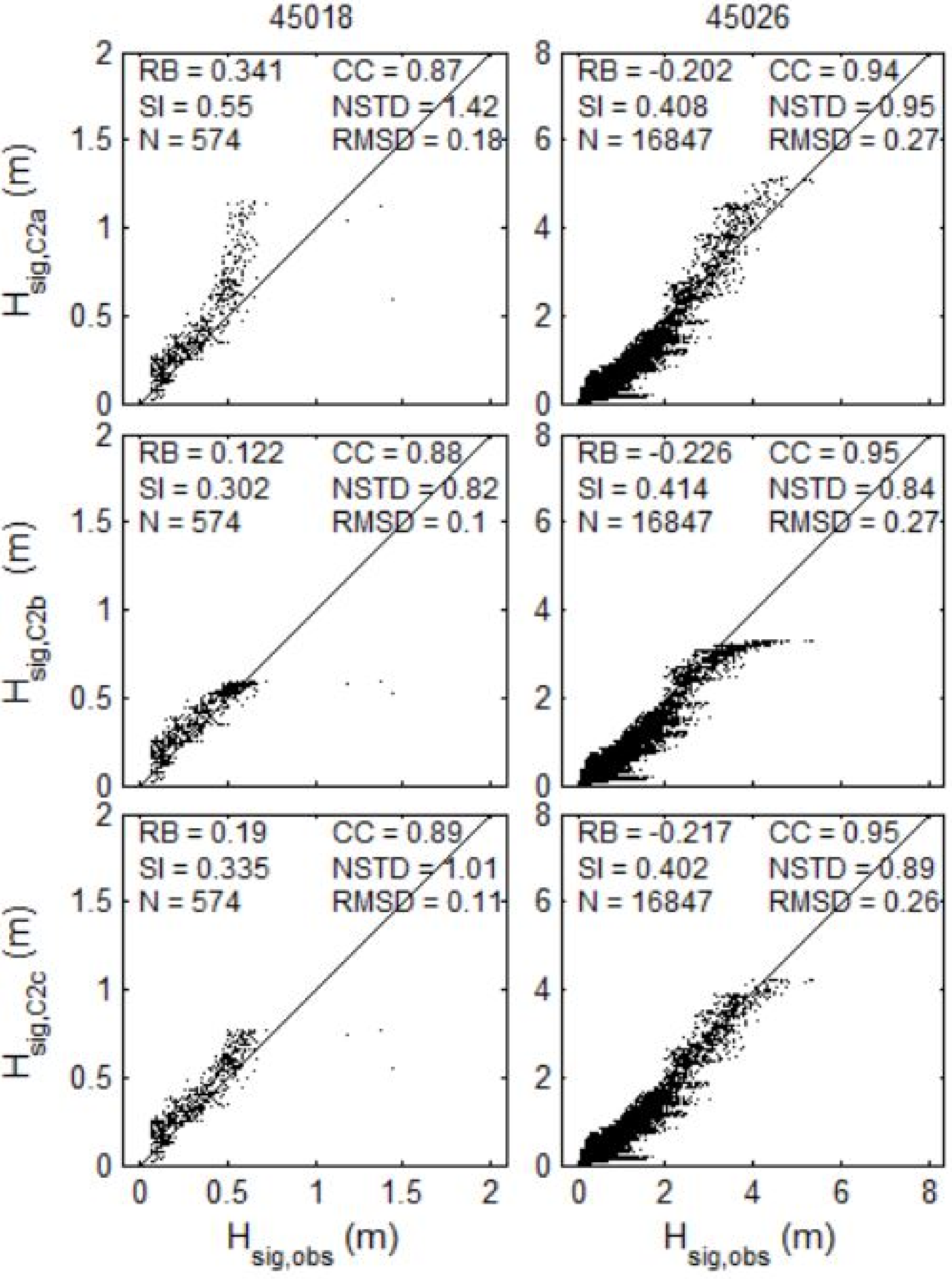
45018
45026
RB = 0.341
CC = 0.87
SI = 0.55
NSTD = 1.42
N = 574
RMSD = 0.18
RB = -0.202
CC = 0.94
SI = 0.408
NSTD = 0.95
N = 16847
RMSD = 0.27
RB = 0.122
CC = 0.88
SI = 0.302
NSTD = 0.82
N = 574
RMSD = 0.1
RB = -0.226
CC = 0.95
SI = 0.414
NSTD = 0.84
N = 16847
RMSD = 0.27
RB = 0.19
CC = 0.89
SI = 0.335
NSTD = 1.01
N = 574
RMSD = 0.11
RB = -0.217
CC = 0.95
SI = 0.402
NSTD = 0.89
N = 16847
RMSD = 0.26
$H_{sig,C2a}$ (m)
$H_{sig,C2b}$ (m)
$H_{sig,C2c}$ (m)
$H_{sig,obs}$ (m)
$H_{sig,obs}$ (m)
0
0.5
1
1.5
2
0
2
4
6
8

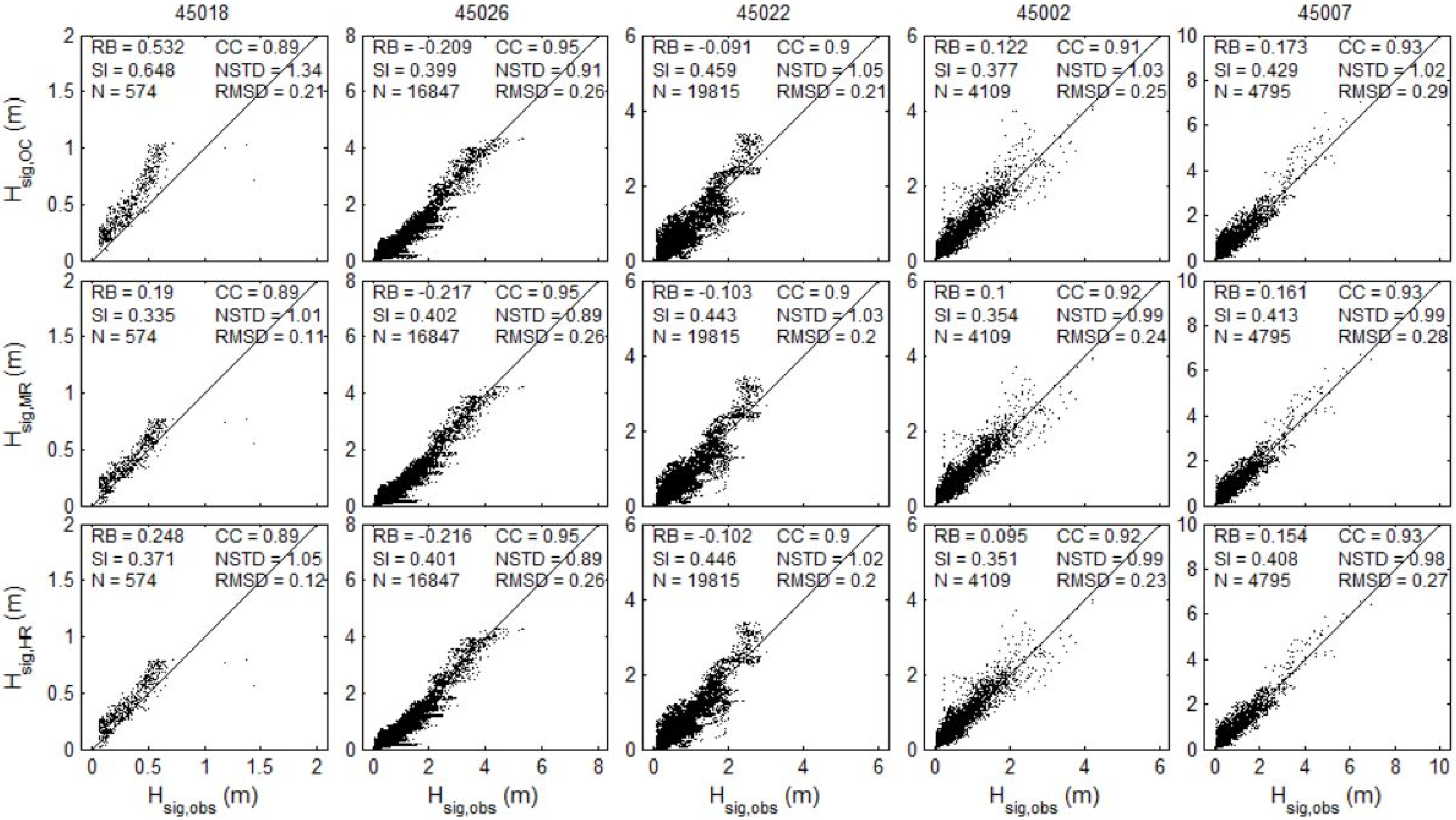
45018
45026
45022
45002
45007
RB = 0.532 CC = 0.89
SI = 0.648 NSTD = 1.34
N = 574 RMSD = 0.21
RB = -0.209 CC = 0.95
SI = 0.399 NSTD = 0.91
N = 16847 RMSD = 0.26
RB = -0.091 CC = 0.9
SI = 0.459 NSTD = 1.05
N = 19815 RMSD = 0.21
RB = 0.122 CC = 0.91
SI = 0.377 NSTD = 1.03
N = 4109 RMSD = 0.25
RB = 0.173 CC = 0.93
SI = 0.429 NSTD = 1.02
N = 4795 RMSD = 0.29
RB = 0.19 CC = 0.89
SI = 0.335 NSTD = 1.01
N = 574 RMSD = 0.11
RB = -0.217 CC = 0.95
SI = 0.402 NSTD = 0.89
N = 16847 RMSD = 0.26
RB = -0.103 CC = 0.9
SI = 0.443 NSTD = 1.03
N = 19815 RMSD = 0.2
RB = 0.1 CC = 0.92
SI = 0.354 NSTD = 0.99
N = 4109 RMSD = 0.24
RB = 0.161 CC = 0.93
SI = 0.413 NSTD = 0.99
N = 4795 RMSD = 0.28
RB = 0.248 CC = 0.89
SI = 0.371 NSTD = 1.05
N = 574 RMSD = 0.12
RB = -0.216 CC = 0.95
SI = 0.401 NSTD = 0.89
N = 16847 RMSD = 0.26
RB = -0.102 CC = 0.9
SI = 0.446 NSTD = 1.02
N = 19815 RMSD = 0.2
RB = 0.095 CC = 0.92
SI = 0.351 NSTD = 0.99
N = 4109 RMSD = 0.23
RB = 0.154 CC = 0.93
SI = 0.408 NSTD = 0.98
N = 4795 RMSD = 0.27
$H_{sig,OC}$ (m)
$H_{sig,MR}$ (m)
$H_{sig,HR}$ (m)
$H_{sig,obs}$ (m)
0
0.5
1
1.5
2
4
6
8
10

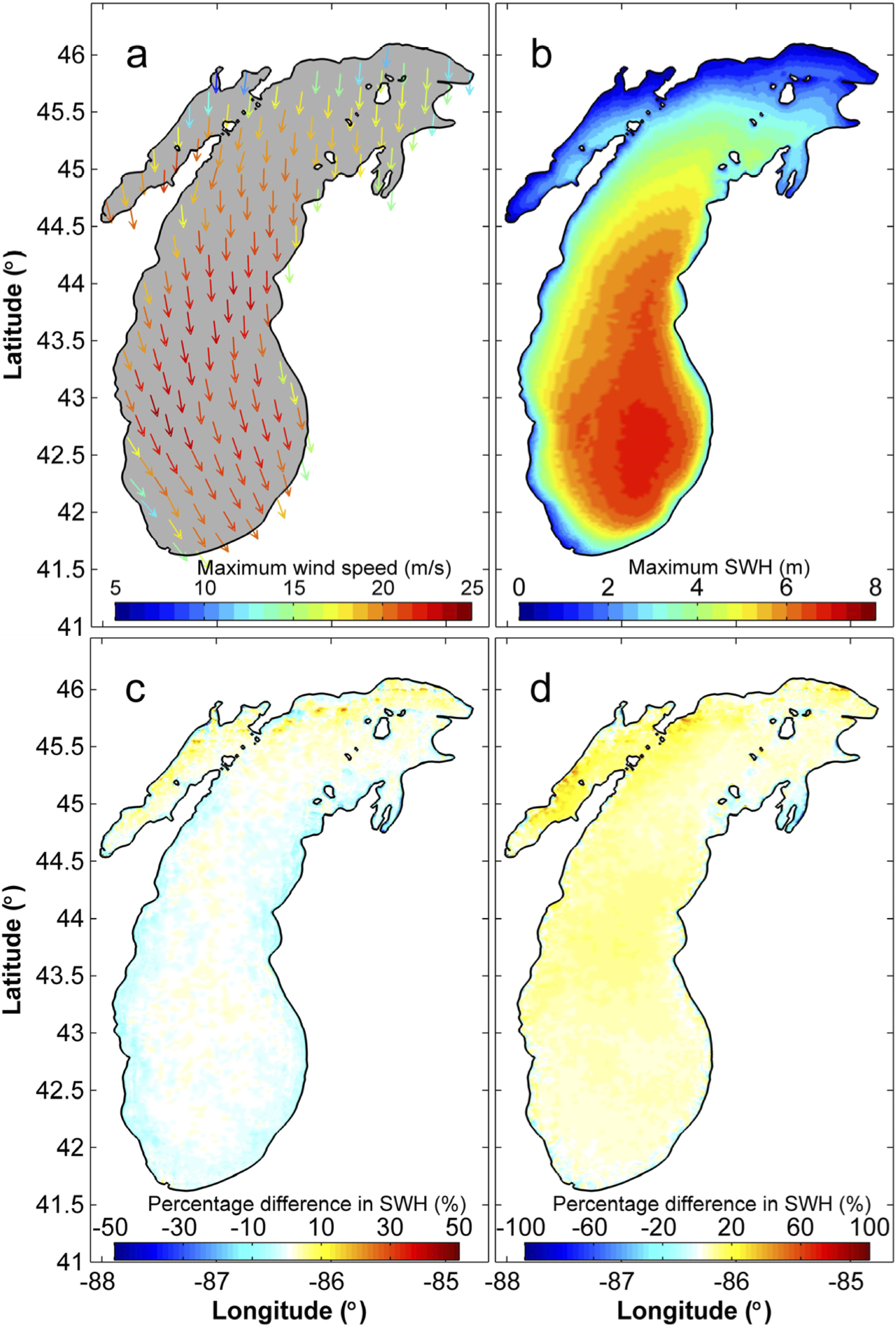
a
b
c
d
Latitude (°)
46
45.5
45
44.5
44
43.5
43
42.5
42
41.5
41
Maximum wind speed (m/s)
5
10
15
20
25
Maximum SWH (m)
0
2
4
6
8
Percentage difference in SWH (%)
-50
-30
-10
10
30
50
Percentage difference in SWH (%)
-100
-60
-20
20
60
100
-88
-87
-86
-85
Longitude (°)

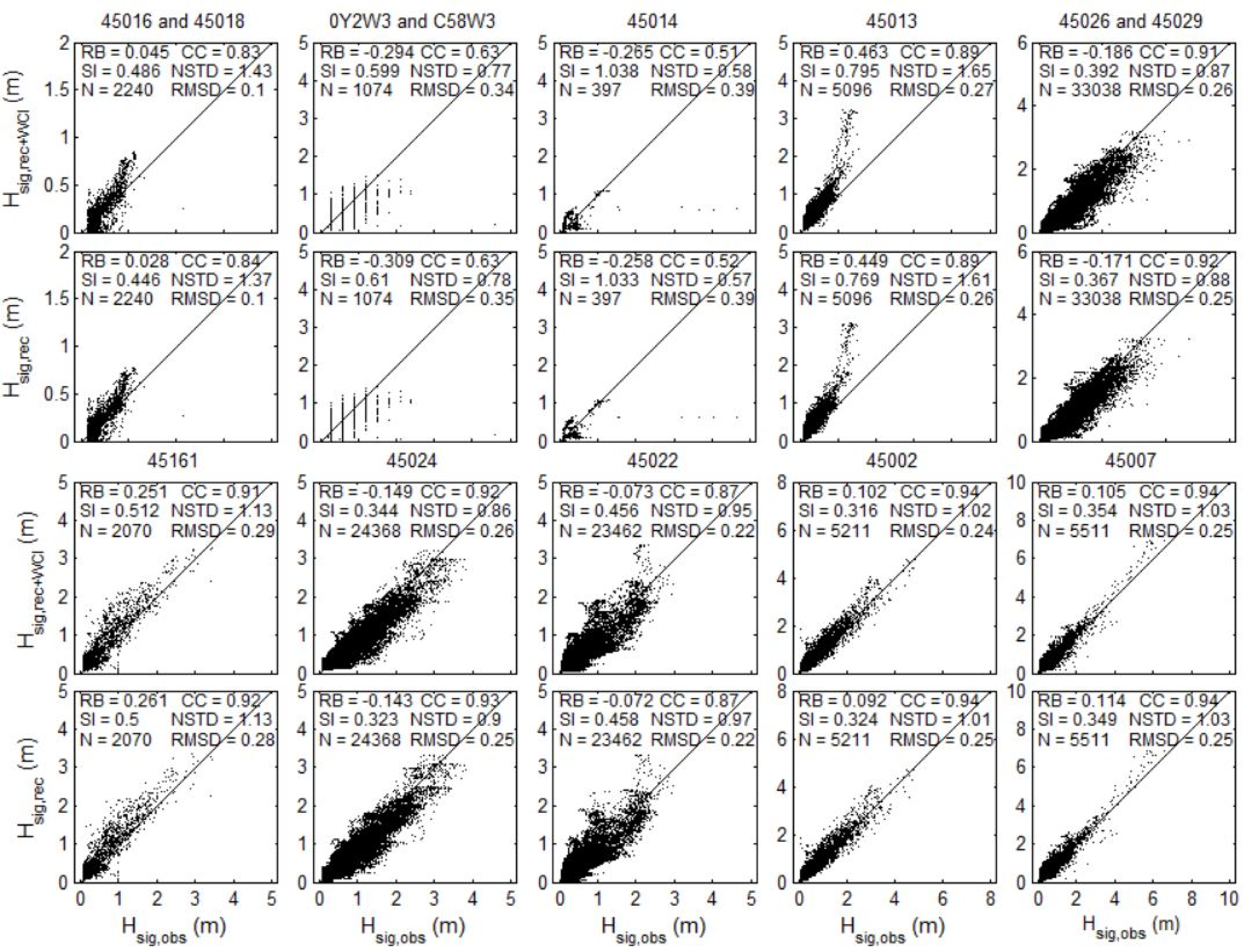
45016 and 45018
0Y2W3 and C58W3
45014
45013
45026 and 45029
RB = 0.045 CC = 0.83
SI = 0.486 NSTD = 1.43
N = 2240 RMSD = 0.1
RB = -0.294 CC = 0.63
SI = 0.599 NSTD = 0.77
N = 1074 RMSD = 0.34
RB = -0.265 CC = 0.51
SI = 1.038 NSTD = 0.58
N = 397 RMSD = 0.39
RB = 0.463 CC = 0.89
SI = 0.795 NSTD = 1.65
N = 5096 RMSD = 0.27
RB = -0.186 CC = 0.91
SI = 0.392 NSTD = 0.87
N = 33038 RMSD = 0.26
$H_{sig,rec+WCI}$ (m)
RB = 0.028 CC = 0.84
SI = 0.446 NSTD = 1.37
N = 2240 RMSD = 0.1
RB = -0.309 CC = 0.63
SI = 0.61 NSTD = 0.78
N = 1074 RMSD = 0.35
RB = -0.258 CC = 0.52
SI = 1.033 NSTD = 0.57
N = 397 RMSD = 0.39
RB = 0.449 CC = 0.89
SI = 0.769 NSTD = 1.61
N = 5096 RMSD = 0.26
RB = -0.171 CC = 0.92
SI = 0.367 NSTD = 0.88
N = 33038 RMSD = 0.25
$H_{sig,rec}$ (m)
45161
45024
45022
45002
45007
RB = 0.251 CC = 0.91
SI = 0.512 NSTD = 1.13
N = 2070 RMSD = 0.29
RB = -0.149 CC = 0.92
SI = 0.344 NSTD = 0.86
N = 24368 RMSD = 0.26
RB = -0.073 CC = 0.87
SI = 0.456 NSTD = 0.95
N = 23462 RMSD = 0.22
RB = 0.102 CC = 0.94
SI = 0.316 NSTD = 1.02
N = 5211 RMSD = 0.24
RB = 0.105 CC = 0.94
SI = 0.354 NSTD = 1.03
N = 5511 RMSD = 0.25
$H_{sig,rec+WCI}$ (m)
RB = 0.261 CC = 0.92
SI = 0.5 NSTD = 1.13
N = 2070 RMSD = 0.28
RB = -0.143 CC = 0.93
SI = 0.323 NSTD = 0.9
N = 24368 RMSD = 0.25
RB = -0.072 CC = 0.87
SI = 0.458 NSTD = 0.97
N = 23462 RMSD = 0.22
RB = 0.092 CC = 0.94
SI = 0.324 NSTD = 1.01
N = 5211 RMSD = 0.25
RB = 0.114 CC = 0.94
SI = 0.349 NSTD = 1.03
N = 5511 RMSD = 0.25
$H_{sig,rec}$ (m)
$H_{sig,obs}$ (m)
$H_{sig,obs}$ (m)
$H_{sig,obs}$ (m)
$H_{sig,obs}$ (m)
$H_{sig,obs}$ (m)

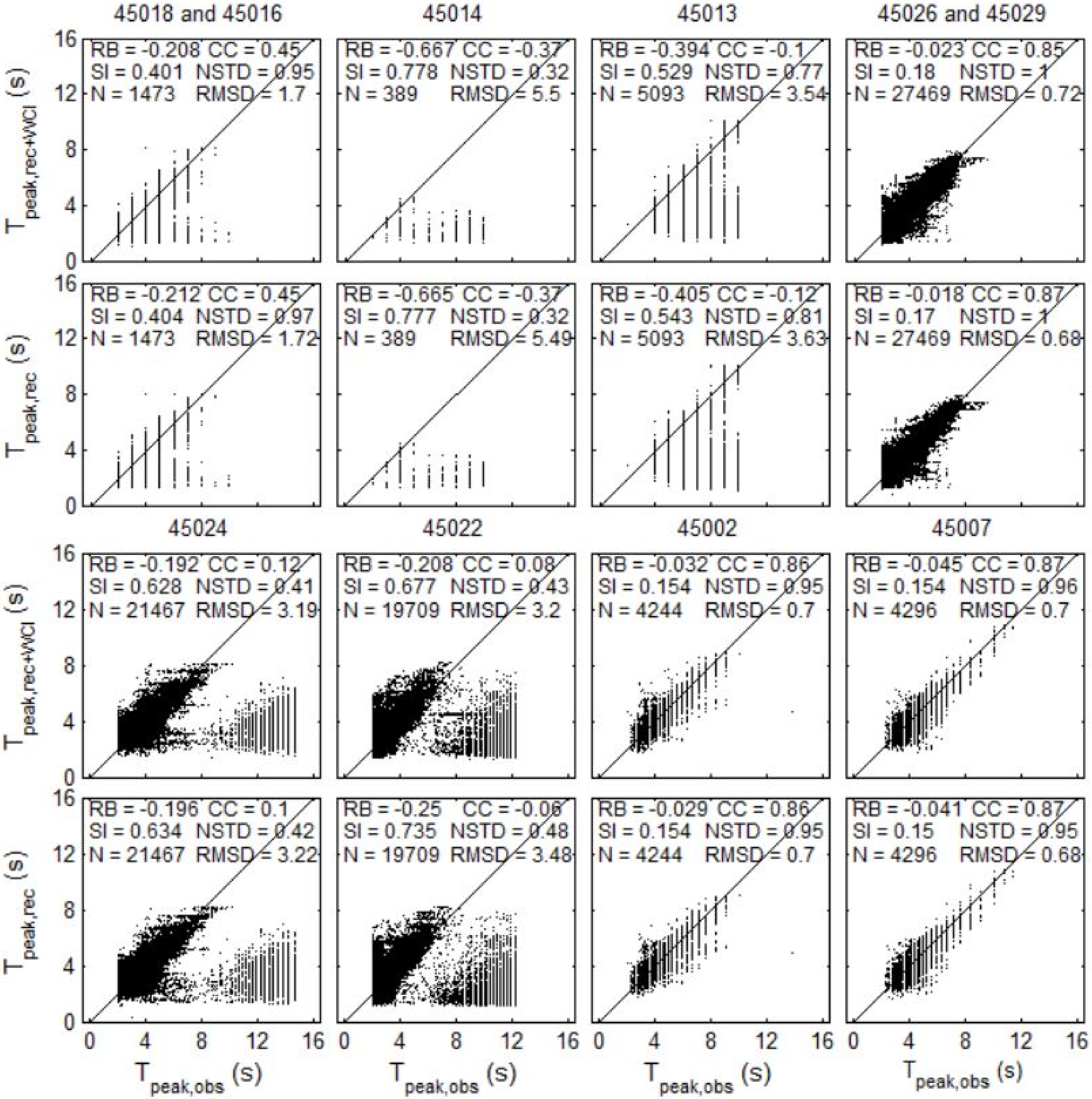
45018 and 45016
45014
45013
45026 and 45029
RB = -0.208 CC = 0.45
SI = 0.401 NSTD = 0.95
N = 1473 RMSD = 1.7
RB = -0.667 CC = -0.37
SI = 0.778 NSTD = 0.32
N = 389 RMSD = 5.5
RB = -0.394 CC = -0.1
SI = 0.529 NSTD = 0.77
N = 5093 RMSD = 3.54
RB = -0.023 CC = 0.85
SI = 0.18 NSTD = 1
N = 27469 RMSD = 0.72
$T_{peak,rec+WCI}$ (s)
RB = -0.212 CC = 0.45
SI = 0.404 NSTD = 0.97
N = 1473 RMSD = 1.72
RB = -0.665 CC = -0.37
SI = 0.777 NSTD = 0.32
N = 389 RMSD = 5.49
RB = -0.405 CC = -0.12
SI = 0.543 NSTD = 0.81
N = 5093 RMSD = 3.63
RB = -0.018 CC = 0.87
SI = 0.17 NSTD = 1
N = 27469 RMSD = 0.68
$T_{peak,rec}$ (s)
45024
45022
45002
45007
RB = -0.192 CC = 0.12
SI = 0.628 NSTD = 0.41
N = 21467 RMSD = 3.19
RB = -0.208 CC = 0.08
SI = 0.677 NSTD = 0.43
N = 19709 RMSD = 3.2
RB = -0.032 CC = 0.86
SI = 0.154 NSTD = 0.95
N = 4244 RMSD = 0.7
RB = -0.045 CC = 0.87
SI = 0.154 NSTD = 0.96
N = 4296 RMSD = 0.7
$T_{peak,rec+WCI}$ (s)
RB = -0.196 CC = 0.1
SI = 0.634 NSTD = 0.42
N = 21467 RMSD = 3.22
RB = -0.25 CC = -0.06
SI = 0.735 NSTD = 0.48
N = 19709 RMSD = 3.48
RB = -0.029 CC = 0.86
SI = 0.154 NSTD = 0.95
N = 4244 RMSD = 0.7
RB = -0.041 CC = 0.87
SI = 0.15 NSTD = 0.95
N = 4296 RMSD = 0.68
$T_{peak,rec}$ (s)
0
4
8
12
16
$T_{peak,obs}$ (s)